Fiber Birefringence Modeling for Polarization Mode Dispersion

by

Weihong Huang

A thesis
presented to the University of Waterloo
in fulfilment of the
thesis requirement for the degree of
Doctor of Philosophy
in
Physics

Waterloo, Ontario, Canada, 2007

AUTHOR'S DECLARATION FOR ELECTRONIC SUBMISSION OF A THESIS

I hereby declare that I am the sole author of this thesis. This is a true copy of the thesis, including any required final revisions, as accepted by my examiners.

I understand that my thesis may be made electronically available to the public.

Abstract

This thesis concerns polarization mode dispersion (PMD) in optical fiber communications. Specifically, we study fiber birefringence, PMD stochastic properties, PMD mitigation and the interaction of fiber birefringence and fiber nonlinearity.

Fiber birefringence is the physical origin of polarization mode dispersion. Current models of birefringence in optical fibers assume that the birefringence vector varies randomly either in orientation with a fixed magnitude or simultaneously in both magnitude and direction. These models are applicable only to certain birefringence profiles. For a broader range of birefringence profiles, we propose and investigate four general models in which the stochastically varying amplitude is restricted to a limited range. In addition, mathematical algorithms are introduced for the numerical implementation of these models. To investigate polarization mode dispersion, we first apply these models to single mode fibers. In particular, two existing models and our four more general models are employed for the evolution of optical fiber birefringence with longitudinal distance to analyze, both theoretically and numerically, the behavior of the polarization mode dispersion. We find that while the probability distribution function of the differential group delay (DGD) varies along the fiber length as in existing models, the dependence of the mean DGD on fiber length differs noticeably from earlier predictions.

Fiber spinning reduces polarization mode dispersion effects in optical fibers. Since relatively few studies have been performed of the dependence of the reduction factor on the strength of random background birefringence fluctuations, we here apply a general birefringence model to sinusoidal spun fibers. We find that while, as expected, the phase matching condition is not affected by random perturbations, the degree of PMD reduction as well as the probability distribution function of the DGD are both influenced by the random components of the birefringence. Together with other researchers, I have also examined a series of experimentally realizable procedures to compensate for PMD in optical fiber systems. This work demonstrates that a symmetric ordering of compensator elements combined with Taylor and Chebyshev approximations to the transfer matrix for the light polarization in optical fibers can significantly widen the compensation bandwidth.

In the last part of the thesis, we applied the Manakov-PMD equation and a general model of fiber birefringence to investigate pulse distortion induced by the interaction of fiber birefringence and fiber nonlinearity. We find that the effect of nonlinearity on the pulse distortion differs markedly with the birefringence profile.

Acknowledgements

I would like to thank my supervisor, Dr. David Yevick, for his essential guidance and support. This thesis is only possible with his insightful suggestions and generous encouragement. I would also like to thank my co-supervisor, Dr. Joseph Sanderson for his kind support. Further thanks go to my advisory committee, Dr. Donna Strickland, Dr. Wing-Ki Liu, Dr. Fred McCourt, and my External Examiner for my Ph.D thesis oral examination, Dr. Henry Yaffe of New Ridge Technologies in Reisterstown, Maryland, for their support and insightful suggestions.

I wish to express my sincere appreciation to Dr. Witold Bardyszewski of Warswaw University, Henghua Deng, Lixin Zhan, Mark Chnachowicz, Michael Reimer and many other colleagues for sharing ideas and fruitful discussions.

Finally, I would like to extend my gratitude to our graduate secretary, Judy McDonnell, for her kindness and excellent services.

Contents

List of Figures

Chapter 1

Introduction

1.1 Background

1.1.1 Fiber-Optic Communication Systems

Lightwave communication systems use electromagnetic waves in the near-infrared region as carriers to transmit information. Fiber-optic communication systems are lightwave systems that employ optical fibers as a light guiding medium. In most existing commercial fiber-optic communication links, information is encoded with square-wave optical pulses in return-to-zero (RZ) or non-return-to-zero (NRZ) format, c.f. Fig. 1.1 [2, 3].

Before the development of optical communication systems, two major forms of communication systems were employed. In the first of these, namely, electrical communication system, information is encoded as electrical pulses and transmitted through coaxial cable; the other system, i.e., microwave system, uses electromagnetic waves with frequencies in the range of $1 - 10\,GHz$ to transmit the signal [2]. These two systems are limited either by bandwidth due to high frequency-dependent loss of coaxial cable of the electrical system, or bit rate due to the low carrier frequencies of the microwave system. Fortunately, these two obstacles could be overcome by using optical communication system, thanks to the invention of the laser

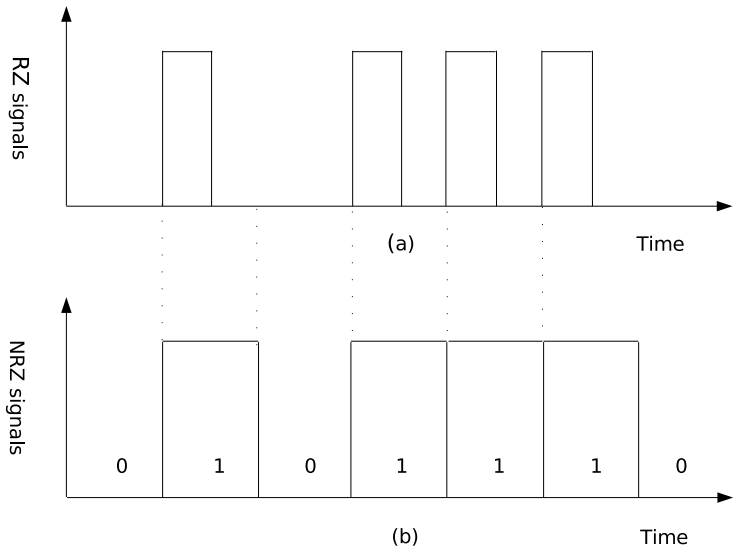

Figure 1.1: Digital bit stream 0101110 $\cdots$ coded by (a) return-to-zero (RZ) and (b) nonreturn-to-zero (NRZ) formats.

in 1960 and the breakthrough technology of low-loss optical fibers in 1970. Specifically, the high frequencies ($\sim 100\,THz$) of the optical pulses increase enormously the bit-rate of the system, and the fiber loss has been reduced to below $20\,dB/km$ in a broad wavelength range around $1\,\mu m$. While, for the advantage of low cost, electrical and microwave transmission technologies are still preferred for short distances and relatively low bandwidth applications, such as cable TV (Television), wireless LAN (Local Area Network), CCTV (Closed Circuit Television), and cell phones, etc, fiber-optic technology is generally used in telecommunications for its inherently high data-carrying capacity and the exceptionally low loss of the optical fiber.

The basic building block of all lightwave systems is a point-to-point link which is simply a connection from point A to point B. The main function of this link is to transport information at a specified bit rate and bit error rate (BER) over a specified distance. These links can be classified into two sub-categories: short-haul

and long-haul. Short-haul links are characterized by the fact that they contain no repeaters or amplifiers, and are typically of distance up to many tens of kilometers. Short-haul links are widely used in Metropolitan Area Networks (MANs) or Local Area Networks (LANs). Long-haul links do contain repeaters to compensate for loss and/or dispersion, and may be several $1000\,km$ in length. Long-haul links are widely used as backbones in large-scale terrestrial networks such as Wide Area Networks (WANs) and undersea intercontinental networks.

One of the major design considerations with point-to-point links is the repeater (or regenerator) spacing L. This spacing is usually in the range of $20 - 100\,km$ since various imperfections in the fiber and other optical components in the system can deform the pulses, causing errors in the transmitted signal. These imperfections include fiber loss, chromatic dispersion, polarization mode dispersion, fiber nonlinearity, etc. As a consequence, after propagating a certain distance in the system, optical signals need to be regenerated by going through the conversion process of light-electricity-light in repeaters to completely recover the original digital data stream within a given BER. Communication systems are usually characterized by the product of the bit rate B and the repeater spacing L, i.e., BL.

The development of the fiber-optic communication technology started around 1975. While it is only 30 years old, it has progressed rapidly and has evolved through several generations. The first generation of lightwave systems operates with wavelength $\lambda = 0.8\,\mu m$. Such systems became available commercially in 1980, and the BL has reached $\sim 1\,GHz \cdot km$. The BL product has been increased considerably in the second generation of fiber-optic communication system operating in the wavelength near $1.3\,\mu m$, where the fiber has minimum chromatic dispersion. By the use of single-mode fiber, second generation lightwave system, operating at bit rates of up to $1.7\,GHz$ with a repeater spacing of about $50\,km$, were commercially available by 1987. The second-generation lightwave system was limited by the fiber loss at the operating wavelength of $1.3\,\mu m$ (typically $0.5\,dB/km$). Losses of silica fibers become minimum near $1.5\,\mu m$; for example, a $0.2\,dB/km$ loss was realized in 1979 in this spectral region. However, the introduction of third-generation lightwave systems operating at $1.5\,\mu m$ was considerably delayed by a large fiber chromatic dispersion near $1.5\,\mu m$. By 2005, thanks to the development of dispersion-shifted

fibers, the $1.5\,\mu m$ systems have achieved $BL \sim 100\,THz \cdot km$. In the fourth generation of lightwave systems, optical amplification was used for increasing the repeater spacing L while wavelength-divison multiplexing (WDM) technology was developed to increase the bit rate B. The current systems attempt to increase the bit rate for each wavelength channel. Starting in 2000, many experiments used channels operating at $40\,GHz$; migrating toward $160\,GHz$ is also likely in the future.

With the advent of optical amplifiers, fiber losses are no longer a major limiting factor for optical communication systems. Indeed, modern lightwave systems are often limited by the dispersion and nonlinear effects rather than fiber losses. In some sense, optical amplifiers solve the loss problem but, at the same time, worsen the dispersion problem. As a result, dispersion-induced degradation of the transmitted signal accumulates over multiple amplifiers. The system may then become dispersion limited, in which case an electronic repeater or dispersion compensation is necessary. Further, the bit rate has been increased to over $10\,GHz$ for current communication systems in which dispersion and fiber nonlinearity become important issues for long-haul transmission.

1.1.2 Fibers as Light Waveguide

Optical fibers are almost always made from silica which is a dielectric (non-conductive) material. Due to the phenomenon of total internal reflection, optical fibers are used as a light-guiding medium to send light energy for communication. Optical fibers consist of three parts: the core, the cladding, and the coating or buffer. The cylindrical core of silica glass is surrounded by a cladding whose refractive index is lower than the core. Because of an abrupt index change at the core-cladding interface, such fibers are called step-index (SI) fibers. In a more complex fiber, known as graded-index fibers, the refractive index decreases gradually inside the core.

Electric Properties of Dielectric material

In order to understand the lightwave propagation in optical fibers, we need some basic knowledge of electric properties of a dielectric material. When light pulses

propagate in an optical fiber, an electric field can shift the average position of electrons in the dielectric fiber, resulting in a polarization of the fiber material. The effect of polarization $\mathbf{P}$ is expressed mathematically by [4]

$$\mathbf{P} = -en_e\xi(\mathbf{E}) \tag{1.1}$$

where n_e is the density of electrons that participate in the polarization and ξ represents the displacement of the electron position in each molecule induced by the electric field $\mathbf{E}$.

In many dielectric materials, including optical fibers, the dielectric response to electric field $\mathbf{E}$ is not linear, and the index of refraction can be expressed as

$$n(\omega, |\tilde{\mathbf{E}}|^2) = n(\omega) + n_2(\omega)|\tilde{\mathbf{E}}|^2 \tag{1.2}$$

where ω is the angular frequency and $\tilde{\mathbf{E}}$ denotes the electric field in the frequency domain. While the first term $n(\omega)$ on the right-hand of Eq. (1.2) is the usual refractive index, the second term $n_2(\omega)|\tilde{\mathbf{E}}|^2$ is a nonlinear correction, referred as the Kerr effect, in which n_2 represents the coefficient of the nonlinear response or Kerr coefficient. However, for an optical fiber material, the value of n_2 is very small and typically is about $10^{-12}\,(m/V)^2$. For example, for an optical pulse with a typical power $1\,mW$ and an effective mode area $A_{eff} = 55\,\mu m^2$, the electric field of lightwave in fibers has a value around $10^5\,V/m$; the nonlinear correction of the index of refraction is about 1 part in 10^{-12}.

For most of applications, it is sufficient to approximate the polarization as a linear function of the electric field,

$$\tilde{\mathbf{P}}(\omega) = \chi(\omega)\tilde{\mathbf{E}}(\omega), \tag{1.3}$$

and the electric displacement vector, $\tilde{\mathbf{D}}(\omega)$, can be expressed as

$$\tilde{\mathbf{D}}(\omega) = \varepsilon_0\tilde{\mathbf{E}}(\omega) + \tilde{\mathbf{P}}(\omega). \tag{1.4}$$

where $\varepsilon_0 = 8.864 \times 10^{-12}\,F/m$ is the dielectric constant of the vacuum. Eq. (1.3) and Eq. (1.4) yield a linear relation between $\tilde{\mathbf{D}}$ and $\tilde{\mathbf{E}}$,

$$\tilde{\mathbf{D}}(\omega) = \varepsilon_0\varepsilon^*(\omega)\tilde{\mathbf{E}}(\omega) \tag{1.5}$$

Here, ε^* is the relative permittivity constant of the material, and the refractive index is given by

$$n(\omega) = \frac{ck}{\omega} = \sqrt{\varepsilon^*} \tag{1.6}$$

where k is the wave number.

Single Mode Fiber

When light propagates in an optical fiber, only discrete optical modes are supported in the fiber core. Depending on the number of supported (or guided) modes, optical fibers are classified as multimode fiber and single mode fiber. In this thesis, we mostly consider single mode fibers.

In fact, optical modes are the solutions of the wave equation [5]

$$\nabla^2\tilde{\mathbf{E}} + \frac{n^2\omega^2}{c^2}\tilde{\mathbf{E}} = 0 \tag{1.7}$$

with appropriate boundary conditions; these solutions have the property that their spatial distributions do not change with propagation. In general, the solutions of the wave equation have non-zero E_z and H_z; therefore, fiber modes are denoted by HE_{mn} or EH_{mn}, depending on whether H_z or E_z dominates. While a multimode fiber allows for a larger number of modes, a single mode fiber is designed to support only the fundamental HE_{11} mode at a certain wavelength of operation. Further, the number of modes supported by a fiber depends on its refractive index profile and other fiber parameters.

While both single mode and multimode fibers can have a step-index or graded-index profile, single mode fiber production is almost exclusively step-index because the performance advantages for single mode graded-index fibers compared to single mode step-index fibers are relatively small. For a step-index fiber, the refractive index profile has the form

$$n = \begin{cases} n_1; & \rho \leq a, \\ n_2; & \rho > a. \end{cases} \tag{1.8}$$

where a is the core radius and ρ is the radial coordinate. An important parameter in fiber design is the cutoff condition V defined as

$$V = \frac{2\pi}{\lambda} a \sqrt{n_1^2 - n_2^2}. \tag{1.9}$$

A fiber designed such that $V < 2.405$ supports only the fundamental HE_{11} mode, while a fiber with a larger V supports many modes. Hence, $V < 2.405$ is the single mode condition. According to Eq. (1.9), a single mode fiber must have smaller core radius compared to a multimode fiber. Indeed, most single mode fibers are designed with $a \approx 4\,\mu m$, while the typical core radius of multimode fibers is $a \approx 25\,\mu m$. Further, a single mode fiber is also designed such that $\Delta = (n_1 - n_2)/n_1 \ll 1$, which results in negligible axial components E_z and H_z; hence, a single mode fiber actually supports two orthogonally linearly polarized modes which are degenerate in an ideal circular fiber.

A single mode fiber exhibits no dispersion caused by multiple modes, which greatly increase the transmission bit rate and distance. Hence, while multimode fibers are mostly used in short distance applications such as LAN systems and video surveillance, single mode fiber is best designed for telecommunications and high capacity applications, such as multichannel television broadcast systems.

While replacing multimode fiber with single mode fiber has made telecommunication possible, transmission signals still suffer from chromatic dispersion (CD) and polarization mode dispersion (PMD). Both CD and PMD cause temporal spreading of optical bits as they propagate along the fiber. For data rates equal to or higher than 10 Gb/s, these two effects could cause severe deterioration in optical signals for long-haul transmission systems [6–8].

While the next section gives a full introduction to PMD, we provide some background material on chromatic dispersion in the following paragraph. Chromatic dispersion includes both material dispersion and waveguide dispersion. While material dispersion is caused by the variation of the refractive index of silica as a function of wavelength, waveguide dispersion is due to the waveguiding property of the fiber. The dispersion associated with the waveguide structure can be designed to have different signs; therefore the material dispersion and waveguide dispersion can be balanced at the "zero dispersion" wavelength. While, initially, fiber with

zero dispersion was manufactured near 1310 nm, dispersion-shifted fibers (DSF) were developed to move the zero-dispersion point to the 1550 nm region in which fiber attenuation meets its minimum. Chromatic dispersion is basically compensated through two approaches in modern communication systems: while the most common technique uses dispersion-shifted fibers, a more expensive solution employs the chirped fiber Bragg grating [9].

1.1.3 Polarization Mode Dispersion

An single mode fiber supports only the fundamental mode HE_{11}. In general, an optical wave of arbitrary polarization can be represented as the linear superposition of two orthogonally polarized HE_{11} modes. For an ideal fiber formed as a cylindrically symmetric waveguide, the two HE_{11} modes are degenerate since they propagate with the same properties, which is the source of the term "single mode". However, random birefringence in real optical fibers removes the degeneracy, resulting in two distinct HE_{11} polarization modes with distinct phase velocities, v_{px} and v_{py}, and group velocities, v_{gx} and v_{gy} [10–12]. In the time domain, polarization mode dispersion (PMD) leads to pulse broadening, which in the lowest order yields a time delay ΔT between the two HE_{11} modes that is termed differential group delay (DGD). PMD can also be viewed in the frequency domain, in which the difference of phase velocities, $\Delta v_p = v_{px} - v_{py}$, results in the rotation of the polarization along the fiber length [12, 13]. Further, Δv_p is also frequency dependent; therefore, for a fixed input polarization, the output polarization changes with frequency ω. Due to the random nature of the fiber birefringence, polarization mode dispersion is stochastic and hence a far more complex phenomenon than chromatic dispersion.

Polarization effects of optical fibers were first studied in 1961 by Snitzer and Osterberg. However, they have historically played a minor role in the development of lightwave systems, since commercial optical receivers detect optical power rather than optical field and thus are insensitive to polarization. In the last decade, polarization has become an important issue in lightwave systems as a result of two developments [14]. First, the advent of the optical amplifier has dramatically increased the transmission distance, resulting in a non-negligible pulse distortion

due to the accumulation of polarization mode dispersion (PMD) along fiber length. Further, the development of transmitter and receiver technologies have increased the bit rates in optical communication systems. To satisfy the ever-increasing demand for communication capacity, optical systems are migrating from the current 10 Gb/s to 40 Gb/s or higher. In such high bit rate and long haul communication systems, PMD effects can be a limiting factor [3, 8, 15–17].

Jones Calculus

To deal with modern polarization effects, we employ Jones Calculus [18]: if we view an optical system as a black box, the input or output of the box is an optical field which can be represented as a Jones Vector; assuming a linear response of the optical system to the input field, the black box can be represented as a Jones Matrix.

In general, we express the plane-wave components of an optical field as

$$\begin{aligned} E_x(z,t) &= E_{0x}e^{i(\kappa z-\omega t+\delta_x)} \\ E_y(z,t) &= E_{0y}e^{i(\kappa z-\omega t+\delta_y)} \end{aligned} \tag{1.10}$$

where E_{0x} and E_{0y} are complex quantities. When the common phase $\kappa z - \omega t$ is suppressed, Eq. (1.10) yields

$$\begin{aligned} E_x(z,t) &= E_{0x}e^{i\delta_x} \\ E_y(z,t) &= E_{0y}e^{i\delta_y}. \end{aligned} \tag{1.11}$$

A Jones vector is a 2×1 column matrix $\mathbf{E}$ used to represent the two components of the optical field according to Eq. (1.11), such that

$$\mathbf{E} = \begin{pmatrix} E_x \\ E_y \end{pmatrix} = \begin{pmatrix} E_{0x}e^{i\delta_x} \\ E_{0y}e^{i\delta_y} \end{pmatrix}, \tag{1.12}$$

and the total intensity I of the optical field is given by

$$I = \mathbf{E}^+ \cdot \mathbf{E} = E_x E_x^* + E_y E_y^* = E_{0x}^2 + E_{0y}^2 \tag{1.13}$$

where $\mathbf{E}^+$ is the complex transpose of the Jones vector $\mathbf{E}$. Note that Eq. (1.12) is the general expression of the Jones vector for elliptically polarized light, and the Jones vector can only be used to describe completely polarized light.

In the Jones calculus, optical components, such as polarizers, waveplates, and optical fibers, can be represented by 2×2 matrices. For a linear system, the components of the output field can be expressed as linear superpositions of the input components, i.e.,

$$\begin{aligned} E_x^o &= T_{xx}(\omega)E_x^i + T_{xy}(\omega)E_y^i \\ E_y^o &= T_{yx}(\omega)E_x^i + T_{yy}(\omega)E_y^i \end{aligned} \tag{1.14}$$

where E_x^o and E_y^o are the components of the emerging beam, and E_x^i and E_y^i are the components of the incident beam. The quantities T_{ij}, $i, j = x, y$, are the frequency dependent transforming factors. Equation (1.14) can be written in the matrix form as

$$\begin{pmatrix} E_x^o \\ E_y^o \end{pmatrix} = \begin{pmatrix} T_{xx} & T_{xy} \\ T_{yx} & T_{yy} \end{pmatrix} \begin{pmatrix} E_x^i \\ E_y^i \end{pmatrix} \tag{1.15}$$

or

$$\mathbf{E}^o = T(\omega)\mathbf{E}^i, \tag{1.16}$$

in which the 2×2 matrix $T(\omega)$ is called the Jones matrix, or transfer matrix.

Usually, an optical fiber is considered as a linear medium, and hence can be described by its complex transfer matrix $T(\omega)$. By further assuming no polarization-dependent loss, $T(\omega)$ takes the form

$$T(\omega) = e^{\beta(\omega)}U(\omega) \tag{1.17}$$

where $\beta(\omega)$ is in general complex and $U(\omega)$ is an unitary matrix,

$$U(\omega) = \begin{pmatrix} u_1(\omega) & u_2(\omega) \\ -u_2^*(\omega) & u_1^*(\omega) \end{pmatrix} \tag{1.18}$$

with $|u_1|^2 + |u_2|^2 = 1$.

The Principal States of Polarization

The polarization effect of an optical fiber can be fully characterized by its frequency dependent transfer matrix $T(\omega)$ [1, 19–23]. For a polarization-maintaining (PM) fiber with constant birefringence, this transfer matrix has two eigenmodes which coincide with the two principal axes of birefringence of the fiber. Optical pulses polarized along these two eigenmodes have a maximum or minimum group delay. Unlike the PM fiber, the birefringence of real fiber changes randomly along the fiber length in both magnitude and orientation [14]. However, early in 1986, Poole and Wagner proved that for narrow-band pulses there exists a set of two orthogonal input states of polarization for which the corresponding output states of polarization are independent of frequency to first order [20]. These two input states are termed the principal states of polarization (PSP). In general, an input wave initially aligned with a principal state will evolve through varying states of polarization as it propagates, in contrast to an eigenmode in a PM fiber which propagates unchanged. The statistics of the evolution of the principal states of random birefringent fibers have been analyzed theoretically [24] and experimentally measured [24–26]. Later in 1999, Shieh proved that principal states of polarization exist in random birefringent fibers regardless of the spectral components of the optical pulses [27]. These PSPs are collective effects of the birefringence over the entire fiber length, and may not necessarily be correlated with the local fiber birefringence. In the following, for more insight into PMD phenomena, we briefly review the derivation of the PSPs for narrow-band optical pulses.

To demonstrate the existence of the PSP, the complex field vectors $\mathbf{E}^{i,o}$ can be expressed as

$$\mathbf{E}^{i,o} = \begin{bmatrix} E_x^{i,o} \\ E_y^{i,o} \end{bmatrix} = \varepsilon_{i,o} e^{j\phi_{i,o}} \hat{\varepsilon}_{i,o}, \tag{1.19}$$

where $j \equiv \sqrt{-1}$, $\varepsilon_{i,o}$ and $\phi_{i,o}$ are the amplitudes and phases of the input field (denoted by i) and output field (denoted by o), and $\hat{\varepsilon}_{i,o}$ are complex unit vectors specifying the states of polarization of the corresponding fields. For a constant input field $\mathbf{E}^i$, the output field from an optical fiber characterized by a transfer

matrix $T(\omega)$ can be calculated according to

$$\mathbf{E}^o(\omega) = T(\omega)\mathbf{E}^i \tag{1.20}$$

Expressing $T(\omega)$ according to Eq. (1.17) and combining the frequency derivatives of Eq. (1.19) and Eq. (1.20) yields

$$\varepsilon_o e^{j\phi_o} \frac{d\hat{\varepsilon}_o}{d\omega} = e^{\beta}(U' - jkU)\mathbf{E}^i \tag{1.21}$$

where

$$k = \phi_o' + j\left(\beta' - \frac{\varepsilon_o'}{\varepsilon_o}\right). \tag{1.22}$$

For input states of polarization that give zero dispersion in the output state to first order, we have

$$\frac{d\hat{\varepsilon}_o}{d\omega} = 0, \tag{1.23}$$

and Eq. (1.21) becomes

$$(U' - jkU)\hat{\varepsilon}_i = 0. \tag{1.24}$$

Solving Eq. (1.24) yields two eigenvectors:

$$\hat{\varepsilon}_{i\pm} = e^{j\rho} \begin{bmatrix} \frac{u_2' - jk_\pm u_2}{D_\pm} \\ -\frac{u_1' - jk_\pm u_1}{D_\pm} \end{bmatrix} \tag{1.25}$$

where

$$k_\pm = \pm\sqrt{|u_1'|^2 + |u_2'|^2}, \tag{1.26}$$

$$D_\pm = \sqrt{2k_\pm[k_\pm - Im(u_1^* u_1' + u_2^* u_2')]} \tag{1.27}$$

and ρ is an arbitrary phase. The solutions $\hat{\varepsilon}_{i+}$ and $\hat{\varepsilon}_{i-}$ form the input PSPs of the fiber medium. The corresponding two output PSPs, i.e., $\hat{\varepsilon}_{o+}$ and $\hat{\varepsilon}_{o-}$ can be easily obtained from Eq. (1.20).

The existence of the input PSPs of a random birefringent fiber ensures that an optical pulse that has a narrow spectral width and is aligned with either of the two principal states at the input will remain polarized to first order after propagating through the medium. Further, the input PSPs form an orthogonal pair:

$$\hat{\varepsilon}_{i+} \cdot \hat{\varepsilon}_{i-}^* = 0 \quad and \quad \hat{\varepsilon}_{i\pm} \cdot \hat{\varepsilon}_{i\pm}^* = 1. \tag{1.28}$$

The orthogonality of the input PSPs can be used as basis vectors for a phenomenological description of polarization dispersion. Therefore, an input wave of arbitrary polarization can be decomposed into two waves, one having polarization $\hat{\varepsilon}_{i+}$ and the other $\hat{\varepsilon}_{i-}$. These two waves travel with maximum velocity v_{g+} and minimum velocity v_{g-} compared to waves in other polarizations; therefore, the principal state associated with the maximum group velocity is termed fast PSP, while the other is called slow PSP. The propagation delay difference between these two pulses, one polarized along the slow PSP, and the other along the fast PSP, i.e., $\tau = \tau_+ - \tau_-$, is termed the differential group delay (DGD). Typical mean values of DGD are 1 to 50 ps for 500-km long fiber, depending on fiber and cable attributes.

Stokes Vector

Instead of using a Jones vector, polarization state of light can also be completely described by a Stokes vector

$$\hat{s} = \begin{pmatrix} s_1 \\ s_2 \\ s_3 \end{pmatrix} \tag{1.29}$$

with $s_1^2 + s_2^2 + s_3^2 = s_0^2$. The parameter s_0 is the total intensity of light, the parameter s_1 describes the amount of linear horizontal or vertical polarization, the parameter s_2 describes the amount of linear $+45^o$ or -45^o polarization, and the parameter s_3 describes the amount of linear horizontal or vertical polarization. The Stokes parameters can be expressed by the components of the corresponding Jones vector $\mathbf{E} = [E_x, E_y]^t$ as

$$\begin{aligned} s_1 &= E_x E_x^* - E_y E_y^* \\ s_2 &= E_x E_y^* + E_x^* E_y \\ s_3 &= j(E_x E_y^* - E_x^* E_y). \end{aligned} \tag{1.30}$$

Usually, these two vectors are normalized for the representation of polarization states so that $E_x^2 + E_y^2 = 1$ and $s_1^2 + s_2^2 + s_3^2 = 1$.

PMD Characterization

While polarization mode dispersion of an optical fiber can be fully characterized by the Jones matrix $T(\omega)$ of the fiber system as a function of light frequency ω, a convenient representation of the PMD evolutions may be made in terms of a PMD vector $\boldsymbol{\tau} = \tau\hat{p}$, which is a Stokes vector pointing in the direction of the slow PSP $\hat{p}$ with a length equal to the DGD τ [11, 28, 29]. The PMD vectors are directly connected with the transfer matrix $T(\omega)$ by:

$$i\frac{dT}{d\omega} = \frac{1}{2}\boldsymbol{\tau}(\omega)\cdot\boldsymbol{\sigma}, \tag{1.31}$$

in which $\boldsymbol{\sigma} = [\sigma_1, \sigma_2, \sigma_3]^t$ represents the Pauli spin vector, with components

$$\sigma_1 = \begin{pmatrix} 1 & 0 \\ 0 & -1 \end{pmatrix}, \quad \sigma_2 = \begin{pmatrix} 0 & 1 \\ 1 & 0 \end{pmatrix}, \quad \sigma_3 = \begin{pmatrix} 0 & -j \\ j & 0 \end{pmatrix}. \tag{1.32}$$

If polarized light is launched into an optical fiber with a PMD vector $\boldsymbol{\tau}(\omega)$, its output state of polarization is determined by

$$\frac{d\hat{s}(\omega)}{d\omega} = \boldsymbol{\tau}(\omega)\times\hat{s}(\omega). \tag{1.33}$$

In general, for an optical pulse with a carrier frequency ω_0 and bandwidth $\Delta\omega$, the frequency dependent PMD vector can be Taylor expanded as [30]

$$\boldsymbol{\tau}(\omega) \approx \boldsymbol{\tau}(\omega_0) + \boldsymbol{\tau}_\omega(\omega_0)(\omega-\omega_0) + \boldsymbol{\tau}_{\omega\omega}(\omega_0)(\omega-\omega_0)^2 + \cdots \tag{1.34}$$

where $\boldsymbol{\tau}_\omega = \partial\boldsymbol{\tau}/\partial\omega$ and $\boldsymbol{\tau}_{\omega\omega} = \partial^2\boldsymbol{\tau}/\partial\omega^2$. In Eq. (1.34), $\boldsymbol{\tau}(\omega_0)$, $\boldsymbol{\tau}_\omega(\omega_0)$, and $\boldsymbol{\tau}_{\omega\omega}(\omega_0)$ represent first order, second order, and third order PMD, respectively. While higher order PMD may have non-negligible impact on modern communication for wide-bandwidth pulses [31–34], for optical pulses in current communication systems, it is sufficient to describe the PMD up to second order, such that $\boldsymbol{\tau}(\omega) \approx \boldsymbol{\tau}(\omega_0) + \boldsymbol{\tau}_\omega(\omega_0)(\omega-\omega_0)$. The standard physical picture of the first order PMD considers an input pulse split into two PSPs according to the orientation of the input polarization state relative to the slow PSP $\hat{p}$ [28]. On propagation through the fiber the two pulses are differentially delayed by the DGD τ. Due to the stochastic nature of the

PMD phenomena, the PMD vector not only changes with optical frequency but also varies randomly with time as well as along the fiber length. Both theoretical analysis and experimental measurement provide strong evidence that the three components of $\boldsymbol{\tau}(\omega_0) = [\tau_1, \tau_2, \tau_3]^t$ are asymptotically Gaussian distributed and the DGD τ is asymptotically Maxwellian distributed [35–39]. Moreover, for fiber lengths much longer than its coupling length, the root mean square of the DGD grows as the square root of fiber length [19,35,37]. The second-order PMD (SOPMD) describes the lowest order contribution to the wavelength dependence of the DGD and has two components: depolarization and polarization dependent chromatic dispersion (PDCD). SOPMD causes the principal polarization modes to broaden as shown in Fig. 1.2.

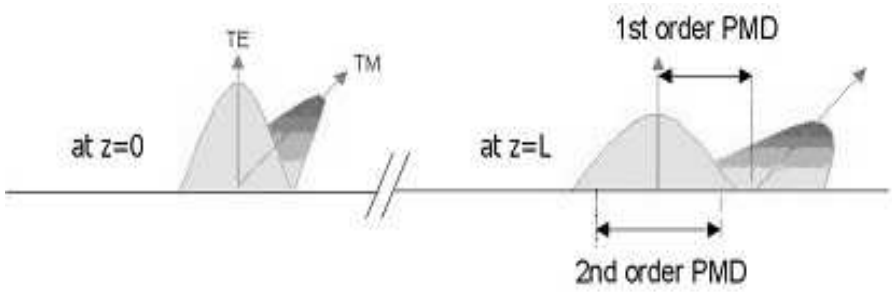

Figure 1.2: Pulse broadening caused by 1st order PMD and 2nd order PMD.

1.1.4 Fiber Birefringence

Fiber birefringence is the physical origin of polarization mode dispersion and can be fully described by the local, frequency dependent, birefringence vector defined as $\mathbf{b}(\omega, z) = [\boldsymbol{\beta}_1(\omega, z) - \boldsymbol{\beta}_2(\omega, z)]/2$ [40]. The quantities $\boldsymbol{\beta}_1(\omega, z)$ and $\boldsymbol{\beta}_2(\omega, z)$ are the propagation constants (in the absence of polarization-dependent-loss) of monochromatic light polarized along or orthogonal to the principal birefringence axis, which is the polarization direction with the smallest group velocity that does not change to first order with light frequency. However, in many applications the frequency variation of the birefringence is characterized simply by the birefringence strength and the group delay per unit length at the carrier frequency ω_0, namely

$b(z) = b(\omega_0, z)$ and $b'(z) = b'(\omega_0, z)$ as well as the orientation, $\theta(z)$, of the principal birefringence axis angle with respect to some fixed coordinate direction [30, 41, 42]. Given the random birefringence vector $\mathbf{b}(z)$ of an optical fiber, the evolution of the PMD vector with distance z is determined according to the dynamical PMD equation [11, 39]

$$\frac{\partial \boldsymbol{\tau}}{\partial z} = \frac{\partial \mathbf{b}}{\partial z} + \mathbf{b} \times \boldsymbol{\tau}. \tag{1.35}$$

In this section, we discuss the birefringence mechanism, existing theoretical models for generating the random birefringence vector $\mathbf{b}(z)$ and experimental studies.

Birefringence Mechanism

Fiber birefringence results from various perturbations that act on a single mode fiber. These perturbations can be classified as intrinsic and extrinsic perturbations [14, 43]. Intrinsic perturbations, such as the noncircular core and nonsymmetrical stress fields in the glass around the core region, are introduced by the manufacturing process. A noncircular core gives rise to geometric birefringence, whereas a nonsymmetrical stress field creates stress birefringence, c.f. Fig. 1.2 (a). Although these two birefringence sources are permanent, they are longitudinally varying along the fiber and may vary from fiber to fiber as well. Fiber birefringence also results from external forces, such as lateral stress of the fiber, fiber bending, and fiber twisting c.f. Fig. 1.3 (b). All three forces are usually present to some extent in spooled and field-installed telecommunication fibers. Due to the dynamic nature of the extrinsic forces, the resulting birefringence changes unpredictably with time. In other words, both the intrinsic and extrinsic perturbations exist unavoidably in real optical fibers, and the magnitude and orientation of the birefringence typically varies with time, distance along the fiber, and among fiber samples.

Fiber Birefringence Modeling

While the birefringence vector $\mathbf{b}(z, \omega)$ describes all PMD sources, the detailed structure of the fiber birefringence map has not been fully understood. To facilitate the study of PMD phenomena, a statistical model of fiber birefringence was first advanced in 1991 by Foschini and Poole [30], which we term the Foschini-Poole model.

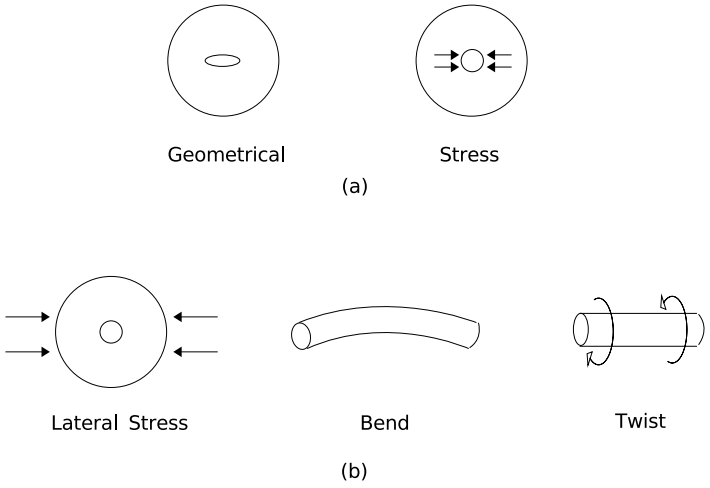

Figure 1.3: (a) Intrinsic and (b) extrinsic mechanisms of fiber birefringence.

In this model, the polarization-dependent properties of a single mode fiber is represented by a real 3×3 rotation matrix which is a product of two matrix components: a length-independent background component and a small length dependent perturbation. This model predicts that optical fibers have nearly fixed birefringence axes, varying only slightly but rapidly along the fiber length. Later in 1996, Wai and Menyuk proposed another two additional birefringent models, namely the fixed and random modulus models (FMM and RMM) [41]. The FMM assumes a randomly varying birefringence axis but a fixed birefringence strength, while the RMM assumes that both quantities vary randomly. While earlier PMD studies are based on the Foschini-Poole model, most recent works have employed the two Wai-Menyuk birefringent models. The following part of this section will introduce these two birefringence models, i.e., the FMM and RMM, in greater details.

In the FMM, the birefringence strength b and the specific group delay per unit length b' at carrier frequency ω_0 are assumed constant along the fiber, and are

determined by the beat length Λ_{beat}, defined by [44]

$$b = \frac{\pi}{\Lambda_{beat}}, \quad b' = \frac{b}{\omega_0} . \tag{1.36}$$

The rate of change of the birefringence orientation θ is modeled by a white noise process $g_\theta(z)$,

$$d\theta/dz = g_\theta(z), \quad \langle g_\theta(z)\rangle = 0, \quad \langle g_\theta(z) g_\theta(z')\rangle = \sigma_\theta^2 \delta(z - z') . \tag{1.37}$$

The variance $\sigma_\theta^2 = 2/L_{corr}$ is given by

$$\begin{aligned} \langle \mathbf{b}(0)\mathbf{b}(z)\rangle &= b^2 \langle \cos[\theta(z) - \theta(0)]\rangle \\ &\equiv b^2 exp\left(-\frac{z}{L_{corr}}\right) \end{aligned} \tag{1.38}$$

where L_{corr} is the fiber correlation length.

In the RMM, the birefringence vector obeys the Langevin process,

$$\frac{d\mathbf{b}}{dz} = -a\,\mathbf{b}(z) + \mathbf{g}(z) \tag{1.39}$$

where $\mathbf{g}(z)$ is an isotropic Gaussian white noise vector with

$$\langle \mathbf{g}(z)\rangle = 0, \quad \langle \mathbf{g}(z)\mathbf{g}(z')\rangle = \sigma^2 \delta(z - z') . \tag{1.40}$$

Eq. (1.39) has the solution

$$\mathbf{b}(z) = \mathbf{b}(0)\, exp(-az) + \int_0^z dz' \mathbf{g}(z')\, exp(az' - az) . \tag{1.41}$$

Here $a = 1/L_{corr}$ and $\sigma^2 = b_{rms}^2/L_{corr}$ are determined by imposing the conditions $\langle \mathbf{b}(0)\mathbf{b}(z)\rangle = b^2(0)\, exp(-z/L_{corr})$ and $\lim_{z\to\infty}\langle b^2(z)\rangle = b_{rms}^2$ where $b_{rms} = \pi/\Lambda_{beat}$. If we denote $b(n) = b(\omega_0, n)$ and $b'(n) = b'(\omega_0, n)$ as two random series, we can calculate

$$b'(n) = \frac{b(n)}{\omega_0} . \tag{1.42}$$

Experimental Studies

Early research on fiber birefringence mostly consisted of experimental studies that focused on limited issues of fiber birefringence, such as the influence of various fiber imperfections on polarization states [45–48], and measurements of birefringence strength or fiber beat length of polarization-maintaining fibers [43, 49]. More recently, birefringence parameters of standard single mode fibers, such as birefringence strength, beat length and correlation length, have been successfully measured by several techniques such as optical frequency domain reflectometer (OFDR)-based techniques [50–52], and polarization optical time domain reflectometer (POTDR)-based techniques [53–59]. Based on these two types of techniques, the spatial distributions of birefringence have also been indirectly measured and reported [52, 53, 57, 59]. Figure 1.4 is one of the typical experimental results of spatial distribution of birefringence in a standard (a) step-index (SI) fiber and (b) Dispersion-shifted fiber (DSF), while Fig. 1.5 presents corresponding histograms of the measured fiber local birefringence [57]. Experiment studies of fiber birefringence have revealed three important statistical features. In the first of these, fiber birefringence not only varies randomly in orientation but also in magnitude, c.f. Fig. 1.4. Second, the probability density function of the birefringence strength is a Rayleigh distribution or at least close to a Rayleigh distribution, c.f. Fig. 1.5. Further, the fluctuation amplitude of the random birefringence strength varies from fiber to fiber, and is the value of the order of the birefringence strength itself, c.f. Fig. 1.4. These features are consistent with the prediction of the RMM, but not the FMM or the Foschini-Poole model.

1.2 Motivation of the thesis

As the data rate continually increases for larger transmission capacity, polarization mode dispersion (PMD) becomes an increasingly important limitation in fiber communication systems. While PMD has been studied extensively in the field of fiber-optic communication, the exact behavior of the birefringence fluctuations in a fiber and their influence on the evolution of the PMD along the fiber length has

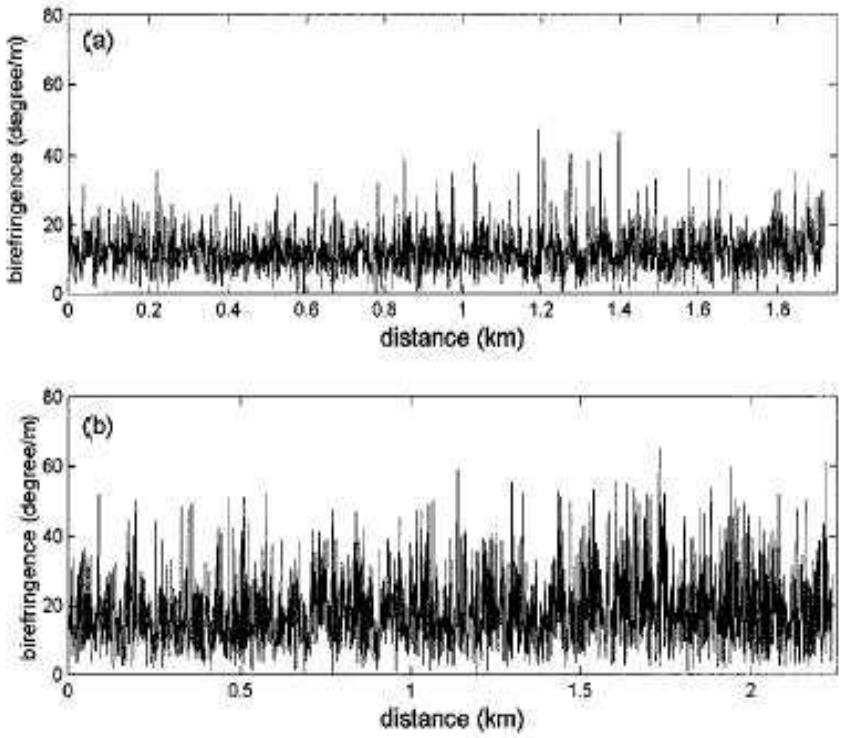

Figure 1.4: Birefringence spatial distribution of (a) an SI optical fiber and (b) DSF.

not been carefully studied, presumably because of the difficulty of measuring small birefringence variations over long distances. On the other hand, for a complete description of PMD and PMD related issues, a detailed birefringence profile is indispensable. Although the random-modulus model (RMM) is the only model that is consistent with the experimental results of fiber birefringence, c.f. section 1.1.4, these results are measured for only a limited number of optical fibers. However, according to the birefringence mechanisms, different manufacturing processes and external environments may result different statistical features of fiber birefringence. Therefore, while the existing three simple birefringence models may be applicable to certain birefringence profiles, general models are still missing for the description

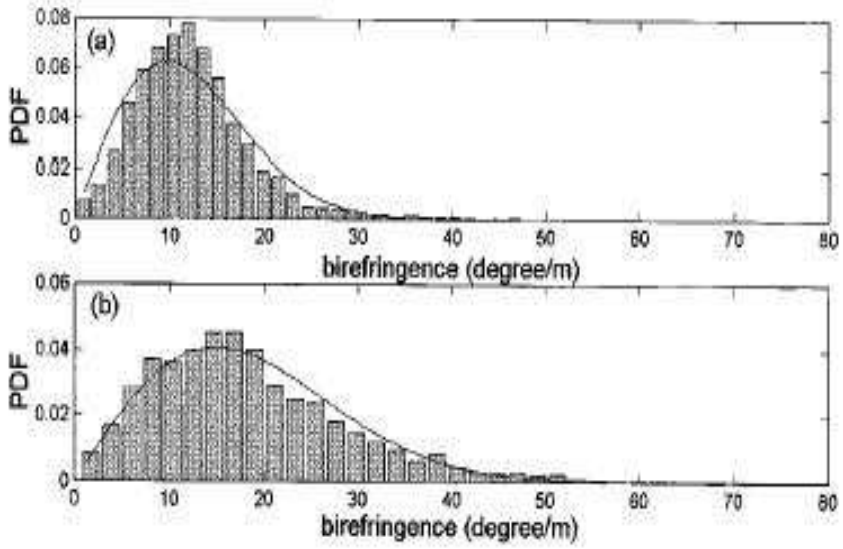

Figure 1.5: (a) Histogram of the SI fiber local birefringence. (b) Histogram of the DSF fiber local birefringence. The solid curves represent the data fit by a Rayleigh distribution.

of a broad range of fiber birefringence. The motivation of this thesis is therefore to develop improved fiber birefringence models and to apply these models to determine the detailed properties of PMD as a function of fiber length.

1.3 Organization of the thesis

This section outlines the structure of this thesis. Chapter 1 introduces the background knowledge, the motivation of the thesis together with its organization. While Chapter 2 describes our general birefringence models and mathematical algorithms for numerical implementing these models, Chapter 3 applies these models as well as the two existing models to the studies of polarization mode dispersion (PMD) in standard single mode fibers. In Chapter 4, the author investigates the PMD reduction of sinusoidally spun fibers and various procedures for PMD compensation. Chapter 5 finally describes pulse distortion caused by the nonlinear

PMD. Chapter 6 concludes the thesis.

Chapter 2

Improved Fiber Birefringence Modeling

To study polarization mode dispersion (PMD) and PMD-related phenomena, two simple models are generally employed to describe the variation of the birefringence along a fiber length. These are the FMM and RMM. While the FMM typically applies to intrinsically stressed or elliptical fibers with large and nearly constant birefringence strengths in which only the birefringence orientation is susceptible to small perturbations, the RMM is more relevant to ultra-low PMD fibers for which both the birefringence strength and orientation vary substantially along the fiber as a result of random profile fluctuations. However, fiber birefringence results from both intrinsic profile variations and external perturbations, leading to characteristic birefringence profiles. For example, the amplitude of the birefringence strength variations may be far larger or far smaller than those of the birefringence orientation. Further, either the strength or the orientation of the birefringence can vary independently at different rates as a result of different manufacturing conditions and external environments. To model as wide a range of birefringence behavior as possible, we have accordingly considered four models for the longitudinal variation of the birefringence. Our models A1 and B1 interpolate between the constant birefringence model and the RMM, while models A2 and B2, which reproduce the FMM in a certain limit, extend our results to a broader range of birefringence pro-

files. In this chapter, we examine these four models analytically and numerically. Practical results of the physical application of the models together with a study of their implications on the statistics of the PMD fluctuations are presented in the next chapters.

2.1 Langevin Equations

In this section, we propose two procedures, labeled A and B, for simulating birefringence. Our starting point is the Langevin equation [60], which is employed, as in the RMM, to generate random fluctuations in the birefringence. Denoting either of the two orthogonal components of the birefringence vector $\mathbf{b}(z)$ by a single variable $x(z)$, this equation is :

$$\frac{dx}{dz} = -a\,x(z) + g(z) \tag{2.1}$$

in which $g(z)$ represents Gaussian white noise with

$$\langle g(z)\rangle = 0\,, \quad \langle g(z)g(z')\rangle = \sigma^2\delta(z-z')\,. \tag{2.2}$$

The contribution from $-a\,x(z)$ in Eq. (2.1) then counteracts the fluctuations in x that are induced by the random noise $g(z)$, in such a manner that the mean value of x is zero, which is the expected result for fibers subject to random perturbations. Polarization-maintaining fibers or fibers subject to systematic stresses, however, would have a non-zero mean value of x requiring modifications to the model.

To generalize the above Langevin formalism to the case of optical fibers for which the birefringence vector possesses a non-zero mean amplitude, an additional term must be introduced. This is done in two ways below.

2.1.1 Procedure A

In our first procedure, Eq. (2.1) is modified through the inclusion of an additional term

$$\ddot{x}(z) + k_2\dot{x}(z) + k_1 x(z) = g(z) \tag{2.3}$$

where $\dot{x}(z)$ and $\ddot{x}(z)$ are, respectively, the first and second derivatives of the birefringence x with respect to the fiber length z . Here $-k_2\,\dot{x}(z)$ and $-k_1\,x(z)$ effectively apply damping and restoring forces to the fluctuations generated by $g(z)$ with $k_1, k_2 > 0$. Adjusting the ratio between k_1 and k_2, therefore changes the magnitude of the overall fluctuations in $x(z)$.

Eq. (2.3), can be recast in standard fashion as two simultaneous first order differential equations:

$$\begin{aligned} \frac{dx}{dz} &= v(z) \\ \frac{dv}{dz} &= -k_1\,x(z) - k_2\,v(z) + g(z) \end{aligned} \tag{2.4}$$

The parameter v then represents the rate of change of the birefringence. As we have verified through numerical simulation, Eq. (2.4) evolves into the same stable solution independent of the initial condition $v(0)$. Therefore, to simply the analysis, we have set $v(0) = 0$.

The analytic solution of Eq. (2.4) is given by

$$x(z) = exp(-\lambda_1 z)[c_1 + G_1(z)] + exp(-\lambda_2 z)[c_2 + G_2(z)] \tag{2.5}$$

with

$$\begin{aligned} \lambda_1 &= \frac{1}{2}\left[k_2 - (k_2^2 - 4k_1)^{1/2}\right] \\ \lambda_2 &= \frac{1}{2}\left[k_2 + (k_2^2 - 4k_1)^{1/2}\right] \end{aligned} \tag{2.6}$$

$$\begin{aligned} G_1(z) &= \frac{1}{\lambda_2 - \lambda_1}\int_0^z g(z')exp(\lambda_1\,z')dz' \\ G_2(z) &= \frac{1}{\lambda_1 - \lambda_2}\int_0^z g(z')exp(\lambda_2\,z')dz' \end{aligned} \tag{2.7}$$

and

$$\begin{aligned} c_1 &= \frac{\lambda_2}{\lambda_2 - \lambda_1}x(0) \\ c_2 &= \frac{\lambda_1}{\lambda_1 - \lambda_2}x(0) \end{aligned} \tag{2.8}$$

2.1.2 Procedure B

In our second procedure, Eq. (2.4) is modified according to:

$$\begin{aligned} \frac{dx}{dz} &= v(z) + g(z) \\ \frac{dv}{dz} &= -k_1\, x(z) - k_2\, v(z) \end{aligned} \tag{2.9}$$

This is equivalent to

$$\ddot{x}(z) + k_2\dot{x}(z) + k_1 x(z) = k_2\, g(z) + \dot{g}(z) \tag{2.10}$$

in which $g(z)$ is the noise source of Eq. (2.2). Although Eq. (2.4) and Eq. (2.9) only differ in that $g(z)$ is displaced from the first to the second of the first-order equations, an additional first order fluctuation term, $\dot{g}(z)$ is present in Eq. (2.10). We will find that the $k_2\, g(z)$ generates relatively slow background fluctuations while $\dot{g}(z)$ is instead associated with rapid, small magnitude variations in $x(z)$.

As in procedure A, the analytic solution of Eq. (2.9) is determined by Eq. (2.5) in which $G_1(z)$ and $G_2(z)$ are redefined as

$$\begin{aligned} G_1(z) &= \frac{\lambda_2}{\lambda_2 - \lambda_1} \int_0^z g(z')exp(\lambda_1\, z')dz' \\ G_2(z) &= \frac{\lambda_1}{\lambda_1 - \lambda_2} \int_0^z g(z')exp(\lambda_2\, z')dz' \end{aligned} \tag{2.11}$$

The constants λ_1 and λ_2 are again obtained from Eq. (2.6).

As evident from the solution of Procedure B, i.e. Eq. (2.5) and Eq. (2.11), while the z-derivative $\dot{g}(z)$ appears formally in Eq. (2.10), this has no physical relevance since the solution for $x(z)$ only involves the term $g(z)$ which is the integral of the z-derivative $\dot{g}(z)$. However, the presence of the additional z-derivative does lead to a different physical behavior for $x(z)$ in procedures A and B.

2.1.3 Numerical Realization

To investigate PMD evolution in an optical fiber, we can model the fiber by a concatenation of N randomly-oriented sections with length Δz of polarization-maintaining (PM) fiber with fixed birefringence $x(n)$. The total fiber length is

denoted by $L = N\,\Delta z$. The quantities $x(n)$ form a random sequence with $n = 1, 2, 3, \cdots, N$ that we construct according to the prescriptions given in this section.

We first express the analytical solution of Eq. (2.5) of Procedure A as

$$\begin{aligned} x(n) &= \frac{exp(-\lambda_1 n\Delta z)}{\lambda_2 - \lambda_1}\left[\lambda_2\, x(0) + \int_0^{n\Delta z} g(z')exp(\lambda_1 z')dz'\right] \\ &+ \frac{exp(-\lambda_2 n\Delta z)}{\lambda_1 - \lambda_2}\left[\lambda_1\, x(0) + \int_0^{n\Delta z} g(z')exp(\lambda_2 z')dz'\right] \\ &= \frac{exp(-\lambda_1 n\Delta z)}{\lambda_2 - \lambda_1}[\lambda_2\, x(0) + \sum_{j=1}^{n} \tilde{g}_1(j)] \\ &+ \frac{exp(-\lambda_2 n\Delta z)}{\lambda_1 - \lambda_2}[\lambda_1\, x(0) + \sum_{j=1}^{n} \tilde{g}_2(j)] \end{aligned} \tag{2.12}$$

in which

$$\begin{aligned} \tilde{g}_1(j) &= \int_{(j-1)\Delta z}^{j\Delta z} g(z')exp(\lambda_1 z')dz' \\ \tilde{g}_2(j) &= \int_{(j-1)\Delta z}^{j\Delta z} g(z')exp(\lambda_2 z')dz' \end{aligned} \tag{2.13}$$

for $j = 1, 2, 3, \ldots, n$ and $n = 1, 2, 3, \ldots, N$.

From Eq. (2.2) and Eq. (2.13), we note that the mean square deviation of $\tilde{g}_i(j)$ must satisfy the following condition,

$$\begin{aligned} \langle \tilde{g}_i^2(j)\rangle &= \int_{(j-1)\Delta z}^{j\Delta z}\int_{(j-1)\Delta z}^{j\Delta z} \langle g(z')g(z'')\rangle e^{\lambda_i(z'+z'')}dz'dz'' \\ &= \int_{(j-1)\Delta z}^{j\Delta z}\int_{(j-1)\Delta z}^{j\Delta z} \sigma^2\delta(z'-z'')e^{\lambda_i(z'+z'')}dz'dz'' \\ &= \int_{(j-1)\Delta z}^{j\Delta z} \sigma^2 e^{2\lambda_i z'}dz' \\ &= \frac{\sigma^2}{2\lambda_i}\, e^{2\lambda_i(j-1)\Delta z}(e^{2\lambda_i\Delta z} - 1) \end{aligned} \tag{2.14}$$

for $i = 1, 2$. The quantity $\tilde{g}_i(j)$ in the j:th section is determined from

$$\tilde{g}_i(j) = \gamma(j)\triangle_i(j) \tag{2.15}$$

where $\gamma(j)$ is a random series with $-1 \leq \gamma \leq 1$ and $\triangle_i(j)$ is the maximum value of $\tilde{g}_i(j)$ in the j:th section, namely,

$$\triangle_i(j) = \sqrt{\frac{\sigma^2(e^{2\lambda_i \Delta z} - 1)}{2\lambda_i \langle \gamma^2 \rangle}}\, e^{\lambda_i (j-1)\Delta z}. \tag{2.16}$$

For Procedure A, we therefore obtain

$$\begin{aligned} x(n) &= \frac{exp(-\lambda_1 n \Delta z)}{\lambda_2 - \lambda_1}[\lambda_2\, x(0) + \sum_{j=1}^{n} \gamma(j) \triangle_1(j)] \\ &+ \frac{exp(-\lambda_2 n \Delta z)}{\lambda_1 - \lambda_2}[\lambda_1\, x(0) + \sum_{j=1}^{n} \gamma(j) \triangle_2(j)]. \end{aligned} \tag{2.17}$$

while the corresponding expression for $x(n)$ in Procedure B is given by

$$\begin{aligned} x(n) &= \frac{\lambda_2}{\lambda_2 - \lambda_1} exp(-\lambda_1 n \Delta z)[x(0) + \sum_{j=1}^{n} \gamma(j) \triangle_1(j)] \\ &+ \frac{\lambda_1}{\lambda_1 - \lambda_2} exp(-\lambda_2 n \Delta z)[x(0) + \sum_{j=1}^{n} \gamma(j) \triangle_2(j)] \end{aligned} \tag{2.18}$$

2.2 Modified Birefringence Models

We now describe methods for generating $b(z)$ and $\theta(z)$ in the context of our two procedures A and B above. In each case, two formalisms are examined. In the first of these, both $b(z)$ and $\theta(z)$ are obtained from the birefringence vector evaluated at the carrier frequency $\mathbf{b}(z) = \mathbf{b}(\omega_0, z)$, while the second generates $b(z)$ and $\theta(z)$ independently. This leads to four birefringence models which we label Model A1, Model B1, Model A2 and Model B2. We will also demonstrate that models A1 and B1 reproduce the RMM in an appropriate limit.

The random sequences $b(z)$ and $\theta(z)$ can be generated once a physical model for the birefringence is specified; and the frequency derivative $b'(z)$ is determined from $b(z)$ by

$$b'(z) = \frac{b(z)}{\omega_0}\,. \tag{2.19}$$

2.2.1 Model A1

In Model A1, once the two orthogonal components b_x and b_y of the birefringence vector $\mathbf{b}(z)$ are generated according to Procedure A from the parameters k_1, k_2 and the variance σ^2 of $\mathbf{g}(z)$, $b(z)$ and $\theta(z)$ are determined from

$$\begin{aligned} b(z) &= \sqrt{b_x^2(z) + b_y^2(z)} \\ \theta(z) &= \cos^{-1}(\frac{b_x}{b}) \end{aligned} \tag{2.20}$$

The variables k_1 and k_2 can be expressed in terms of the fiber parameters L_f and ϵ, c.f. Section (2.3) and Section (2.5), according to

$$\begin{aligned} k_1 &= \frac{1}{L_f^2}\frac{\epsilon}{1-\epsilon} \\ k_2 &= \frac{1}{L_f}\frac{1}{1-\epsilon}. \end{aligned} \tag{2.21}$$

where L_f and ϵ are defined as

$$\begin{aligned} L_f &= \frac{k_2 + \sqrt{k_2^2 - 4k_1}}{2k_1} \\ \epsilon &= \frac{k_2 + \sqrt{k_2^2 - 4k_1}}{2k_2}. \end{aligned} \tag{2.22}$$

Since $k_1 > 0$, $k_2 > 0$, Eq. (2.21) indicates that $0 < \epsilon < 1$. Also, Eq. (2.7) and Eq. (2.8) yield $\lambda_1 \neq \lambda_2$, or equivalently $\sqrt{k_2^2 - 4k_1} \neq 0$ according to Eq. (2.6), so that $\epsilon \neq 0.5$ from Eq. (2.22). We therefore examine the ranges $0 < \epsilon < 0.5$ and $0.5 < \epsilon < 1$ separately.

The quantity σ^2 can be determined by noting that

$$b_{rms} \equiv \lim_{z\to\infty}[\langle b^2(z)\rangle]^{1/2} = \frac{\pi}{\Lambda_{beat}}. \tag{2.23}$$

where the limit $\lim_{z\to\infty}\langle b^2(z)\rangle$ of the analytical solution Eq. (2.5) is

$$\lim_{z\to\infty}\langle b^2(z)\rangle = 2\sigma^2\,\lambda_{rms} \tag{2.24}$$

with

$$\lambda_{rms} = \frac{1}{(\lambda_2 - \lambda_1)^2}\left(\frac{1}{2\lambda_1} + \frac{1}{2\lambda_2} - \frac{2}{\lambda_1 + \lambda_2}\right) \tag{2.25}$$

From Eq. (2.23) and Eq. (2.24) we have

$$\sigma^2 = \frac{b_{rms}^2}{2\lambda_{rms}} \tag{2.26}$$

2.2.2 Model B1

In Model B1, the birefringence vector $\mathbf{b}(z)$ is instead obtained from Procedure B while $b(z)$ and $\theta(z)$ are determined as in Model A1 above. The three parameters, k_1, k_2 and σ^2 still fulfill Eq. (2.21) and Eq. (2.26) after identifying

$$\lambda_{rms} = \frac{1}{(\lambda_2 - \lambda_1)^2}\left(\frac{\lambda_2^2}{2\lambda_1} + \frac{\lambda_1^2}{2\lambda_2} - \frac{2\lambda_1\lambda_2}{\lambda_1 + \lambda_2}\right). \tag{2.27}$$

2.2.3 Model A2

In Model A2, the birefringence vector $\mathbf{b}(z)$ and associated birefringence strength $b(z)$ can again be generated from k_1, k_2 and σ_b^2 as in Model A1, while the values of $\theta(z)$ are determined as in the FMM [41]. Specifically, $\theta(z)$ is obtained from an independent random process according to

$$\frac{d\theta}{dz} = g_\theta(z) \tag{2.28}$$

in which $g_\theta(z)$ is a Gaussian white noise term satisfying

$$\langle g_\theta(z)\rangle = 0\,, \quad \langle g_\theta(z) g_\theta(z')\rangle = \sigma_\theta^2 \delta(z - z')\,. \tag{2.29}$$

The quantity σ_θ^2 can be determined according to

$$\begin{aligned}
\langle \cos[\theta(z) - \theta(0)]\rangle &= \left\langle \cos\left[\int_0^z dz' g_\theta(z')\right]\right\rangle \\
&= 1 - \left\langle \int_0^z dz' \int_0^{z'} dz'' g_\theta(z') g_\theta(z'')\right\rangle + \cdots \\
&= exp\left(-\frac{\sigma_\theta^2}{2} z\right) \\
&\equiv exp\left(-\frac{z}{L_\theta}\right).
\end{aligned} \tag{2.30}$$

where L_θ is the θ-correlation length. Eq. (2.30) then yields

$$\sigma_\theta^2 = \frac{2}{L_\theta}. \tag{2.31}$$

2.2.4 Model B2

In our final model, we assume as in Model A2, that the birefringence strength $b(z)$ and the principal axis angle $\theta(z)$ are independent. Further, we insure that θ follows the white noise process as in the FMM, and describe the longitudinal evolution of the birefringence strength, $b(z)$, with the Procedure B instead of Procedure A.

2.3 Birefringence Correlation Length

We next describe how the birefringence correlation length, which is a measurable quantity, can be determined from our model parameters. Considering first models A1 and B1, we observe that since both $b(z)$ and $\theta(z)$ are determined directly from $\mathbf{b}(z)$, the birefringence strength and principal axis angle have the same correlation length L_{corr}. The autocorrelation of the birefringence vector is calculated according to Eq. (2.5), which yields

$$\langle \mathbf{b}(0)\mathbf{b}(z)\rangle = b^2(0)\left[\frac{\lambda_2}{\lambda_2-\lambda_1}exp(-\lambda_1 z) - \frac{\lambda_1}{\lambda_2-\lambda_1}exp(-\lambda_2 z)\right] \tag{2.32}$$

where the variables λ_1 and λ_2 are defined through Eq. (2.6). However, since Eq. (2.21), which can be reexpressed as

$$\sqrt{k_2^2 - 4k_1} = \frac{1}{L_f}\frac{|1-2\epsilon|}{1-\epsilon} \tag{2.33}$$

has a different form for $\epsilon < 0.5$ and $\epsilon > 0.5$, we generate different expressions for λ_1 and λ_2 in the two ranges. From Eq. (2.6), Eq. (2.21) and Eq. (2.33), these are

$$\lambda_1 = \frac{1}{L_f}\frac{\epsilon}{1-\epsilon}, \quad \lambda_2 = \frac{1}{L_f}, \quad \text{for } 0 < \epsilon < 0.5 \tag{2.34}$$

and

$$\lambda_1 = \frac{1}{L_f}, \quad \lambda_2 = \frac{1}{L_f}\frac{\epsilon}{1-\epsilon}, \quad \text{for } 0.5 < \epsilon < 1. \tag{2.35}$$

Since the autocorrelation of the birefringence vector does not decrease exponentially with length according to Eq. (2.32), we define the correlation length L_{corr} by

$$\langle \mathbf{b}(0)\mathbf{b}(L_{corr})\rangle = b^2(0)exp(-1). \tag{2.36}$$

Eq. (2.32) and Eq. (2.36) then imply

$$\frac{\lambda_2}{\lambda_2-\lambda_1}\exp(-\lambda_1 L_{corr}) - \frac{\lambda_1}{\lambda_2-\lambda_1}\exp(-\lambda_2 L_{corr}) = \exp(-1). \tag{2.37}$$

If we introduce the relative correlation length $\nu \equiv L_{corr}/L_f$, we find from Eq. (2.34), Eq. (2.35) and Eq. (2.37)

$$(1-\epsilon)\exp(-\frac{\epsilon\nu}{1-\epsilon}) - \epsilon\exp(-\nu) = \exp(-1)(1-2\epsilon) \tag{2.38}$$

for both ranges of ϵ. Since ν can be expressed solely in terms of ϵ, the correlation length, $L_{corr} = \nu(\epsilon)L_f$, depends only upon ϵ and L_f. The results of a numerical calculation of ν for $0 < \epsilon < 1$, which are displayed with $\times$ markers in Fig. 2.1 along with a polynomial fit (solid line), further indicates that $\nu > 1$ in the entire physical range of ϵ, so that the correlation length L_{corr} always exceeds L_f.

While the general solution of Eq. (2.38) is complex, an analytical expression for ν can be derived if either $\epsilon << 1$ or $\epsilon \approx 1$. Note that $\lambda_1 \ll \lambda_2$ in these two cases since

$$\frac{\lambda_1}{\lambda_2} = \begin{cases} \frac{\epsilon}{1-\epsilon}, & \text{for } 0 < \epsilon < 0.5 \\ \frac{1-\epsilon}{\epsilon}, & \text{for } 0.5 < \epsilon < 1. \end{cases} \tag{2.39}$$

according to Eq. (2.34) and Eq. (2.35). Therefore, Eq. (2.32) can be approximated by

$$\langle \mathbf{b}(z)\mathbf{b}(0)\rangle = b^2(0)\, exp(-\lambda_1 z). \tag{2.40}$$

If we further assume $\langle \mathbf{b}(z)\mathbf{b}(0)\rangle = b^2(0)\, exp(-z/L_{corr})$ to be consistent with the definition of L_{corr} employed in Eq. (2.36), ν can be expressed analytically for small and large ϵ through Eq. (2.34), Eq. (2.35) and Eq. (2.40); namely,

$$\nu = \begin{cases} \frac{1-\epsilon}{\epsilon}, & \text{for small } \epsilon, \\ 1, & \text{for large } \epsilon. \end{cases} \tag{2.41}$$

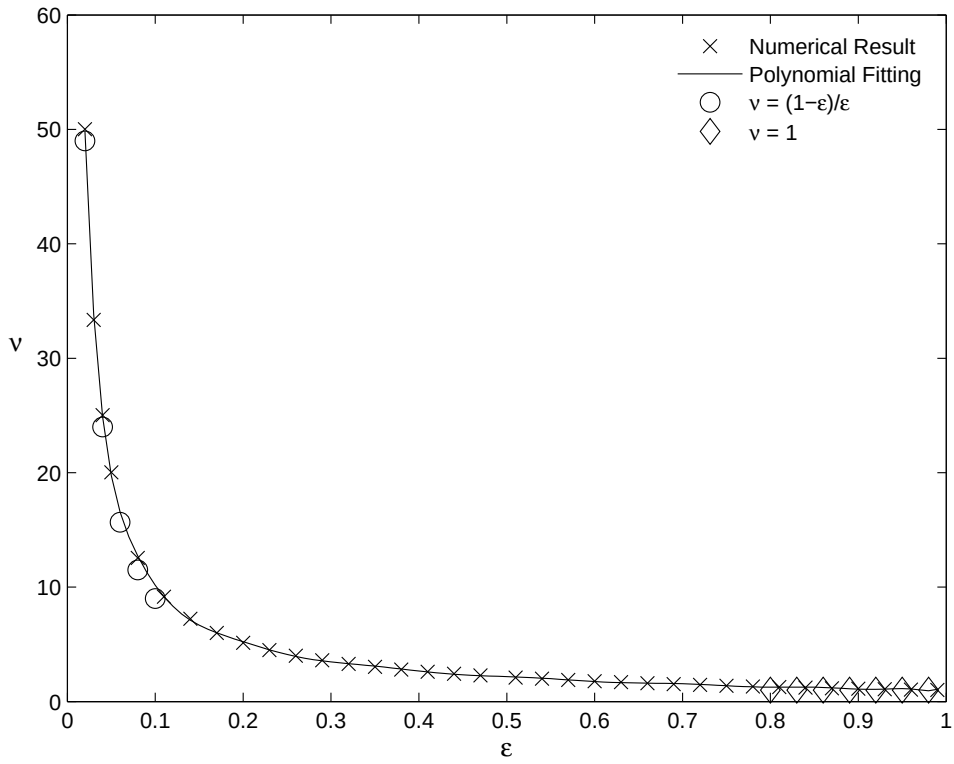

Figure 2.1: The relative correlation length ν as a function of ϵ for $0 < \epsilon < 1$. The numerical results are designated by $\times$ while the solid curve represents a polynomial fit to these values. The $\circ$ and $\diamond$ markers are calculated from our analytic formulas for the $\epsilon \approx 0$ and $\epsilon \approx 1$ regions, respectively.

The results of Eq. (2.41) for $0 < \epsilon < 0.1$ and $0.8 < \epsilon < 1$ are presented as the lines marked $\circ$ and $\diamond$ in Fig. 2.1. Evidently good agreement is achieved between the approximate and exact expressions in both regions.

In models A2 and B2 the fiber birefringence is instead defined through the four parameters Λ_{beat}, L_f, ϵ, and L_θ. Accordingly, two different correlation lengths $L_{corr,1} = \nu L_f$ and $L_{corr,2} \equiv L_\theta$ are associated with the birefringence strength $b(z)$ and the principal axis angle $\theta(z)$, respectively.

2.4 Limiting Behavior

In this section, we demonstrate that models A1 and B1 interpolate between the constant birefringence model and the RMM, while models A2 and B2 reproduce the FMM in a certain limit.

Considering first models A1 and B1 for $\epsilon \to 0$, $k_1 = 0$, $k_2 = 1/L_f$ from Eqs. (2.21), we find that Eqs. (2.6) and Eq. (2.25) imply $\lambda_{rms} \to \infty$ so that $\sigma^2 = 0$ from Eq. (2.26). Together with our assumption that $v(0) = 0$, Eqs. (2.4) and (2.9) then yield $\mathbf{b}(z) = \mathbf{b}(0)$, implying that the effective birefringence is constant while Eq. (2.41) indicates that $L_{corr} \to \infty$. For $\epsilon \to 1$, Eq. (2.41) instead reduces to $L_{corr} = L_f$. Accordingly, Eq. (2.3) and Eq. (2.10) yield

$$\frac{1}{k_2}\ddot{x}(z) + \dot{x}(z) + \frac{1}{L_{corr}}x(z) = \frac{1}{k_2}g(z) \tag{2.42}$$

and

$$\frac{1}{k_2}\ddot{x}(z) + \dot{x}(z) + \frac{1}{L_{corr}}x(z) = g(z) + \frac{1}{k_2}\dot{g}(z). \tag{2.43}$$

Further, since $k_1, k_2 >> 1$ when $\epsilon \to 1$ from Eq. (2.21), the first term $1/k_2\,\ddot{x}(z)$ in both Eq. (2.42) and Eq. (2.43) is far smaller than the remaining terms while $1/k_2\,\dot{g}(z)$ of Eq. (2.42) can be neglected in comparison to the first noise term $g(z)$. Consequently, both Eq. (2.42) and Eq. (2.43) yield the governing equation of the RMM [41], as will be verified numerically in the following section.

On the other hand, in models A2 and B2, when the parameters are chosen such that the birefringence strength remains nearly constant, the orientation of the birefringence vector still varies so that for $\epsilon \to 0$, the FMM is recovered.

2.5 Numerical Results

In this section, we investigate the longitudinal evolution and statistical properties of the random birefringence through numerical simulations.

We first demonstrate that ϵ is closely related to the magnitude of the stochastic birefringence fluctuations. In Fig. 2.2, we display numerically generated curves of

$b(z)$ and $\theta(z)$ for $z < 50\,m$ with $\Lambda_{beat} = 20\,m$ and $L_f = 12\,m$ for models A1 and B1. The random series of vectors $\mathbf{g}(z)$ have here been chosen identically for all calculations. The dashed, dotted, and solid lines correspond to $\epsilon = 0.01$, $\epsilon = 0.22$, and $\epsilon = 0.99$ respectively. As is evident from Fig. 2.2, the behavior of $b(z)$ and $\theta(z)$ varies markedly with ϵ. In particular, the fluctuations of $b(z)$ and $\theta(z)$ increase with ϵ and are respectively of the order of the birefringence strength or the principal axis angle in models A1 and B1 in the limit of $\epsilon \to 1$. The corresponding RMM results for $b(z)$ and $\theta(z)$ obtained by applying the RMM to the same sequence of noise vectors $\mathbf{g}(z)$ overlap with the solid curves of Model A1 or Model B1 for $\epsilon = 0.99$. Further, observe that the birefringence magnitude contains additional rapid and small fluctuations as a function of propagation length in Model B1 compared to Model A1, except when $\epsilon \approx 1$. This effect is especially pronounced for $\epsilon \approx 0$, as expected from the additional noise term $\dot{\mathbf{g}}$ in the B models. The birefringence maps generated by Model A2 or Model B2 are qualitatively similar to those of Model A1 or Model B1, respectively. We have further found that the birefringence magnitude is Rayleigh distributed in all four models, consistent with experimental results [54].

The above results have established that ϵ is roughly proportional to the magnitude of stochastical fluctuations in the fiber birefringence. While ϵ lies in the range $0 < \epsilon < 0.5$, our model more closely describes birefringence fibers with small birefringence fluctuations; while ϵ in the range $0.5 < \epsilon < 1.0$, our model applies to fibers with pronounced random birefringence variations, possibly originating in fluctuating physical environments.

To characterize the randomness of the birefringence, we calculate the probability density function (pdf) of the birefringence strength b based on our four general models by varying both fiber length and ϵ. We find that, for any value of $0 < \epsilon < 1$, this pdf of b approaches the Rayleigh distribution with increasing fiber length. However, the pdf approaches the Rayleigh distribution more rapidly for larger ϵ. Moreover, for a finite fiber length, while the pdf deviates from the Rayleigh distribution as ϵ decreases, this deviation is not significant for $0.20 < \epsilon < 1$. To illustrate this, we plot in Fig. 2.3 the pdf of the birefringence strength b of fiber length $z = 3\,km$ for (a) $\epsilon = 0.99$, (b) $\epsilon = 0.60$, (c) $\epsilon = 0.20$ and (d) $\epsilon = 0.01$. The birefringence strengths are generated for a fixed set of random values,

$\mathbf{g}(z)$, based on Model B1 with $\Lambda_{beat} = 10\,m$, $L_f = 15\,m$. The solid curves are the corresponding best fitting Rayleigh pdfs. Our numerical simulation indicates that our general models are consistent with experimental histogram for the fiber birefringence strength c.f. 1.5.

2.6 Conclusions

We have introduced four birefringence models that simulate the evolution of birefringence along an optical fiber by adding a restoring force to the Langevin equation. Unlike the standard Langevin equation, the birefringence is described by the modified equations as a random variable with a non-zero mean value but effectively arbitrary fluctuation amplitude. Consequently, the method can be fit to a broad range of observed fiber birefringence behavior that can result from different intrinsic properties and/or external physical environments. Further, we have demonstrated that the fixed and random modulus model can be recovered as limiting cases of the formalism, which however can model fibers with any relationship between the mean birefringence vector magnitude and the mean amplitude of fluctuations in both the magnitude and the direction of the birefringence. Since birefringence properties may differ not only among optical fibers but also may change for a single fiber depending on the external environment, such models, which allow the birefringence correlation lengths and the extent of the perturbation fluctuation to be adjusted separately, could be required for the accurate predictions of certain statistical properties.

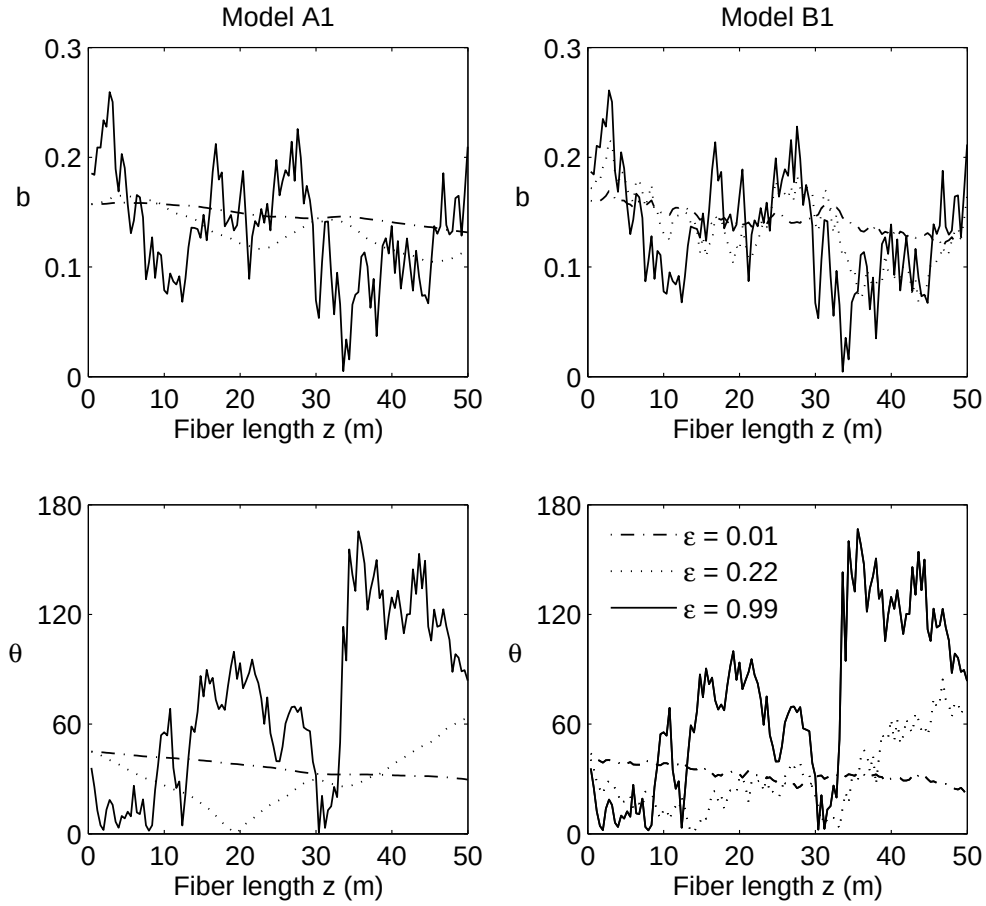

Figure 2.2: The variation of the birefringence strength b and axis rotation angle θ with fiber propagation distance $z < 50$ for a fixed set of random values, $\mathbf{g}(z)$ with $\Lambda_{beat} = 20\,m$ and $L_f = 12\,m$. The dashed, dotted and solid curves are generated with $\epsilon = 0.01, 0.22, 0.99$ in model A1 and B1. The RMM method results overlap with those of model A1 and B1 for $\epsilon = 0.99$.

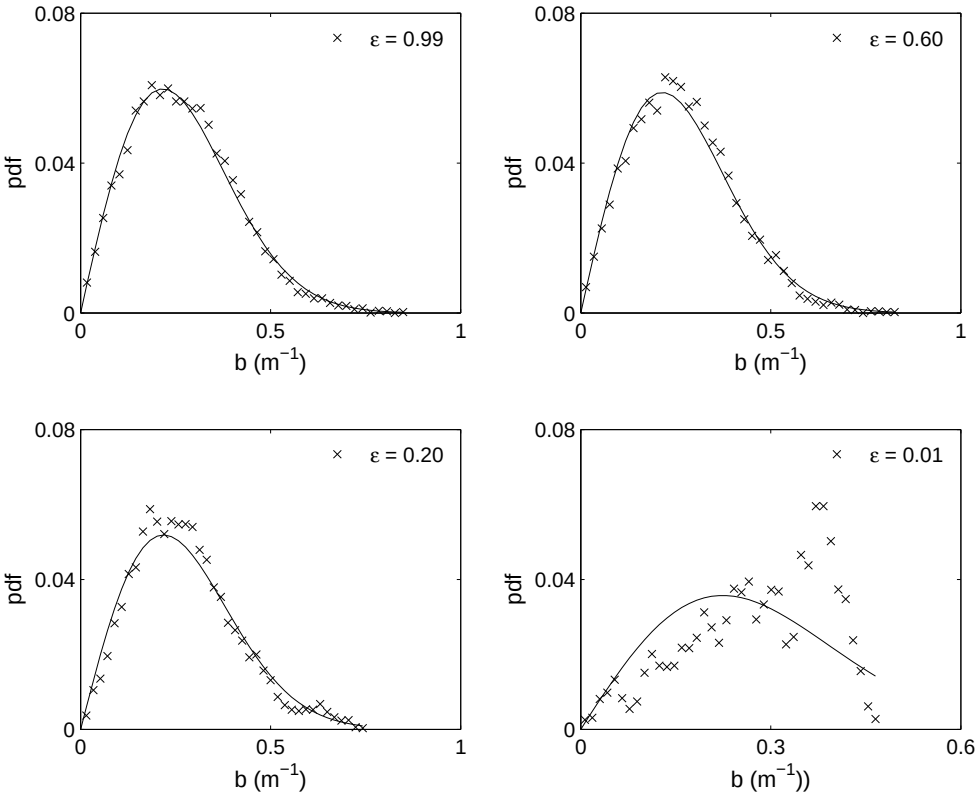

Figure 2.3: The probability density function (pdf) of the birefringence strength b of fiber length $z = 3\,km$ for (a) $\epsilon = 0.99$, (b) $\epsilon = 0.60$, (c) $\epsilon = 0.20$ and (d) $\epsilon = 0.01$. The birefringence strengths are generated for a fixed set of random values, $\mathbf{g}(z)$, based on Model B1 with $\Lambda_{beat} = 10\,m$, $L_f = 15\,m$. The solid curves are the corresponding best fitting Rayleigh pdfs

Chapter 3

Application of Various Birefringence Models to Polarization Mode Dispersion

Since polarization mode dispersion (PMD) originates from fiber birefringence fluctuations in both the magnitude and orientation along the length of an optical fiber or waveguide [43], a complete description of PMD requires knowledge of the detailed statistical structure of the fiber birefringence map. To examine the statistical properties of the PMD, three simple models, i.e., the Foschini-Poole model, the FMM and RMM have been employed in statistical studies of the PMD for standard [61] and spun [62, 63] fibers. While the probability distribution functions (pdf) of the DGD for all models share the same Maxwell distribution for long fiber lengths, the statistical features of the PMD of short fibers and of the DGD of periodically spun fibers differ substantially. Since birefringence profiles not only differ among fibers, but also change with time within a single fiber as a result of environmental fluctuations, installed fibers have more birefringence fluctuations than spooled fibers. For the stochastic characterization of a broad range of birefringence profiles, we have introduced in Chapter 2 four additional physical fiber birefringence models, designated Model A1, Model B1, Model A2 and Model B2. Of these, models A1 and B1 interpolate between the constant birefringence model and the RMM, while

models A2 and B2 extend the FMM. While most previous studies have focused upon the long fiber length regions, in this chapter we will examine the stochastic properties of the PMD of random birefringence fibers at all length scales based on the FMM and RMM, and our improved models.

3.1 Transfer Matrix

Our evaluation of the DGD employs the transfer matrix formalism [11] in which the fiber is modeled by N sections of polarization maintaining (PM) fiber. The transfer matrix of the fiber then takes the form

$$\mathbf{M}(\omega) = \prod_{n=0}^{N} \mathbf{M}_n(\omega) \ . \tag{3.1}$$

$\mathbf{M}_n(\omega)$ represents the solution of the ordinary differential equation for the two orthogonal polarization components of the electric field in each PM section n, namely [40] ,

$$\mathbf{M}_n(\omega) = \begin{pmatrix} m_{11} & m_{12} \\ m_{21} & m_{22} \end{pmatrix} \tag{3.2}$$

with

$$\begin{aligned} m_{11} &= m_{22}^* \\ &= \cos[(b(n) + b'(n)\omega)\Delta z] + i\cos(\theta(n))\sin[(b(n) + b'(n)\omega)\Delta z] \\ m_{12} &= m_{21} \\ &= i\sin(\theta(n))\sin[(b(n) + b'(n)\omega)\Delta z] \ . \end{aligned}$$

where $b(n)$, $b'(n)$ and $\theta(n)$ are calculated according to the corresponding birefringence models.

3.2 Polarization Mode Dispersion Based on Wai-Menyuk Models

Although experimental measurements of statistical properties of the random birefringence appear consistent with the Random Modulus Model (RMM) [54], most theoretical studies have instead actually employed the Foschini-Poole model and the FMM [39, 61, 64] due to their relative simplicity. In this section, we employ both the RMM and FMM to compute the evolution of DGD for fiber lengths less than or of the order of the birefringence correlation length.

3.2.1 Numerical Realizations

For the following numerical realizations, a linearly birefringent single mode fiber is approximated as N sections of a polarization maintained (PM) fiber with section size Δz, i.e. $L = N \cdot \Delta z$, and birefringence vector $\mathbf{b} = [b\cos\theta,\, b\sin\theta]^t$, which implies a birefringence strength $b(\omega, n) = b(\omega, n\Delta z)$, group delay per unit length $b'(\omega, n) = b'(\omega, n\Delta z)$, and birefringence angle $\theta(n)$. In this subsection, we introduce mathematical algorithms for generating $b(n)$ and $\theta(n)$ based on the FMM and RMM.

Fixed Modulus Model

In the FMM, the birefringence strength is assumed to be a constant, i.e., $b(n) = b$. In the following, we introduce the procedure to generate the randomly varying birefringence angle $\theta(n)$.

According the definition of $g_\theta(z)$, c.f. Eq. (1.37), the rotation angle between the birefringence axes of adjacent PM fiber sections can be expressed in the form

$$\Delta\theta(j) = \int_{(j-1)\Delta z}^{j\Delta z} g_\theta(z)\, dz$$

for j=1, 2, 3, $\cdots$, n. The mean square value of the angular displacement is therefore

given by

$$\begin{aligned}\langle \Delta\theta^2(j) \rangle &= \int_{(j-1)\Delta z}^{j\Delta z} dz' \int_{(j-1)\Delta z}^{j\Delta z} dz'' \, \langle \, g_\theta(z') g_\theta(z'') \, \rangle \\ &= \int_{(j-1)\Delta z}^{j\Delta z} dz' \int_{(j-1)\Delta z}^{j\Delta z} dz'' \, \sigma_\theta^2 \, \delta(z'' - z') \\ &= \frac{2\Delta z}{L_{corr}} \, . \end{aligned} \tag{3.3}$$

In our simulations, we generate the random variable $\Delta\theta(j)$ for each section j according to

$$\Delta\theta(j) = \gamma(j) \cdot \Delta\theta_{max} \tag{3.4}$$

where γ is a random number in the range of $(-1, 1)$. The maximum rotation between sections is then

$$\Delta\theta_{max} = \left(\frac{\Delta z}{2 L_{corr} \langle \gamma^2 \rangle} \right)^{1/2} , \tag{3.5}$$

and the birefringence axis angle $\theta(n)$ for the n:th section relative to the input axis is

$$\theta(n) = \sum_{j=1}^{n} \gamma(j) \, \Delta\theta_{max} \, . \tag{3.6}$$

Random Modulus Model

In the RMM, we generate the random vector $\mathbf{b}(n)$ in the following manner. First, we rearrange Eq. (1.41) so that it does not contain the continuous vector $\mathbf{g}(z)$ as follows

$$\begin{aligned}\mathbf{b}(n) &= [\mathbf{b}(0) + \int_0^{n\Delta z} \mathbf{g}(z') \, exp(az') \, dz'] \, exp(-an\Delta z) \\ &= [\mathbf{b}(0) + \sum_{j=1}^{n} \int_{(j-1)\Delta z}^{j\Delta z} \mathbf{g}(z') \, exp(az') \, dz' \,] \, exp(-an\Delta z) \\ &= [\mathbf{b}(0) + \sum_{j=1}^{n} \mathbf{G}(j) \,] \, exp(-an\Delta z) \end{aligned} \tag{3.7}$$

where

$$\mathbf{G}(j) = \int_{(j-1)\Delta z}^{j\Delta z} \mathbf{g}(z')\, exp(az')\, dz' \,, \tag{3.8}$$

for j=1, 2, 3, $\cdots$, n and n=1, 2, 3, $\cdots$, N.
Further, Eq. (1.40) and Eq. (3.8) require that the mean square of $\mathbf{G}(j)$ satisfy the condition,

$$\begin{aligned} \langle G^2(j)\rangle &= \int_{(j-1)\Delta z}^{j\Delta z}\int_{(j-1)\Delta z}^{j\Delta z} \langle \mathbf{g}(z')\mathbf{g}(z'')\rangle\, exp(az'+az'')dz'dz'' \\ &= \frac{\sigma^2}{2a}\, exp[2a(j-1)\Delta z]\,[exp(2a\Delta z)-1] \,. \end{aligned} \tag{3.9}$$

Similar to what is done in FMM, we generate $\mathbf{G}(j)$ for the j:th section as,

$$\mathbf{G}(j) = \vec{\gamma}(j)\, \triangle_{max}(j) \,. \tag{3.10}$$

Here $\vec{\gamma}$ is now a random vector with $-1 < |\vec{\gamma}| < 1$, while $\triangle_{max}(j)$ is the maximum value for $\mathbf{G}(j)$ in the j:th section. Since the mean square value of $\mathbf{G}(j)$, Eq. (3.9), is different in each PM fiber section j, we employ $\triangle_{max}(j) = \triangle_c\, exp[a(j-1)\Delta z]$, where $\triangle_c$ is a constant. Note that the value of $\triangle_{max}(j)$ is different in each section in RMM but remains constant in the FMM. Combining Eq. (3.9) and Eq. (3.10), now yields

$$\triangle_{max}(j) = \left[b_{rms}^2 \frac{exp(2a\Delta z)-1}{2\langle\gamma^2\rangle} \right]^{1/2} exp[a(j-1)\Delta z] \tag{3.11}$$

so that

$$\mathbf{b}(n) = [\,\mathbf{b}(0) + \sum_{j=1}^{n} \vec{\gamma}(j)\triangle_{max}(j)\,]\; exp(-an\Delta z) \,. \tag{3.12}$$

3.2.2 Numerical Results

We first calculate the DGD and its probability density function (pdf) for the FMM and RMM. We then study the relative deviation,

$$\delta_{rms} = \frac{\tau_{rms} - \tau_{rms}^*}{\tau_{rms}^*}, \tag{3.13}$$

of the root-mean-squared DGD from its analytical value

$$\tau^*_{rms} = 2b' \left[2zL_{corr} + 2L^2_{corr}\, exp(-z/L_{corr}) - 2L^2_{corr}\right]^{1/2}, \tag{3.14}$$

as well as the deviation of the mean DGD from its asymptotic value for large z, namely

$$\delta_{mean} = \frac{\langle\tau\rangle - \langle\tau\rangle_{asym}}{\langle\tau\rangle_{asym}}, \tag{3.15}$$

where $\langle\tau\rangle_{asym} = [8/(3\pi)]^{1/2}\,\tau_{rms}$. Our calculations are performed for fiber lengths ranging from zero to several fiber correlation lengths, with birefringence parameters $\Lambda_{beat} = 10\,m$, $L_{corr} = 15\,m$, and $D_{pmd} = 0.2\,ps/(km)^{1/2}$. The fiber length z is normalized as $L = z/L_{corr}$.

In Fig. 3.1 we display the results for the FMM of our Monte Carlo simulations after 10^6 fiber realizations for the pdf of DGD for fiber lengths $L = 0.01$, 1, 5, 10, 20, and 100. In subplots (e) and (f), the Maxwell distribution is also plotted for comparison. In all our graphs, the Maxwell distributions are given by the mean DGD determined by the the Monte-Carlo simulations. We observe that for $L < 1$, indicating that the fiber length is shorter than the correlation length, the pdf is highly peaked with a long tail in the low DGD side and zero probability density for DGD close to zero. For larger fiber lengths, the pdf gradually develops an extended tail for large DGD, c.f. subplot (d), and increasingly approximates a Maxwell distribution as in the last subplot. The pdf of DGD for the RMM differs markedly from that of the FMM, as shown in Fig. 3.2. In this case the pdf is initially nearly symmetric at very short propagation distances. While the pdf approaches a Maxwell distribution as L increases from 0.0 to 0.825, it again distorts in the direction of low DGD as L increases further. The distortion reaches a maximum at $L \simeq 2.5$. but subsequently approaches the Maxwell distribution asymptotically. The two distributions nearly coincide for $L > 100$. For longer fiber lengths, the evolution of the tail of the pdf at large DGD, which gives rise to the physically important system outage events is shown in Fig. 3.3. Here the dotted curves are the base 10 logarithmic plot of the pdf ρ computed with the Monte-Carlo method for L=20, 100 and 1000, based on (a) the FMM and (b) the RMM , while the solid curves are the corresponding Maxwell distributions. While as expected, both

methods yield the Maxwell distribution asymptotically, this curve is approached from above for the RMM and below for the FMM.

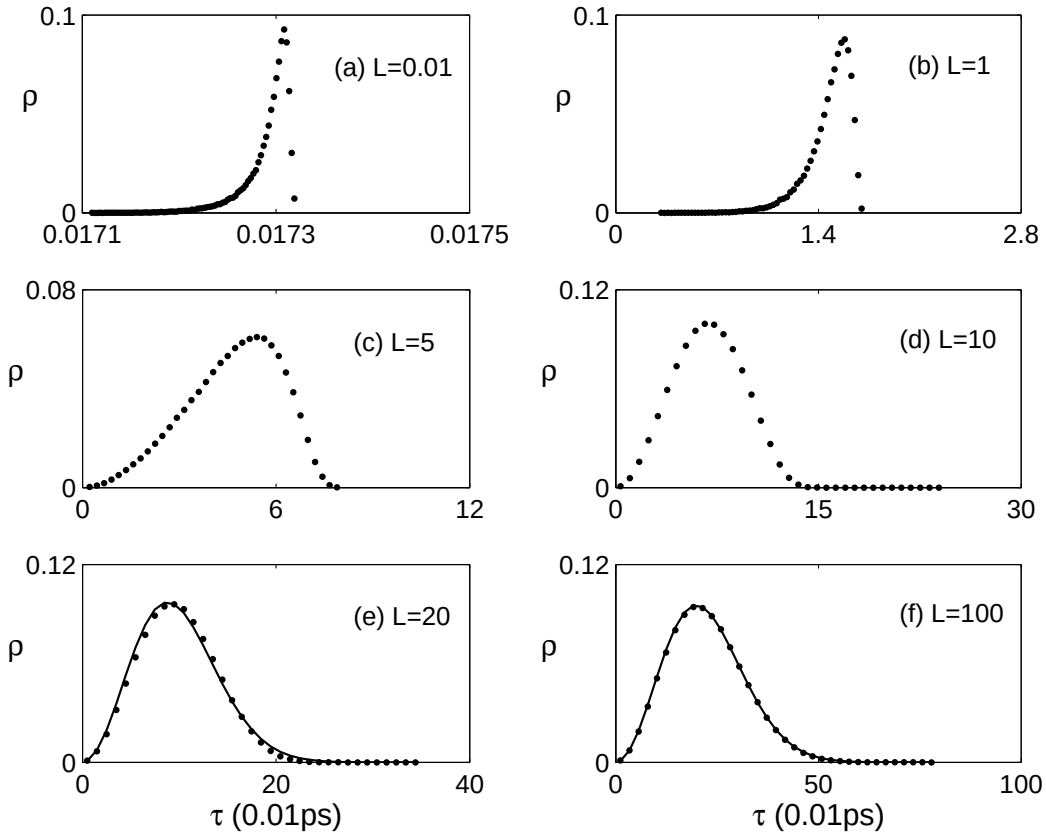

Figure 3.1: The probability density ρ as a function of the DGD, τ. The dotted curves are the results of Monte-Carlo simulations based on the FMM for L equal to (a) 0.01, (b) 1, (c) 5, (d) 10, (e) 20, (f) 100, while the solid lines in (e) and (f) are Maxwell distributions.

In Fig. 3.4 (a) and (b) we display the relative deviations δ_{rms} and δ_{mean} as functions of $log(L)$ for the FMM and RMM, respectively, computed for 12 different fiber lengths from L=0.03 to L=100. The values for δ_{rms}, which are represented by the symbol $\circ$ in the figures, nearly vanish (zero is indicated by the dashed-dotted line) in both models, which implies that our calculated results for the rms DGD

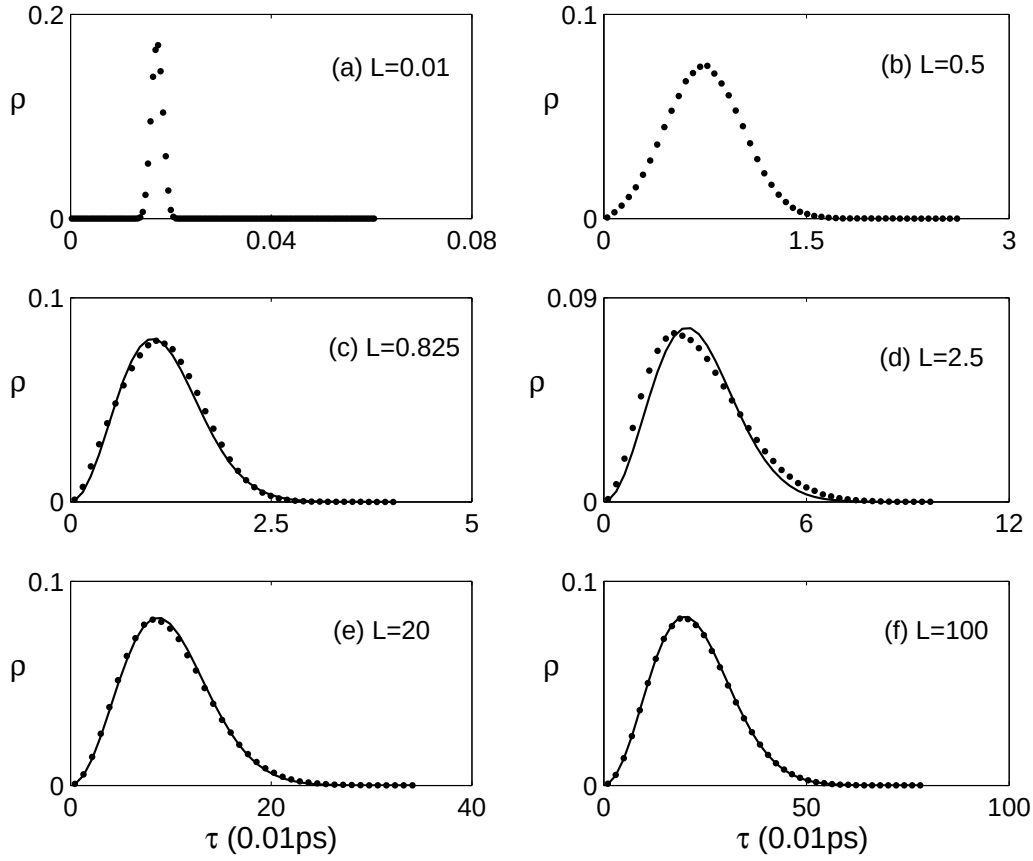

Figure 3.2: The probability density ρ as a function of the DGD, τ. The dotted curves are the results of Monte-Carlo simulations based on the RMM for L equal to (a) 0.01, (b) 0.5, (c) 0.825, (d) 2.5, (e) 20, (f) 100, while the solid lines in (c) - (f) are the Maxwell distributions.

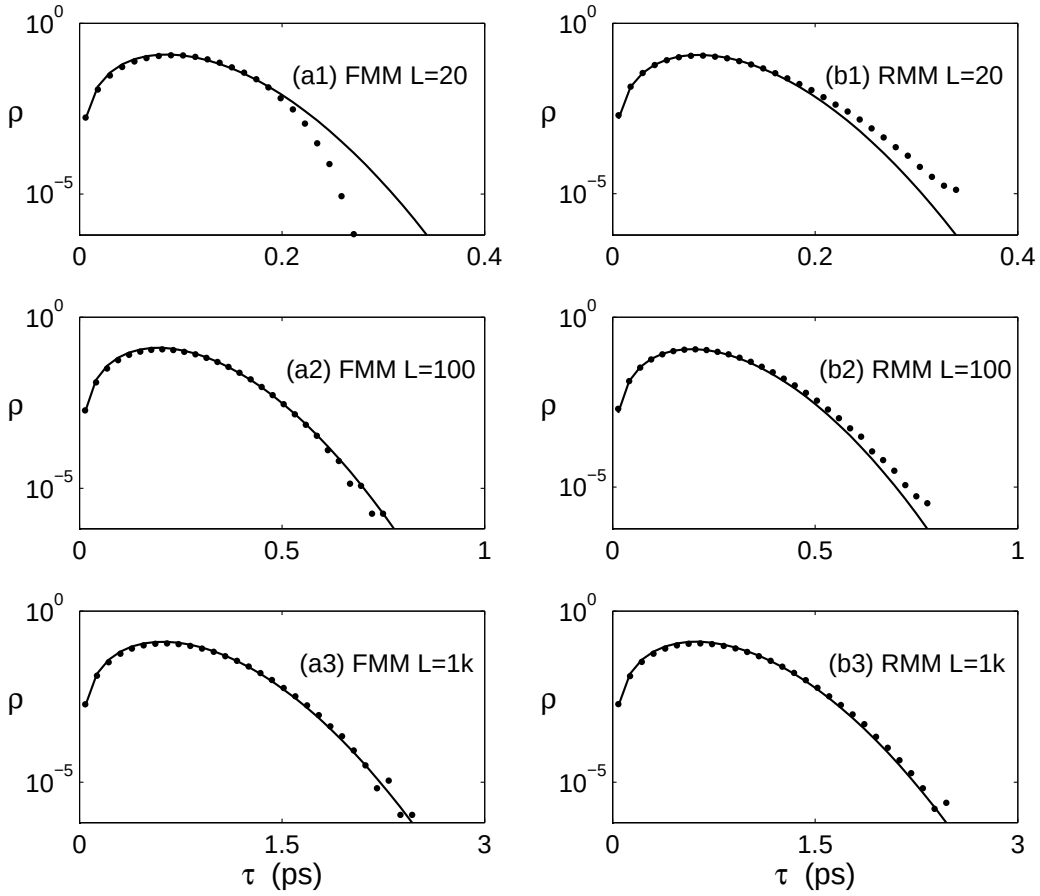

Figure 3.3: The variation of the pdf ρ with the DGD τ in a logarithmic (base 10) scale, for L=20, 100, and 1000 based on (a) the FMM and (b) the RMM. The dotted curves are the Monte Carlo simulation results while the solid curves display the Maxwell distributions.

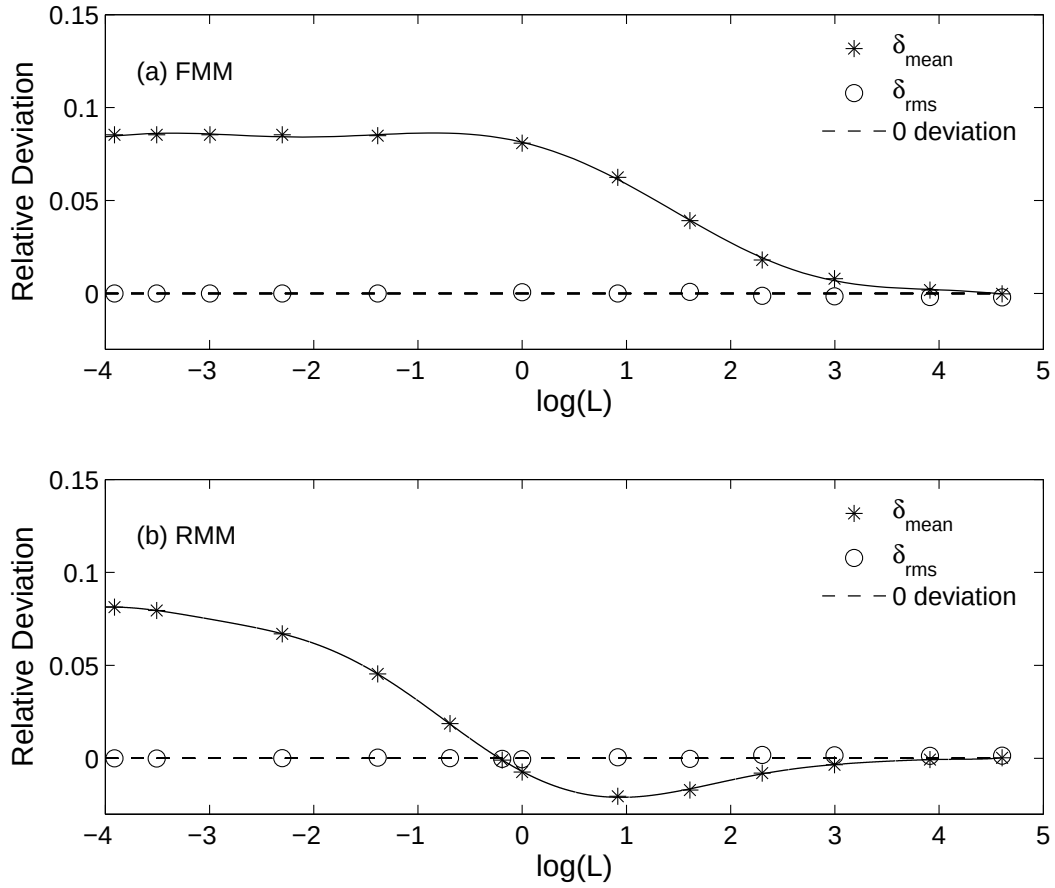

Figure 3.4: The relative deviations δ_{mean} and δ_{rms} plotted as functions of $log(L)$ for (a) the FMM and (b) the RMM. The symbol $*$ corresponds to the δ_{mean} while the symbol $\circ$ represents the δ_{rms}. The dashed-dotted lines indicate zero deviation. The solid curves are polynomial fits to the δ_{mean} data.

nearly coincide with the analytic predictions, Eq. (3.14). While for large L, δ_{mean} for both models approaches zero, however, this occurs monotonically in the FMM, while in the RMM, δ_{mean} first decreases from positive to negative values before subsequently rising to zero. A polynomial fit yields $L = 0.825$ for the zero point location. The accuracy of our results was further established by repeating our calculation for different values of Δz.

3.3 Polarization Mode Dispersion Based on Improved Models

In the previous section, we have examined the statistical properties of the PMD based on the FMM and RMM. In this section, we investigate the stochastic properties of PMD based on our four improved models. In the following, we first review the four models, with emphasis on the physical implications of the defining equations and their applicability to different fiber birefringence maps. We then derive relationships between the root mean square DGD and the statistical parameters of the birefringence variations. The corresponding results of numerical PMD simulations are presented in the final subsection.

3.3.1 Model Descriptions

To motivate our subsequent numerical studies, we first briefly review the models of fiber birefringence presented in section 2.2. In this context, we derive analytic formulas for the root mean square DGD for certain of these models.

To calculate the statistical variation of $b(z)$ and $\theta(z)$ with z requires an appropriate birefringence model. In two of our models, labeled A1 and B1, $b(z)$ and $\theta(z)$ are obtained from the orthogonal components b_x and b_y of $\mathbf{b}(\omega_0, z)$ according to Eq. (2.20).

In the FMM, $\theta(z)$ follows a Wiener process, while in the RMM, $b_x(z)$ and $b_y(z)$ obey two independent Langevin equations. In both cases, a random birefringent variable $x(z)$ with zero mean results [41], where $x(z)$ denotes either of the two

birefringence components $b_x(z)$ and $b_y(z)$. While this behavior is expected in birefringent fibers subject to random perturbations, the birefringence in polarization maintaining fibers or fibers subject to systematic stresses fluctuate around a non-zero mean value. For this case, we introduced the modified Langevin equation, Eq. (2.3) for Model A1, and Eq. (2.10) for Model B1, respectively. Here $k_1, k_2 > 0$, and $g(z)$ represents a Gaussian "white noise". While only a single term $g(z)$ appears in Eq. (2.3), an additional first order term, $\dot{g}(z)$, is included in Eq. (2.10). As discussed in Chapter 2, $g(z)$ in Eq. (2.3), or $k_2 g(z)$ in Eq. (2.10), leads to far slower and larger-amplitude fluctuations in the birefringence $x(z)$, than does the extra term $\dot{g(z)}$ in Eq. (2.10).

Since the asymptotic behavior of $x(z)$ is independent of the initial condition, we set $v(0) = 0$ in Eq. (2.3) which yields the analytical solution Eq. (2.5)- Eq. (2.8). The analytical solution of Eq. (2.10) is also given by Eq. (2.5) with $G_1(z)$ and $G_2(z)$ now defined by Eq. (2.11).

Despite the similar forms of the analytical solutions to models A1 and B1, the latter formalism predicts a relatively slowly varying birefringence as a function of fiber length while the former yields additional high-frequency but small magnitude fluctuations, c.f. Fig 2.2. Additional distinguishing features of the two models will be discussed in section 3.3.2.

To relate the three parameters appearing in Eqs. (2.3) and (2.10), i.e., k_1, k_2, and σ^2, to physically meaningful quantities, we first observe that σ^2 is defined as the variance of Eq. (2.2) and is consequently related to the beat length Λ_{beat} through

$$\sigma^2 = \frac{\pi^2}{2\lambda_{rms}\Lambda_{beat}^2}, \tag{3.16}$$

where λ_{rms} is calculated according to Eq. (2.25) for Model A1 and Eq. (2.27) for Model B1. The quantities λ_1 and λ_2 are given in terms of k_1 and k_2 by Eq. (2.6). We can further relate k_1 and k_2 to two physical parameters, the random fluctuation strength parameter ϵ and the correlation length L_{corr}. For mathematical convenience, we introduce the inverse coupling strength $L_f = L_{corr}/\nu$ where ν is expressed in terms of ϵ by Eq. (2.38). We can relate k_1 and k_2 to ϵ and L_f, or equivalently ϵ and L_{corr}. Solving Eq. (2.38) numerically then demonstrates that

L_{corr} increases from L_f to ∞, as ϵ decreases from 1 to 0. Note that ϵ $(0 < \epsilon < 1)$ corresponds to the mean fluctuation amplitude of the fiber birefringence, while L_f equals the shortest fiber correlation length L_{corr} when $\epsilon \to 1$. In terms of these parameters, k_1 and k_2 can be rewritten as in Eq. (2.21). Models A1 and B1 interpolate between a constant-birefringence model when $\epsilon \to 0$ and the random modulus model (RMM) for $\epsilon \to 1$. Consequently, depending on the values of ϵ and L_f, models A1 and B1 describe a broad range of fiber birefringence profiles.

Because models A1 and B1 generate both $b(z)$ and $\theta(z)$ from the same random process, the fluctuations in both the birefringence strength and orientation are of the same order. This behavior appears reasonable for fibers with small intrinsic birefringence, for which both the birefringence strength and orientation should typically be affected in the same manner by small perturbations. However, for fibers with relatively large intrinsic birefringence, small perturbations could affect the birefringence strength less than the birefringence orientation. Therefore, we proposed two additional models, A2 and B2, in which $b(z)$ and $\theta(z)$ are influenced by independent random processes. In these procedures, which again employ the three parameters ϵ, L_f and Λ_{beat}, $b(z)$ is calculated in the same manner as models A1 and B1, but $\theta(z)$ is governed by an independent equation, i.e., Eq. (2.28). In Eq. (2.28), $g_\theta(z)$ is an uncorrelated noise term with variance $\sigma_\theta^2 = 2/L_\theta$ where L_θ is the correlation length of θ. While the FMM is again recovered in the limit of $\epsilon \to 0$, models A2 and B2 extend the FMM to a broad range of birefringence profiles. For example, to limit the excursion of $b(z)$ while ensuring that $\theta(z)$ exhibits large amplitude variations, ϵ should be set to a small value, typically $0 < \epsilon < 0.5$.

Since the random variations of the PMD originate from birefringence fluctuations, we can compute its statistical properties from our models. For long fibers, the most significant of these is the mean DGD since the probability density distribution of the DGD is known to be Maxwellian in this limit. Therefore, the root mean square DGD is a key quantity that we will now examine for the representative case of Model B1. While the same analysis applies to Model A1, models A2 and B2 of course lead to more complex formulas, as they predict different correlation lengths for $b(z)$ and $\theta(z)$.

Accordingly, we first consider the defining equation,

$$\frac{\partial \boldsymbol{\tau}(z,\omega)}{\partial z} = \frac{\partial W(z,\omega)}{\partial z} + W(z,\omega) \times \boldsymbol{\tau}(z,\omega) \tag{3.17}$$

in which $\boldsymbol{\tau} = [\tau_1, \tau_2, \tau_3]^t$ denotes the PMD vector, and $W = [2b_x, 2b_y, 0]^t$ with b_x and b_y the two components of the birefringence vector $\mathbf{b}$. The frame of reference is rotated by $\tilde{\boldsymbol{\tau}} = R(z)\boldsymbol{\tau}$ with

$$R(z) = \begin{pmatrix} \cos\theta(z) & \sin\theta(z) & 0 \\ -\sin\theta(z) & \cos\theta(z) & 0 \\ 0 & 0 & 1 \end{pmatrix}$$

such that the birefringence vector is in the τ_1 direction. Since the DGD, τ, which equals the magnitude of the PMD vector, is invariant under rotations, we have

$$\langle \tau^2 \rangle = \langle \tilde{\tau_1}^2 + \tilde{\tau_2}^2 + \tilde{\tau_3}^2 \rangle \tag{3.18}$$

where $\langle \tilde{\tau_1}^2 + \tilde{\tau_2}^2 + \tilde{\tau_3}^2 \rangle$ is determined by Eq. (3.17) in the rotated frame together with Eq. (2.10).

We further assume that $b(\omega, z) = \rho(\omega)b(z)$ in which $b(z) = b(\omega_0, z)$ is the birefringence strength at the carrier frequency and $\rho(\omega)$ is a deterministic function of frequency. Following the procedure of [41], we arrive at

$$\begin{aligned} \frac{\partial \langle \tau^2 \rangle}{\partial z} &= 4\rho_\omega \langle b\tilde{\tau}_1 \rangle \\ \frac{\partial \langle b\tilde{\tau}_1 \rangle}{\partial z} &= 2\rho_\omega \langle b^2 \rangle + \langle \frac{b_x v_x + b_y v_y}{\rho b}\, \tilde{\tau}_1 \rangle + \langle \frac{b_x v_y - b_y v_x}{\rho b}\, \tilde{\tau}_2 \rangle \end{aligned} \tag{3.19}$$

Here we have denoted the frequency derivative of ρ by ρ_ω. The root mean square DGD is defined as $\tau_{rms} \equiv \sqrt{\langle \tau^2 \rangle}$.

Since the general solution of Eq. (3.19) is complex, we first consider two special cases. For $\epsilon \to 0$, which corresponds to an optical fiber with a constant birefringence, Eq. (2.10) yields $v_x(z) = 0$ and $v_y(z) = 0$ for the initial condition $\mathbf{v}(0) = 0$. Eq. (3.19) then yields the root mean square DGD of a polarization-maintaining fiber, namely, τ_{rms}^{PM},

$$\tau_{rms}^{PM} = \frac{2\pi}{\omega \Lambda_{beat}} z. \tag{3.20}$$

In $\epsilon \rightarrow 1$ limit, Model B1 reproduces the RMM. Comparing Eq. (2.10) to the Langevin equation for the RMM [41] gives

$$v_x = -b_x/L_f,\ v_y = -b_y/L_f. \tag{3.21}$$

The corresponding expression for the root mean square DGD,

$$\tau_{rms}^{RMM} = \frac{2\pi}{\omega\Lambda_{beat}}\,[2zL_f + 2L_f^2\,exp(-z/L_f) - 2L_f^2]^{1/2}, \tag{3.22}$$

then follows from Eq. (3.19) and Eq. (3.21).

In general, as ϵ increases from 0 to 1, the stochastic fluctuation amplitude increases monotonically, resulting in a stronger coupling between the two polarization modes and hence a smaller PMD. That is, in general $\tau_{rms}^{RMM} < \tau_{rms} < \tau_{rms}^{PM}$. Note that if L_f is replaced by L_{corr}, Eq. (3.22) yields the formula,

$$\tau_{rms}^{*} = 2\frac{\pi}{\omega_0\Lambda_{beat}}\,[2zL_{corr} + 2L_{corr}^2\,exp(-z/L_{corr}) - 2L_{corr}^2]^{1/2}\,, \tag{3.23}$$

for the root mean square DGD of the FMM and RMM. Since $L_{corr} = \nu(\epsilon)L_f$ where $0 < \epsilon < 1$, τ_{rms}^{*} in Eq. (3.23) depends on the three parameters, ϵ, L_f and Λ_{beat} of Model B1.

While Eq. (3.23) transforms into Eq. (3.20) and Eq. (3.22) in the two limiting cases discussed above, in general it predicts different mean DGD values than Model A1 and B1, as we demonstrate explicitly in the subsequent section. Further, as mentioned above, none of these equations are applicable to models A2 and B2, which possess independent correlation lengths for $b(z)$ and $\theta(z)$.

3.3.2 Numerical Results

In this subsection, we investigate the statistical properties of the PMD through numerical simulations. In particular, we first examine the root mean square DGD and then the evolution of the probability density function (pdf) of the DGD with fiber length, since knowledge of these values enables the estimation of many additional properties associated with polarized light propagation in fibers.

For simplicity, our numerical studies of the root mean square DGD, τ_{rms}, are confined to Models A1 and B1, which require three parameters ϵ, Λ_{beat} and L_f. Given these parameters, a series of birefringence values is generated based on the defining equations of the corresponding models. The DGD is then calculated with the standard transfer matrix formula from these values. After repeating this calculation, we evaluate the ensemble average of the root mean square DGD τ_{rms}.

We now investigate the variation of τ_{rms} with respect to ϵ, Λ_{beat} and L_f. Considering first the dependence of τ_{rms} on ϵ for $0 < \epsilon < 1$, $\Lambda_{beat} = 15\,m$ and $L_f = 10\,m$, we obtain the $\times$ and $\circ$ markers in Fig. 3.5 for models A1 and B1 at $z = 200\,m$, where each value in this and our subsequent curves are averaged over 10^5 realizations. Clearly, while τ_{rms} differs in the two models, in both cases it decreases monotonically with ϵ in the interval [0, 1], as noted in Section 3.3.1. Further, for a given ϵ, τ_{rms} is always larger for Model A1 than for Model B1, which is expected as a result of the additional fluctuation source term and thus larger polarization coupling in Model B1, c.f. Section 2.5 and Fig. 2.2. The analytic values for the root mean square DGD, τ^*_{rms} given by Eq. (3.23) as a function of ϵ, Λ_{beat} and Ł$_f$ are displayed as the solid curves in Fig. 3.5 and in the two subsequent figures respectively. The correlation lengths in Eq. (3.23) are calculated according to $L_{corr} = \nu(\epsilon)\, L_f$ and Eq. (2.38), which yields $L_{corr} = 10^6\, L_f, 100\, L_f, 1.78\, L_f, 1.01\, L_f$ for $\epsilon = 10^{-6}$, 0.01, 0.60, 0.99. While the simplified analytic expression is valid for $\epsilon \to 0$ and $\epsilon \to 1$, the results of Model A1 or B1 do not agree with Eq. (3.23) away from these limiting values.

We display next in Fig. 3.6 the base 10 logarithm of τ_{rms} as a function of Λ_{beat} for $0 < \Lambda_{beat} < 30\,m$. These results are calculated with Model B1 for $\epsilon =$ 0.01, 0.60, 0.99, $L_f = 10\,m$ and $z = 100\,m$. Since longer beat lengths imply reduced birefringence, τ_{rms} is a decreasing function of Λ_{beat} for all three ϵ values. Similarly, τ_{rms} decreases for larger ϵ since greater random fluctuations yield enhanced modal coupling.

That the variation of τ_{rms} with L_f is highly dependent on the value of ϵ is further evident from Fig. 3.7, which displays the results of Model B1 at $z = 100\,m$ for $\epsilon = 10^{-6}$, 0.01, 0.60, 0.99 and $\Lambda_{beat} = 10\,m$. Evidently, for $\epsilon \approx 0$, corresponding to a polarization maintaining (PM) fiber, the PMD, namely τ_{rms}, is nearly constant

over the interval $0 < L_F < 30$. Further, as expected, this value of ϵ maximizes τ_{rms} since a PM fiber has a greater PMD than fibers with random birefringence. For large values of ϵ, however, τ_{rms} increases quadratically as a function of L_f. For intermediate values of ϵ such as $\epsilon = 0.01$, τ_{rms} grows rapidly for small L_f and then slowly approaches a maximum value for large L_f.

While the polarization mode coupling predicted by any model of random birefringence effects induces full mode mixing in the long-length limit, leading to a square-root dependence of DGD on length, the approach to this asymptotic behavior differs among birefringence models. Specializing to Model B1, we display in Fig. 3.8 the variation of τ_{rms}, again averaged over 10^5 realizations, with the normalized fiber length $L = z/L_f$ for $L < 50$, $\epsilon = 0.01, 0.10, 0.20, 0.99$, $\Lambda_{beat} = 15\,m$ and $L_f = 10\,m$. As expected, for the nearly constant birefringence case $\epsilon = 0.01$, τ_{rms} increases linearly with L, while it grows approximately quadratically for $\epsilon = 0.99$. In the remaining cases, $\epsilon = 0.10, 0.20$, τ_{rms} is a linear function of L at small fiber lengths but becomes quadratic as $L \to \infty$. To demonstrate this explicitly, we plot τ_{rms} as a function of $\sqrt{L}$ for $\epsilon = 0.20, 0.60, 0.99$ in Fig. 3.9 together with linear least-square fits to these curves, as indicated by solid lines. Clearly, for all three values of ϵ, τ_{rms} approaches a linear function of $\sqrt{L}$ at sufficiently long fiber lengths. Further, the curves are increasingly linear at shorter fiber lengths for larger ϵ.

Finally, we examine the evolution of the pdf of DGD, ρ , with fiber length as in Section 3.2. The DGD, τ, is evaluated with our four models, while we employ 10^6 realizations and evaluate the pdf for $\Lambda_{beat} = 20\,m$, $\epsilon = 0.60$ and $L_f = 12\,m$. For models A2 and B2, we set the correlation length of θ, $L_\theta = 10\,m$. The pdf curves will be evaluated at normalized fiber lengths given by $L = 1.5, 2.5, 5, 10, 20, 100, 500, 1000$.

In Fig. 3.10, we display the base 10 logarithm of the pdf, ρ, of the DGD as a function of τ for $L = 20$ and $L = 100$, where the results for the models A1, B1, A2 and B2, are displayed in separate subfigures (a)-(d), respectively. The corresponding curves for $L = 500$ and $L = 1000$ are presented in Fig. 3.11. The solid lines of these curves are the corresponding Maxwell distributions. The pdf here approaches the Maxwell distribution from above in models A1 and B1, and below in models A2 and B2 as the fiber length increases from $L = 20$ to $L = 100$ while it

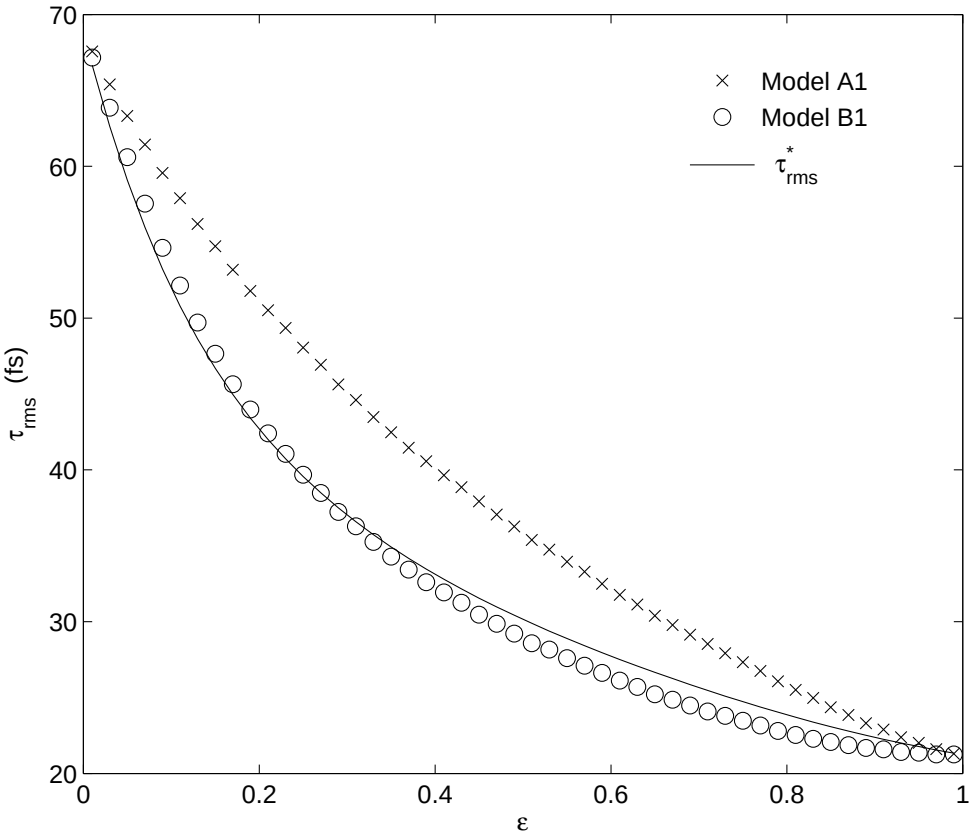

Figure 3.5: τ_{rms} as a function of ϵ according to models A1 ($\times$) and B1 ($\circ$) for a fiber length $L = 200\,m$ with beat length $\Lambda_{beat} = 15\,m$ and $L_f = 10\,m$. The solid line is the analytic value for the root mean square DGD, τ^*_{rms}.

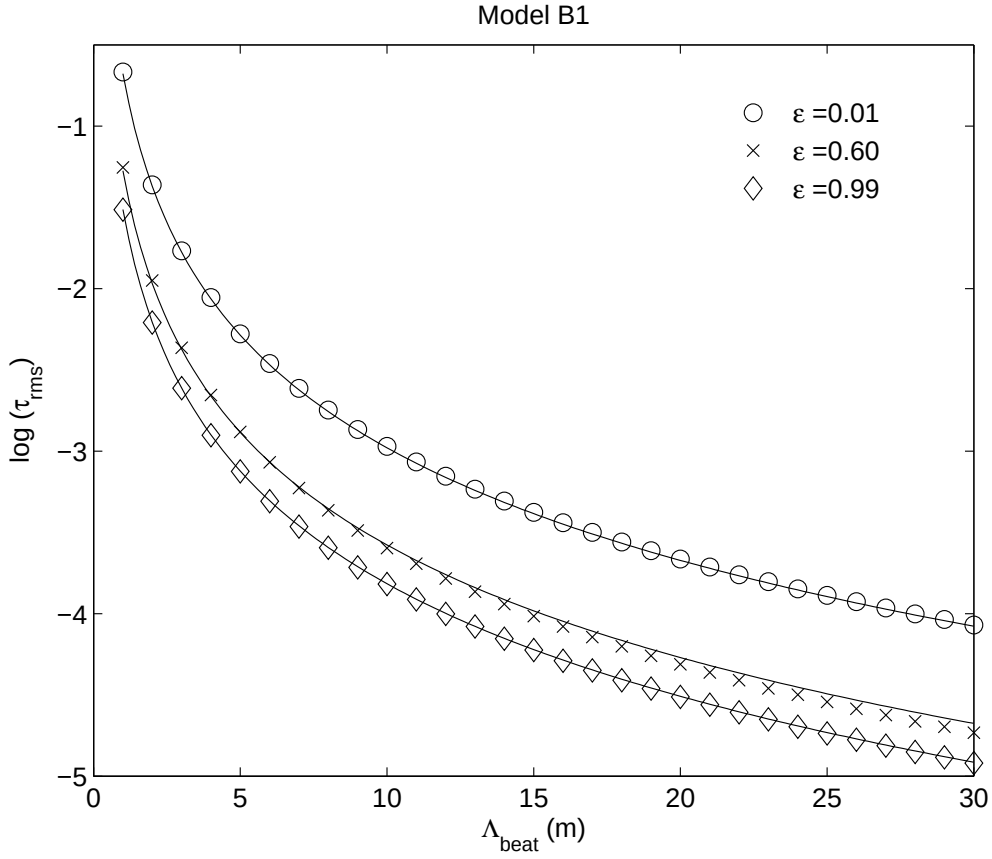

Figure 3.6: τ_{rms} as a function of Λ_{beat} according to Model B1 for $\epsilon = 0.01,\ 0.60,\ 0.99$ for a fiber length $z = 100\,m$ with $L_f = 10\,m$. The solid line is the analytic value for the root mean square DGD, τ^*_{rms}.

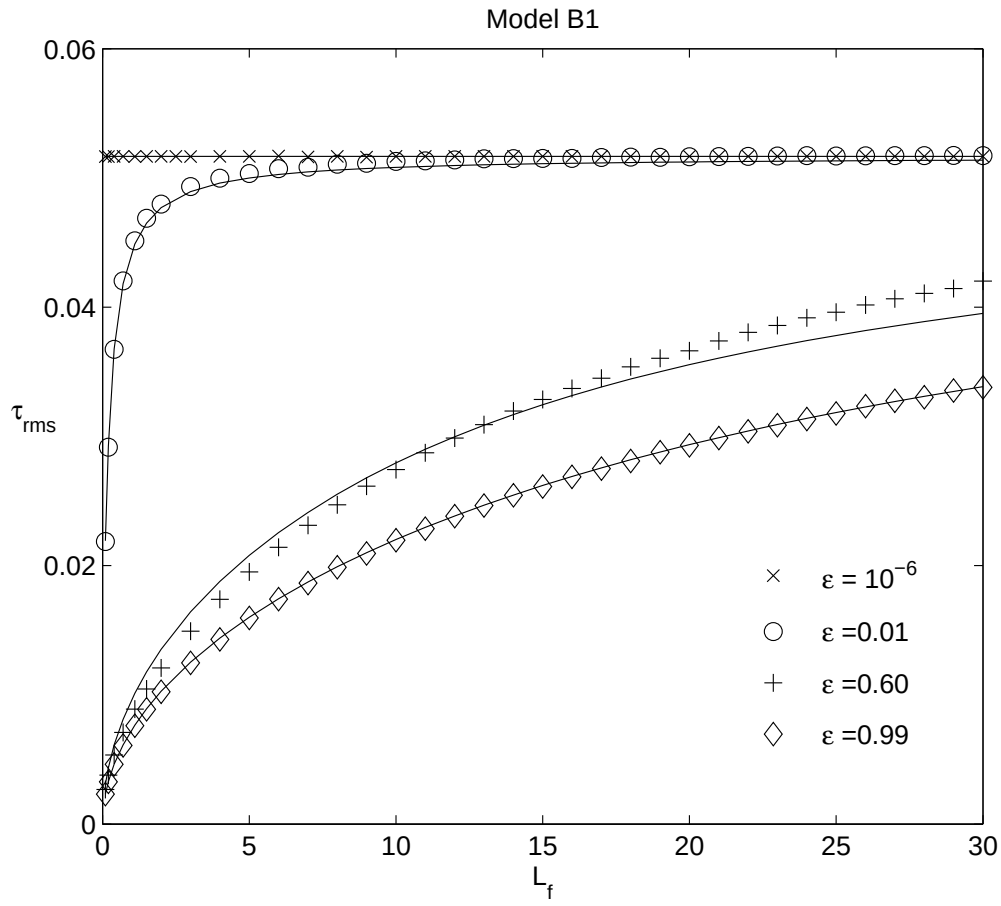

Figure 3.7: τ_{rms} as a function of Ł$_f$ according to Model B1 for $\epsilon = 10^{-6}$, 0.01, 0.60, 0.99 for a fiber length $z = 100\,m$ with $\Lambda_{beat} = 10\,m$. The solid line is the analytic value for the root mean square DGD, τ^*_{rms}.

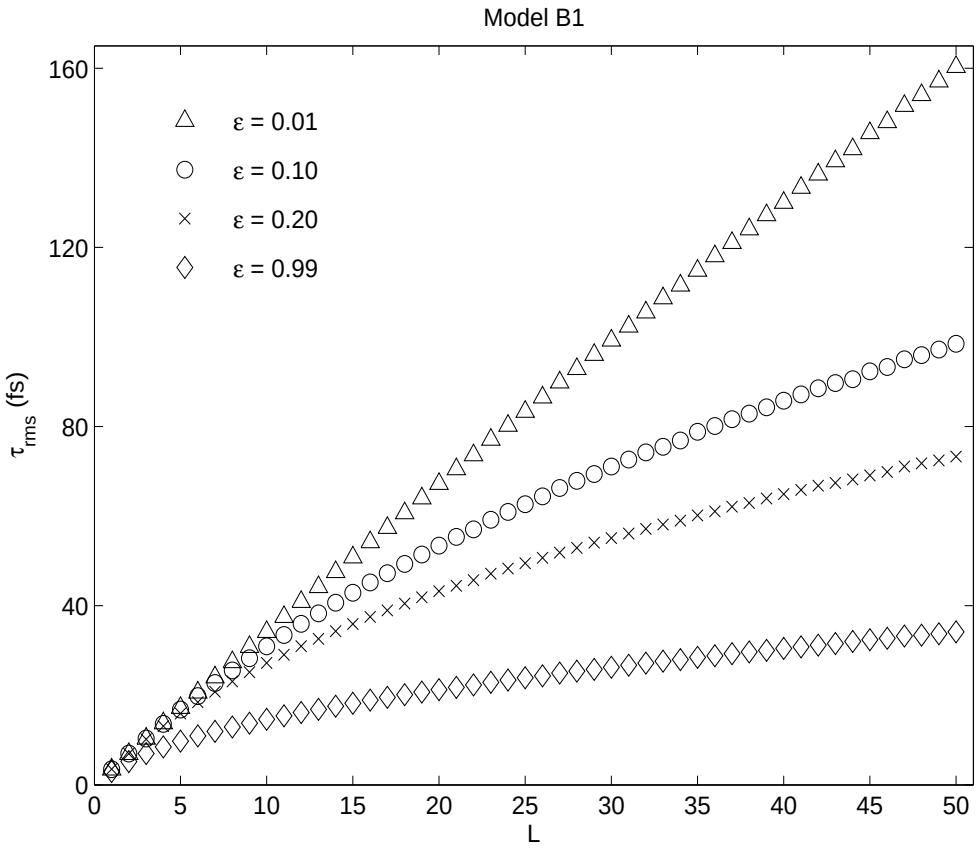

Figure 3.8: τ_{rms} as a function of fiber length L according to Model B1 for $\epsilon = 0.01, 0.10, 0.20, 0.99$ with $\Lambda_{beat} = 15\,m$ and $L_f = 10\,m$.

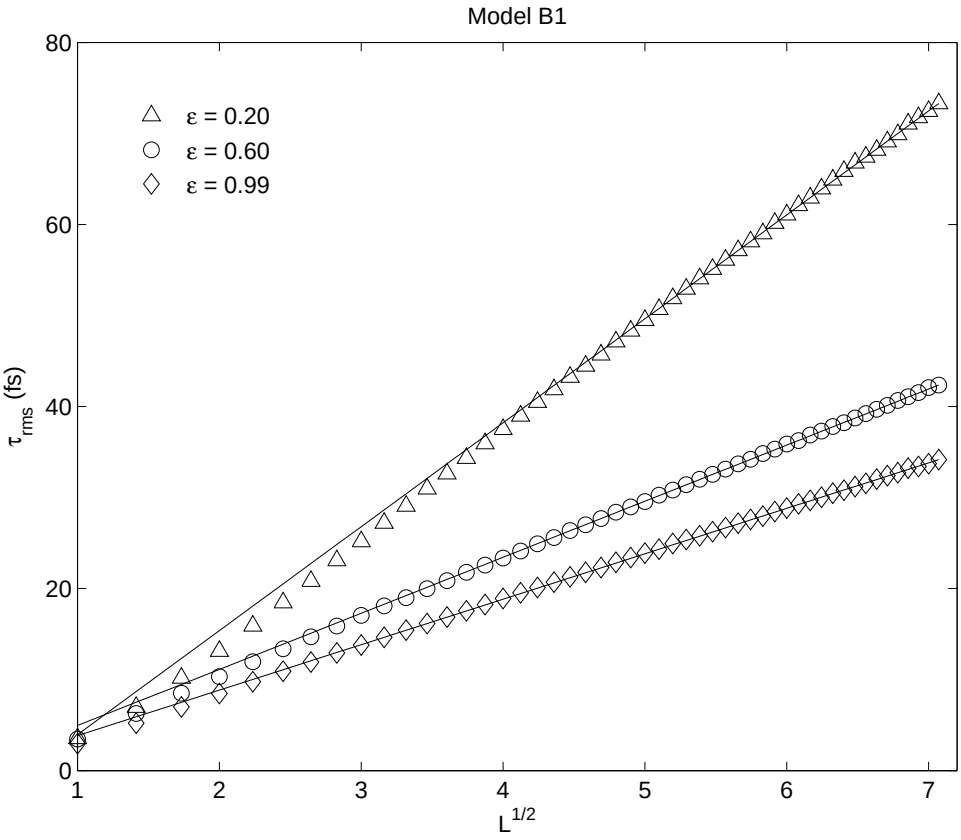

Figure 3.9: τ_{rms} as a function of $\sqrt{L}$ according to Model B1 for $\epsilon = 0.20$, 0.60, 0.99 with $\Lambda_{beat} = 15\,m$ and $L_f = 10\,m$. The solid lines are linear least-square approximations to the corresponding curves.

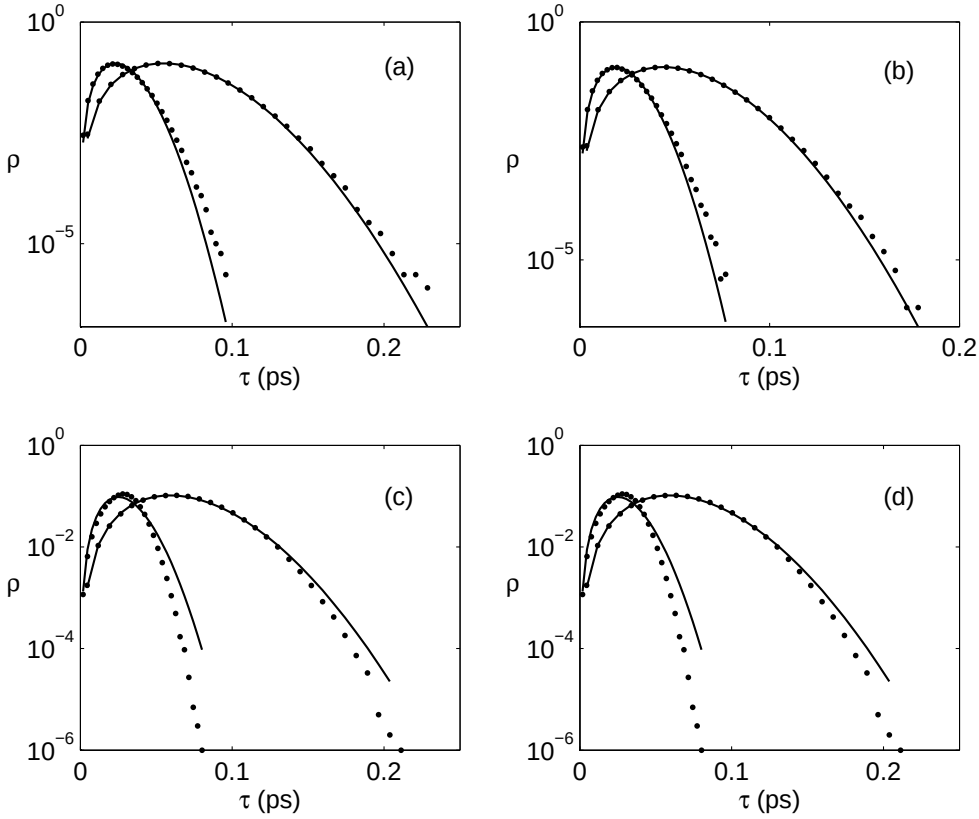

Figure 3.10: The base 10 logarithm of the pdf ρ as a function of DGD τ for L= 20 and 100 according to models (a) A1, (b) B1, (c) A2, and (d) B2. The dotted curves are numerical simulations, while the solid curves are the Maxwell distributions.

overlaps with the Maxwell distribution for all four models at $L = 1000$. Moreover, for the same parameter values, models A1 and B1 predict a different mean DGD than models A2 and B2. Therefore, as discussed in Section 2, the mean DGD depends upon the details of the birefringence, and cannot be accurately predicted by a simple approximation such as Eq. (3.23).

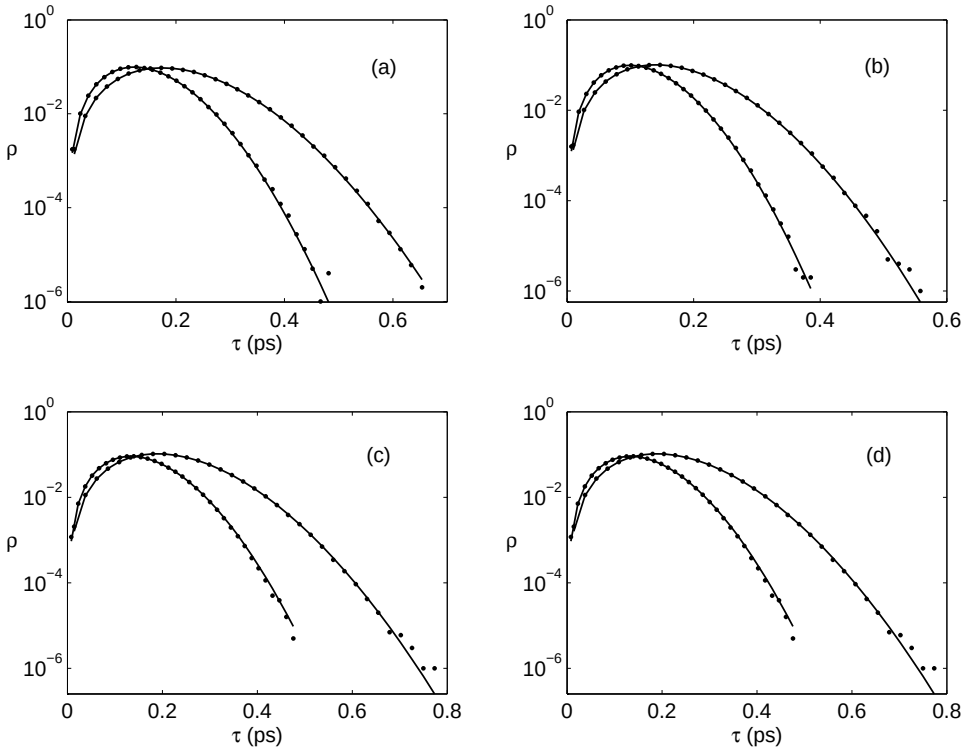

Figure 3.11: The base 10 logarithm of the pdf ρ as a function of DGD τ for L= 500, and 1000 according to models (a) A1, (b) B1, (c) A2, and (d) B2. The dotted curves are numerical simulations, while the solid curves are the Maxwell distributions.

We now examine evolution of the pdf of the DGD with fiber length at all length scales. To simplify the discussion, we first compute the variance of the deviation of

our pdf, $\rho(n)$, from the Maxwell distribution, $\rho_m(n)$, with the same mean DGD,

$$\begin{aligned} \delta_v &= \sum_{n=0}^{M} (\rho_m(n) - \rho(n))(\tau_b^2(n) - \bar{\tau}_b^2) \\ \bar{\tau}_b &= \sum_{n=0}^{M} \rho\tau_b(n) \end{aligned} \tag{3.24}$$

in which we typically employ $M = 40$ histogram bins. Figure 3.12 displays the variation of δ_v with $log(L)$ as L increases from 1.5 to 1000 for Model A1 ($\circ$), Model B1 ($\times$), Model A2 ($\diamond$), and Model B2 ($*$). The solid line further designates $\delta_v = 0$. Evidently, the Model A1 and Model B1 curves, as well as the Model A2 and Model B2 curves nearly overlap, indicating that the statistical properties of procedures A and B are similar, despite the differing birefringence behaviors. Moreover, although $\delta_v \to 0$ as $L \to \infty$ for all four models, the approach is monotonic for Model A2 or B2, while for Model A1 and B1, δ_v first crosses zero at $L_0 = 2.16$ for Model A1 and $L_0 = 1.61$ for Model B1, after which it asymptotically approaches zero.

As implied from Equation (4.2), $\delta_v = 0$ is a necessary but not sufficient condition for the pdf to coincide with a Maxwell distribution. To investigate further the convergence of the pdf to a Maxwell distribution, we display the pdf as a function of the DGD for $L = 1.5$, 2.5, 5, 10, 20, 100, 500, 1000. These graphs confirm that the evolution of the pdf in models A1 and B1 is similar to that of the RMM, while the curves for models A2 and B2 resemble those of the FMM, which is explained by the relatively large value of ϵ, as we will discuss at the end of this section. That is, for models A2 and B2, the pdf approaches a Maxwell distribution monotonically with fiber length as predicted by our previous results for δ_v. However, for models A2 and B2, while the δ_v curves indicate the major features of the pdf results, the pdf evolves rapidly towards the Maxwell distribution for $L \leq L_0$, which leads to a distorted curve in the vicinity of L_0. The pdf then deviates further from the Maxwell distribution until $L \sim 5$. For $L > 5$, the pdf again approaches the Maxwell distribution asymptotically.

The pdf at $L = L_0$ is plotted on a linear scale in Fig. 3.13 (a) and (b) for Models A1 and B1, while the pdf at $L = 1000$ is given in Fig. 3.13 (c) for Model A1 and (d) for Model B1 for comparison. The solid curves are the Maxwell distributions

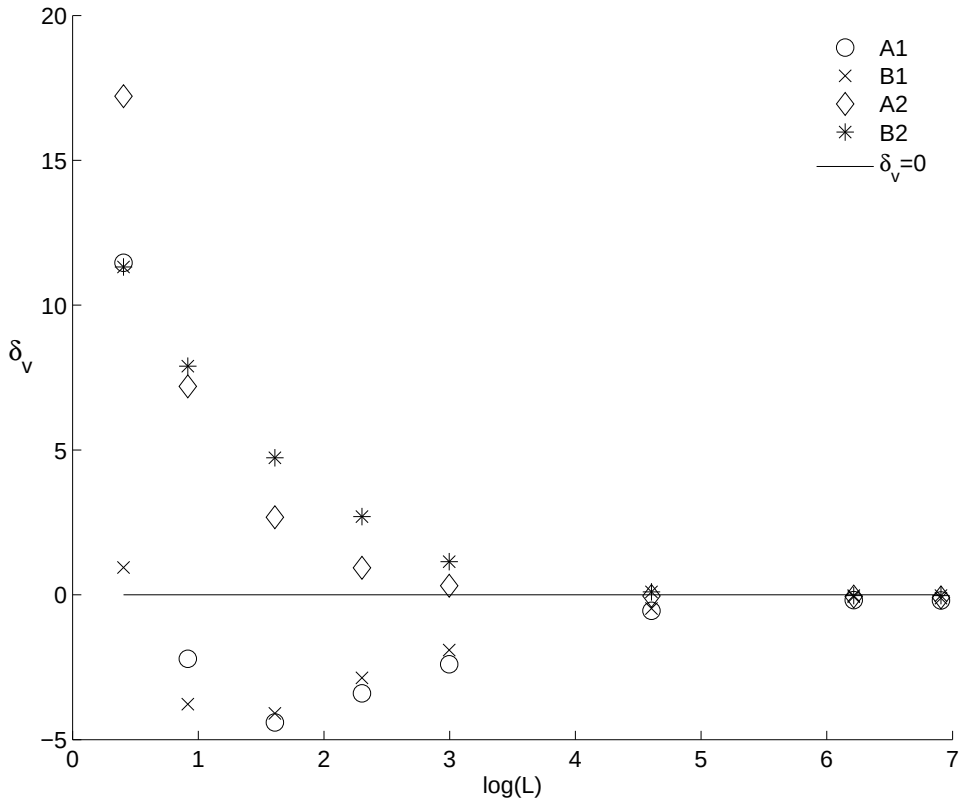

Figure 3.12: δ_v as a function of $log(L)$ from models A1 ($\circ$), B1 ($\times$), A2 ($\diamond$), and B2 ($*$). The solid line designates $\delta_v = 0$.

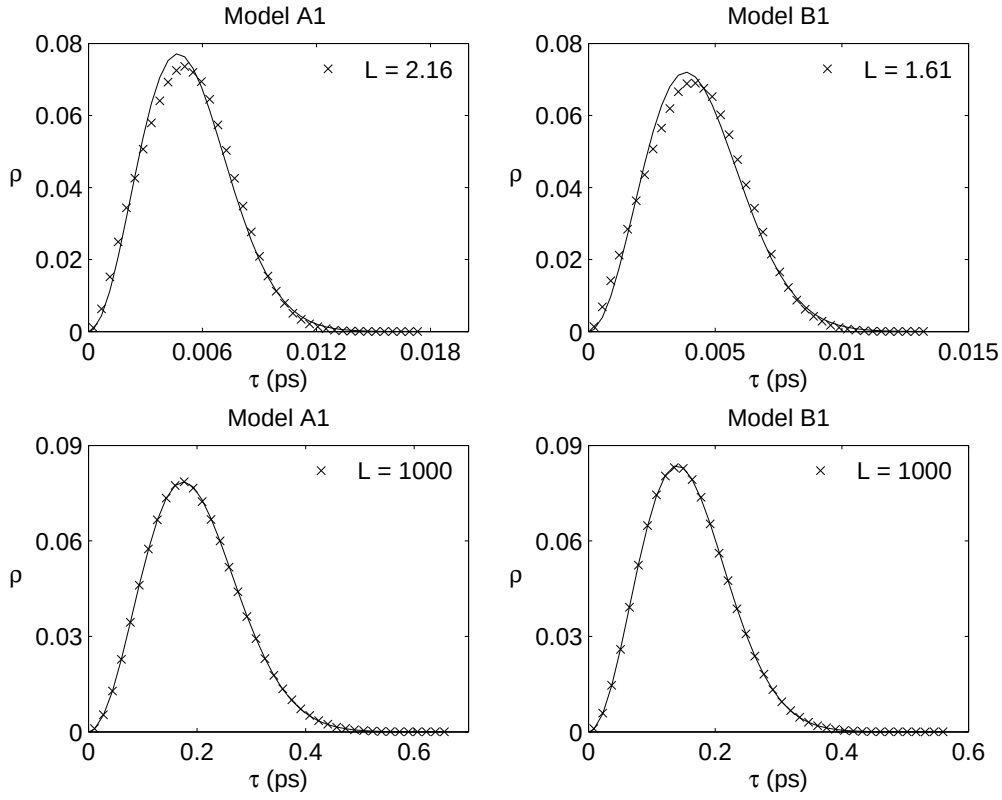

Figure 3.13: The variation of the pdf ρ with DGD τ for (a) Model A1 at $L = 2.16$, (b) Model B1 at $L = 1.61$, (c) Model A1 at $L = 1000$, and (d) Model B1 at $L = 1000$. The solid curves are the corresponding Maxwell distributions.

with the corresponding mean DGD values. While $\delta_v = 0$ at $L = L_0$, $\delta_v \simeq 0.1$ and $\delta_v \simeq 0.2$ at $L = 1000$ for models A1 and B1 respectively, for which $\delta_v = 0$ is only approached asymptotically for large L. Clearly, the pdf of the DGD resembles a distorted Maxwell distribution for models A1 and B1 at $L = L_0$, unlike the pdf at $L = 1000$, which, as expected, agrees nearly perfectly with the Maxwell curve.

That our results for models A1 and B1 approximately reproduce those of the RMM, while those for models A2 and B2 are close to the FMM is related to the relatively large values that we have employed for ϵ. For small ϵ, the form of the pdf of the DGD can be substantially modified. To illustrate, we have calculated the pdf and δ_v for $L = 100$ in Model B1 as a function of ϵ with $0 < \epsilon < 1$. The dependence of δ_v on ϵ is displayed in Fig. 3.14. Evidently, δ_v decreases with ϵ, indicating that the pdf of the DGD deviates more substantially from the Maxwell distribution for smaller ϵ. Moreover, for $0 < \epsilon < 0.5$, δ_v falls rapidly with ϵ while δ_v varies more slowly for $0.5 < \epsilon < 1$. This at least partially explains the similarity of our previous curves for models A1 and B1 with $\epsilon = 0.6$ with those of the RMM, which is obtained from Model A1 or B1 when $\epsilon \to 1$.

3.3.3 Conclusions

We have examined the predictions of the two existing models of fiber birefringence for the PMD of short fiber lengths. While our FMM calculations agree as expected with the analysis of J. Yang etc. [61], the evolution of the pdf of the DGD for the FMM differs rather unexpectedly from the RMM result for fiber lengths close to or shorter than the correlation length (although the models of course agree in the limit of long fiber lengths). Further, for long but finite fiber length, the FMM yields a smaller outage probability than that predicted from the Maxwell distribution while the RMM instead predicts a larger outage probability. Our results could potentially be employed experimentally, possibly with an efficient non-invasive method for measuring the evolution of the PMD over numerous short lengths of a given fiber to determine the physical properties of the birefringence.

We have also examined the statistical properties of the PMD based on the four models proposed in Chapter 2 through both theoretical analysis and numerical

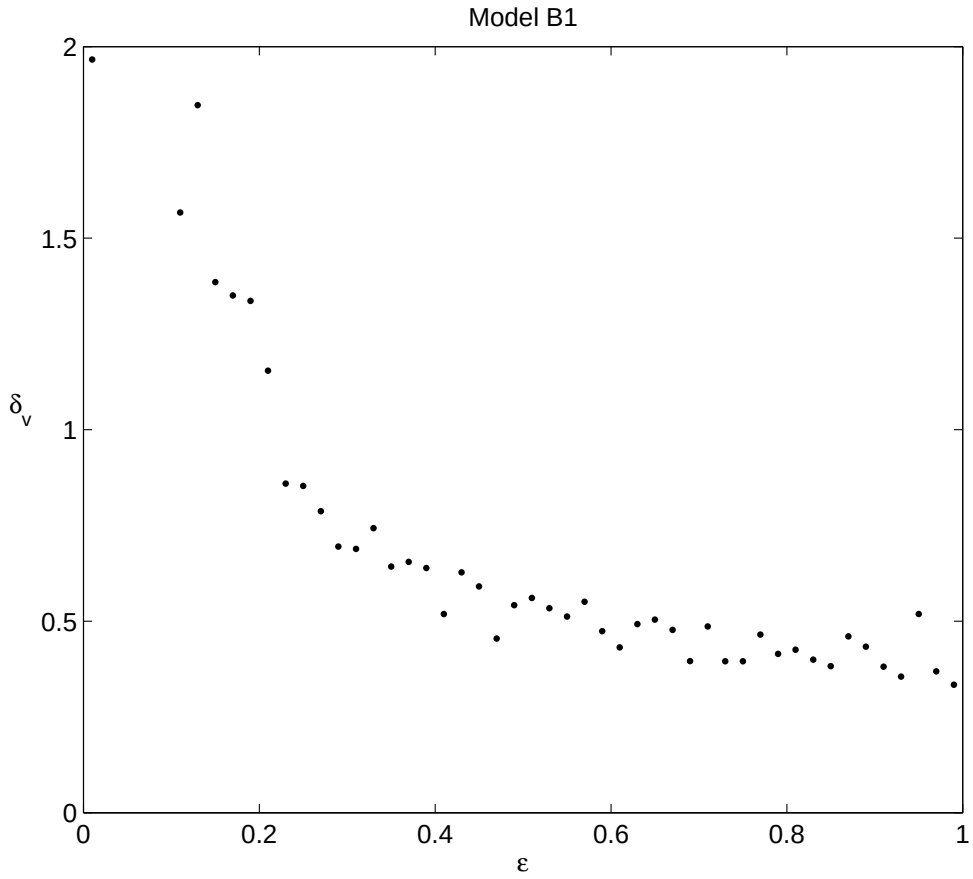

Figure 3.14: The variation of δ_v with ϵ for Model B1 with $L = 100$.

simulations. The models can be adapted to a broad range of birefringent fibers, ranging from nearly polarization-maintaining fibers to fibers with very large polarization mode coupling. Further, they generate different fluctuation behavior for the birefringence along the fiber and therefore lead to different formulas for the root mean square DGD as a function of longitudinal distance. These statistical properties could in principle be employed to distinguish between different birefringence behavior through repeated measurements on short optical fiber segments, possibly subject to time-dependent environmental fluctuations. In Chapter 4, we will derive analogous results for spun fibers.

Chapter 4

Polarization Mode Dispersion Mitigation through Compensation and Spun Fibers

Polarization mode dispersion (PMD) mitigation can be achieved through two approaches. The first is to compensate the PMD in already installed systems. Because PMD fluctuates in time, the compensation must be applied in-site and dynamically, greatly complicating the development of compensators and adding substantially to their expense. The second approach is to design low-PMD fibers. One procedure for manufacturing low PMD fibers involves spinning the fiber during the fiber drawing process [65, 66]. Generally, the fiber is rotated with tractors, which induces a similar rotation of the fiber's birefringence axis along the fiber length. This spinning can be applied at either a constant or a variable rate. The latter procedure appears to reduce PMD more than the former. Spinning was implemented in fiber manufacturing about a decade ago to reduce the PMD of transmission fibers. Experimentally, the PMD coefficient was reduced from $1.0 - 0.1ps/\sqrt{km}$ to $0.05 - 0.01ps/\sqrt{km}$ [67–69], which as we see, is in almost exact agreement with the results of this chapter. Accordingly, in this chapter, we study both approaches. In section 4.1, we examine PMD reduction of sinusoidally spun fiber, while second 4.2 introduces different procedures for PMD compensation and mitigation.

4.1 The PMD Reduction of Sinusoidally Spun Fibers

PMD reduction in spun fibers was initially examined under the assumption that the birefringence magnitude was constant or slowly-varying [65, 66, 70–74]. Later, the effects of random birefringence variations were included with the aid of two physical birefringence models, i.e., the random-modulus model (RMM) and the fixed-modulus model (FMM) [62, 63, 75–77]. The two methods predict different PMD properties [63], indicating the importance of an accurate statistical model of the fiber birefringence. In this section, we study sinusoidal spun fibers based on a modified random modulus model (MRMM) denoted as Model B1 in Chapter 2. While in the FMM and RMM, the amplitude of the birefringence fluctuations are either zero or a fixed value, the MRMM enables this amplitude to be set arbitrarily. Accordingly, in this section we simulate PMD reduction and the DGD statistics of spun fibers with arbitrary birefringence profiles.

4.1.1 Numerical Results

We now consider fibers subjected to a sinusoidal spin function $A(z) = A_0 \sin 2\pi z/p$, where p and A_0 are termed the spin period and amplitude, respectively. We first investigate the PMD reduction as a function of both the fiber parameters and the spin amplitude, and then compare the evolution of the probability density function (pdf) of the DGD along fiber length in spun fibers to that of standard fibers.

The degree of PMD reduction through spinning is often specified through the spin-induced reduction factor (SIRF), defined by [76]

$$SIRF = \frac{\tau_{rms}^{s}}{\tau_{rms}}. \tag{4.1}$$

Here τ_{rms}^{s} is the root mean square DGD of the spun fiber and τ_{rms} is that of standard fiber. In our numerical studies, we model a linearly birefringent single mode fiber of length z by N sections of PM fiber with a section size $\Delta z = z/N$ that is much shorter than both the polarization beat length Λ_{beat} and the inverse

coupling strength L_f. Random sequences of the two orthogonal components of the birefringence vector $\mathbf{b}(n)$ are then generated from the MRMM, c.f. Chapter 2. From these values, we compute the evolution of the birefringence along the fiber length, i.e., the principal birefringence axis angle $\theta(n)$ and the birefringence modulus $b(n)$. Assuming that fiber spinning rotates the birefringence axis without affecting the birefringence strength [75] results in $\vartheta(n) = \theta(n) + A(n)$ for the principal birefringence axis angle. The differential group delay (DGD) of both spun and standard fibers is then evaluated with a transfer matrix method from the computed birefringence as a function of length c.f. Chapter 3. PMD statistics, such as the root mean square DGD and the pdf of the DGD, are estimated by repeating our calculations for 10^5 realizations.

In the MRMM, the fiber birefringence is characterized by three parameters, ϵ, L_f and Λ_{beat}, that vary among fibers and further depend on the environmental properties. We accordingly first calculate the variation of the SIRF with respect to these three parameters for a spin period $p = 4\,m$ and amplitude $A_0 = 2.75\,rad.$ As is evident from Section 2.5 and Fig. 2.2, the value of ϵ determines the main characteristics of the random birefringence profile. Thus, while for $0 < \epsilon < 0.5$ the profile varies randomly with small fluctuation amplitude, for larger ϵ, in the range $0.5 < \epsilon < 0.9$, the birefringence variations become pronounced. To investigate the influence of the fiber spin on PMD reduction in the presence of random birefringence, we first display in Fig. 4.1 the SIRF ($\times$) as a function of ϵ for $0 < \epsilon < 1$ with $\Lambda_{beat} = 10\,m$ and $L_f = 5\,m$ for a fiber length $z = 500\,m$. In this figure, the corresponding result for a PM fiber is also plotted as a point denoted by $\circ$. Evidently, the SIRF is larger for large ϵ and increases monotonically with ϵ for $\epsilon > 0.4$, indicating that the PMD reduction is less effective for more pronounced random birefringence variations. This is expected, since for PM fibers, periodic sinusoidal spinning reduces the PMD to zero due to precise phase matching; however the fluctuations of the birefringence result in a certain average deviation from the phase matching condition and therefore gives rise to a corresponding increase in the reduction factor.

Fig. 4.2 displays the SIRF as a function of L_f for $0 < L_f < 30\,m$ with $\Lambda_{beat} = 10\,m$ and $z = 500\,m$. The three curves are computed with $\epsilon = 0.01\,\circ$, $\epsilon = 0.20\,\times$

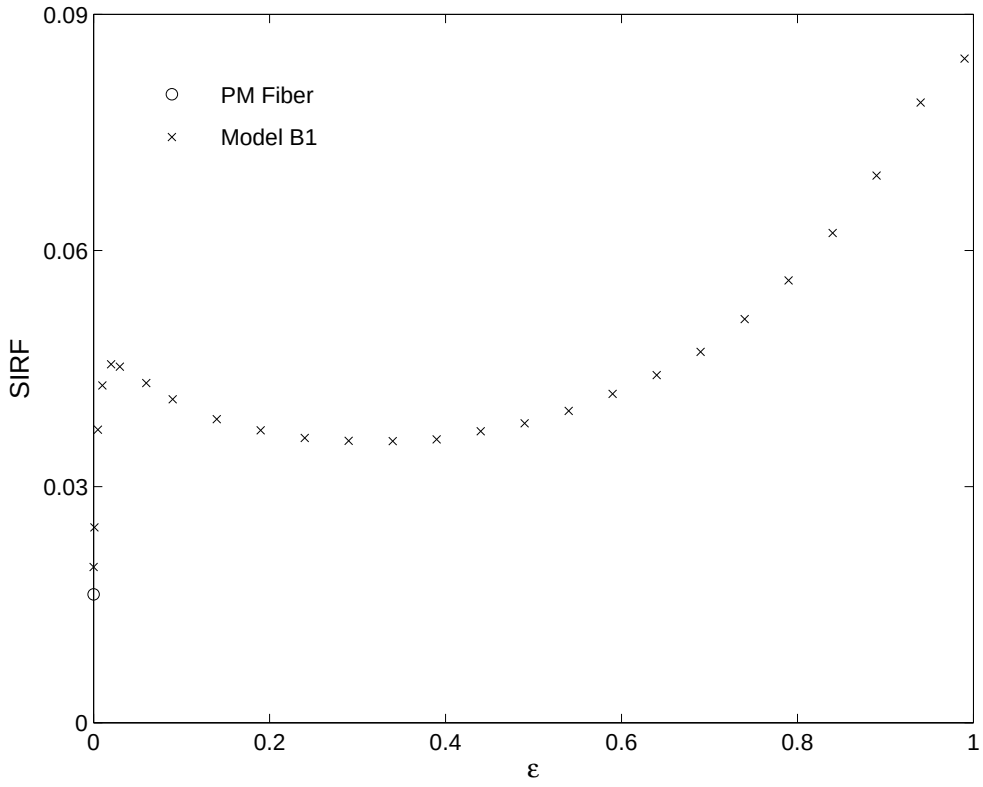

Figure 4.1: The SIRF ($\times$) as a function of ϵ for $0 < \epsilon < 1$ with $\Lambda_{beat} = 10\,m$, $Ł_f = 5\,m$ and $z = 500\,m$. The point indicated by $\circ$ is the PM fiber result.

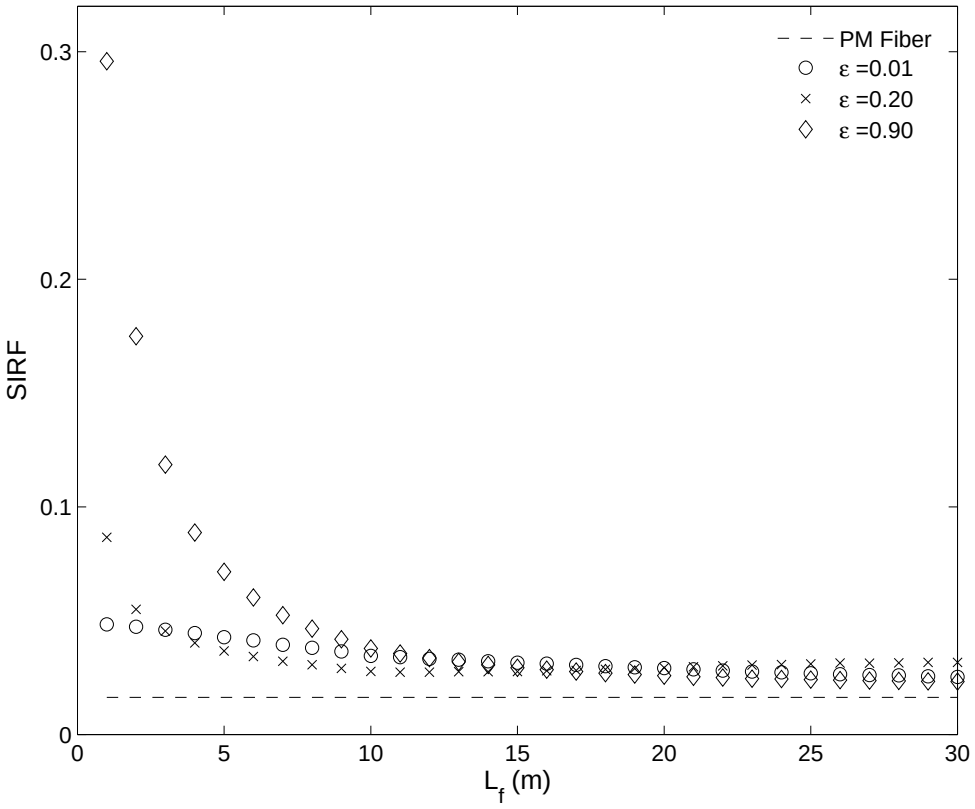

Figure 4.2: The SIRF as a function of L_f for $1 < L_f < 30\,m$ with $z = 500\,m$, $\Lambda_{beat} = 10\,m$, and $\epsilon = 0.01$ $\circ$, $\epsilon = 0.20$ $\times$, and $\epsilon = 0.90$ $\diamond$. The dashed line corresponds to the PM fiber results.

and $\epsilon = 0.90\,\diamond$, while the corresponding result for a PM fiber is presented as the dashed line in the figure. In the MRMM, Ł$_f$ varies inversely with the correlation (coupling) length such that the mode coupling induced by birefringence fluctuations is enhanced when Ł$_f \to 0$. Hence, for $L_f < 10\,m$, the SIRF decreases with L_f and increases with ϵ, while for $L_f > 10\,m$, the SIRF is small and nearly independent of L_f, and is further nearly identical for all three cases. Indeed, for values of L_f approaching zero, the large effective random mode coupling removes considerably the spin-induced PMD reduction, especially for large ϵ. Moreover, as ϵ decreases from 0.90 to 0.01, the SIRF curves vary less with L_f, and therefore approach the behavior of PM fiber, for which the PMD is independent of L_f, c.f. Fig. 3.7. This is expected, since in the limit of $\epsilon \to 0$, the MRMM reduces to a PM fiber model. The curves in Figs. 4.1 and 4.2 for the PMD of spun fiber as a function of the random birefringence fluctuation strength ϵ and the inverse coupling length L_f are new results of our model.

Next, in Fig. 4.3, we display the SIRF as a function of beat length for $0 < \Lambda_{beat} < 30\,m$, with $L_f = 5\,m$ and $z = 500\,m$. As in Fig. 4.2, the three SIRF curves correspond to $\epsilon = 0.01\,\circ$, $\epsilon = 0.20\,\times$ and $\epsilon = 0.90\,\diamond$, while the dashed line is the PM fiber result. As expected, the SIRF of the three ϵ values becomes nearly independent of the beat length for $\Lambda_{beat} > 10\,m$ as for PM fiber when Λ_{beat} is much longer than the spin period. For $\Lambda_{beat} < 10\,m$ the SIRF fluctuates noticeably at small ϵ. This behavior is similar to that of a periodically spun PM fiber, for which a large maximum appears at $\Lambda_{beat} = 2.1\,m$ together with two more smaller maxima at $\Lambda_{beat} = 25\,m$ and $28.5\,m$. While the first maximum is still noticeable for $\epsilon = 0.20$, 0.01, the secondary maxima are not visible in these two curves. For $\epsilon = 0.9$, the large birefringence fluctuations effectively suppress the first maximum as well. In addition to the novel curves shown above for the variation of the PMD reduction factor with beat length for different random birefringence profiles, our results for PM fiber are slightly different from the previously reported results of [66].

We now implement the MRMM to study the variation of the SIRF with spin amplitude A_0 for $0 < A_0 < 5\,rad$ for different random birefringence profiles with $p = 4\,m$, $\Lambda_{beat} = 20\,m$ and $\epsilon = 0.01,\, 0.20, 0.90$. Since the resulting curves depend strongly on L_f, we present results for $L_f = 1\,m$, $L_f = 5\,m$ and $L_f = 25\,m$ in Figs.

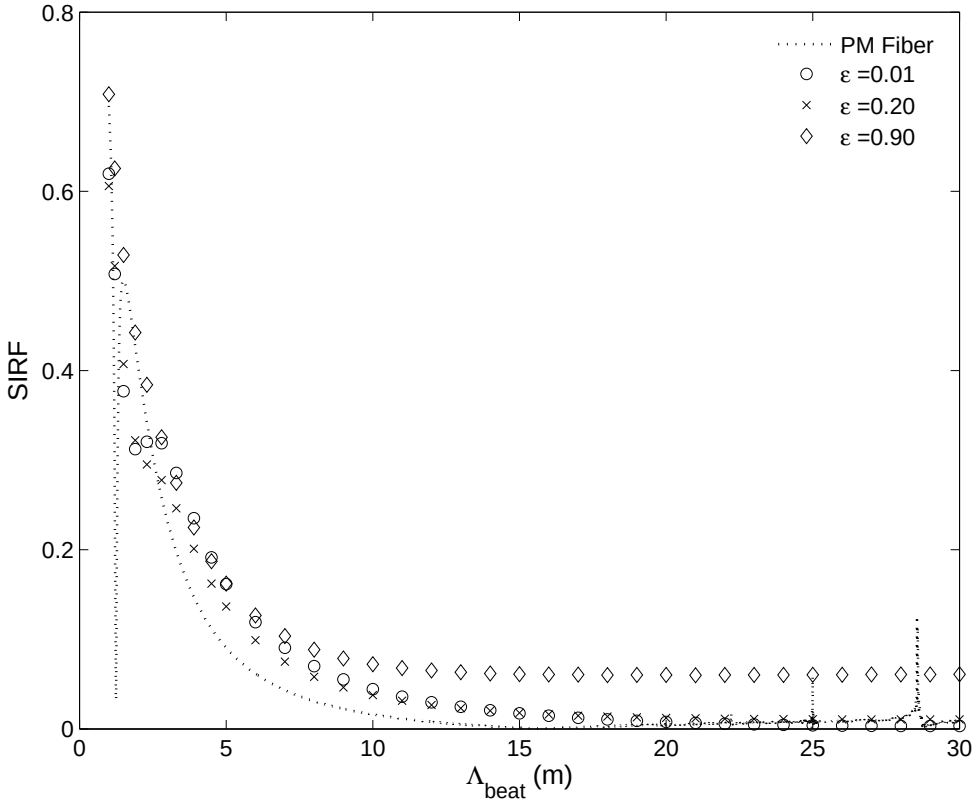

Figure 4.3: The SIRF as a function of Λ_{beat} for $1 < \Lambda_{beat} < 30\,m$ with $z = 500\,m$, $\mathrm{L}_f = 5\,m$, and $\epsilon = 0.01$ $\circ$, $\epsilon = 0.20$ $\times$, and $\epsilon = 0.90$ $\diamond$. The dashed line again corresponds to a PM fiber.

4.4, 4.5, and 4.6, respectively, with $z < 100\,L_f$, which is sufficient to illustrate the asymptotic behavior. In these three figures, $\circ$, $\times$ and $\diamond$ indicate the $\epsilon = 0.01$, $\epsilon = 0.20$ and $\epsilon = 0.90$ values, respectively. For short sinusoidal spin periods, i.e., $p \ll \Lambda_{beat}$, both the PM fiber and the RMM predict that the PMD reduction is optimal when the spin amplitude satisfies the phase matching condition $J_0(2A_0) = 0$, where J_0 is the zeroth-order Bessel function of the first kind [65]. Accordingly, for all L_f and ϵ, our curves have local minima at $A_0 = 1.20,\ 2.75,\ 4.33, ...$ That is, the phase matching condition yields an optimum solution for the spin amplitude for short spin periods, independent of the birefringence profile variations. Moreover, the SIRF is an oscillating function of the spin amplitude with a monotonically decreasing average value. Other aspects of the curves depend strongly on ϵ and L_f. For example, for $L_f = 1$, the local minima of the SIRF are pronounced for large ϵ, but vanish for $\epsilon = 0.01$. This again demonstrates that the PMD reduction factor of spun fiber increases when the random birefringence is large (for small L_f) because of the resulting changes in the relative phase of the two fiber modes. As is evident from our curves for $L_f = 5,\ 25$, the three curves nearly overlap, with minima close to zero (except for the third minimum for $L_f = 25\,m$). While our results for $\epsilon = 0.9$ are similar to those of the RMM [76], the variation of the PMD reduction as a function of the spin amplitude for different birefringence profiles has not been examined previously.

For short period PM fibers, sinusoidal spinning yields periodic fluctuations in the DGD as a function of length when the phase matching condition is satisfied [65]. Although the DGD is not periodic in a randomly birefringent fiber, an optimum PMD reduction can still be achieved. To illustrate, we display in Fig. 4.7 the SIRF calculated with the MRMM as a function of normalized fiber lengths L with $L_f = 15\,m$, $\Lambda_{beat} = 20\,m$ and $\epsilon = 0.01\ \circ$, $\epsilon = 0.20\ \diamond$, and $\epsilon = 0.90\ \times$. The PM fiber result is shown as a dashed line with $\triangle$ markers. To satisfy the phase matching condition, $J_0(2A_0) = 0$, we have further set $p = 4\,m$ and $A_0 = 2.75$. While the SIRF oscillates periodically with L for all values of ϵ, as ϵ increases, the oscillation amplitude decreases, leading to larger PMD reduction factors. As expected, the curve for $\epsilon = 0.01$ nearly overlaps that for a PM fiber, while the SIRF is less periodic for $\epsilon = 0.90$, as previously observed from the RMM calculations [65].

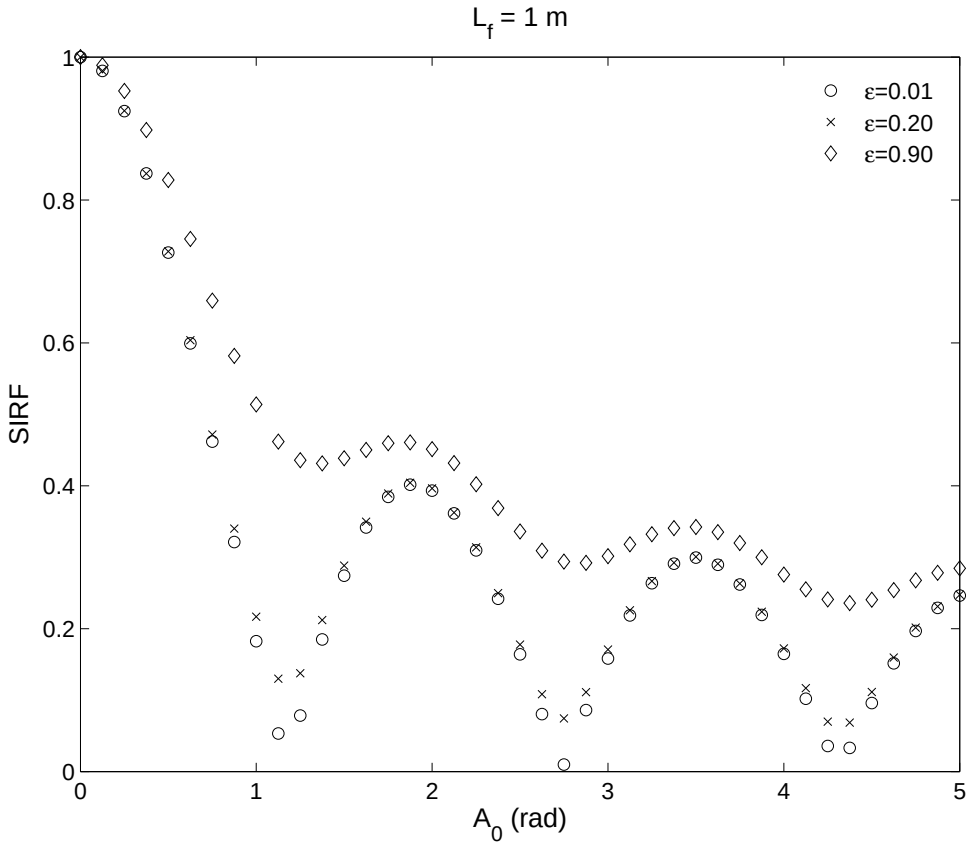

Figure 4.4: The SIRF as a function of spin amplitude A_0 for $0 < A_0 < 5\,rad$ with $L_f = 1\,m$. Here the spin period $p = 4\,m$, while $\Lambda_{beat} = 20\,m$ and $\epsilon = 0.01$ $\circ$, $\epsilon = 0.20$ $\times$, and $\epsilon = 0.90$ $\diamond$.

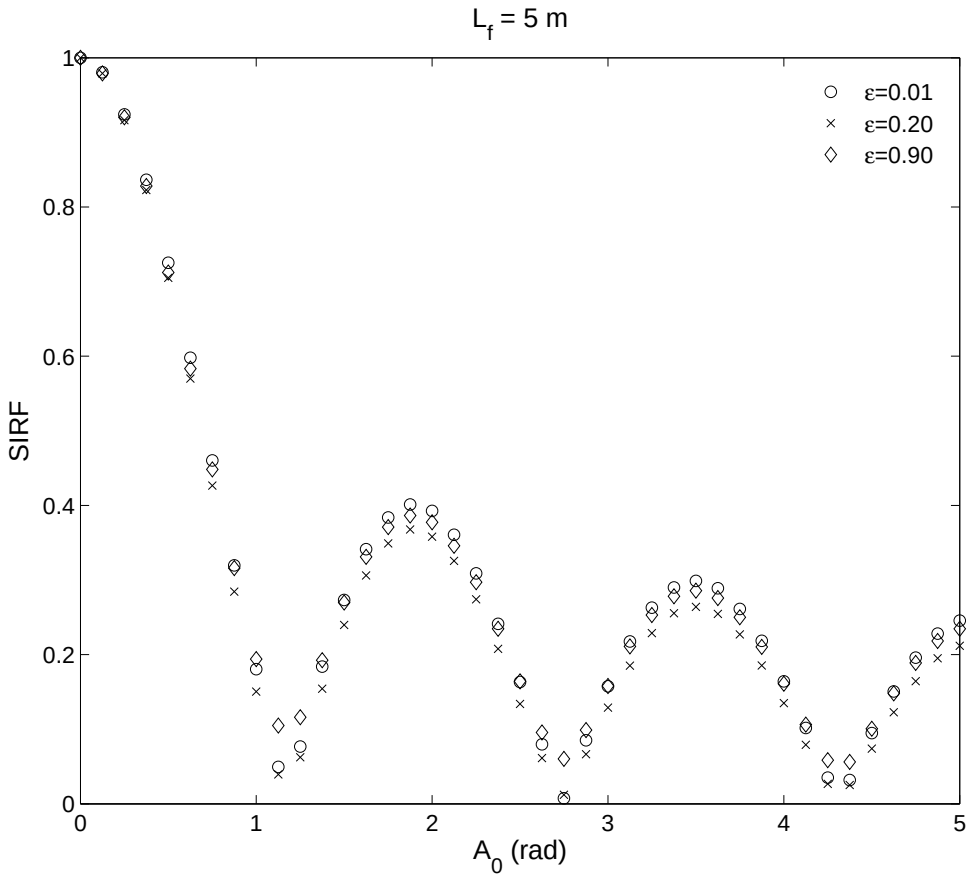

Figure 4.5: As in Fig. 4.4 but for $L_f = 5\,m$

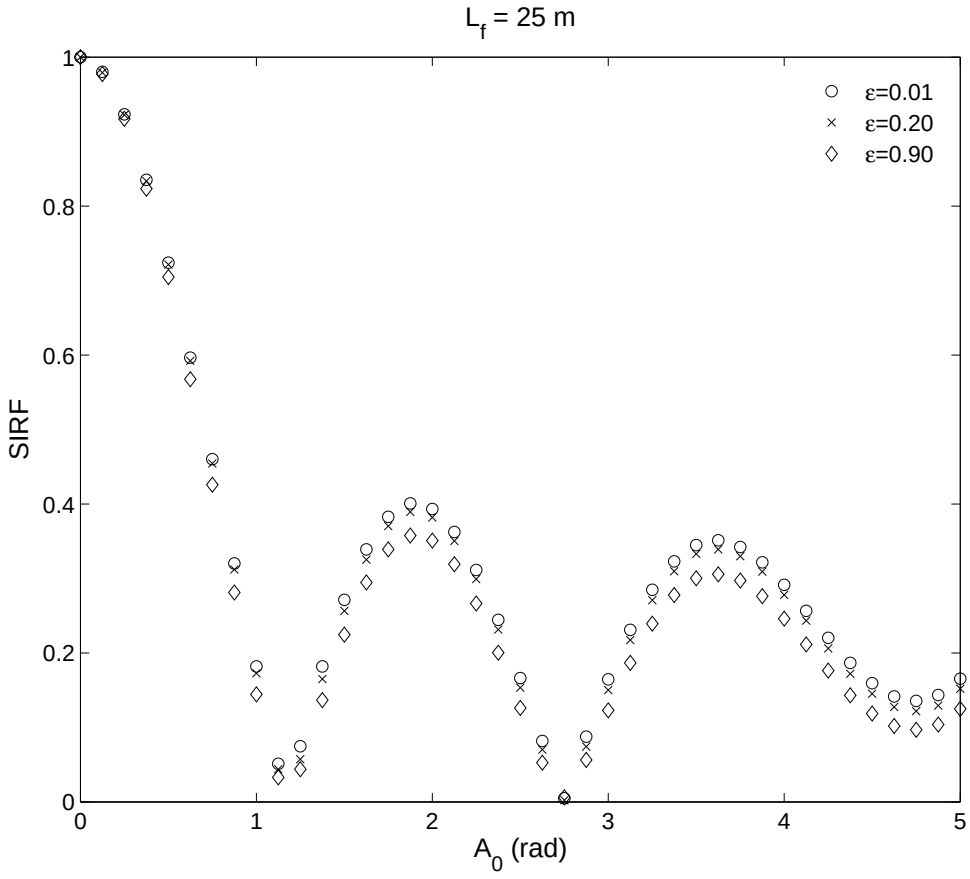

Figure 4.6: As in Fig. 4.4 but for $L_f = 25\,m$

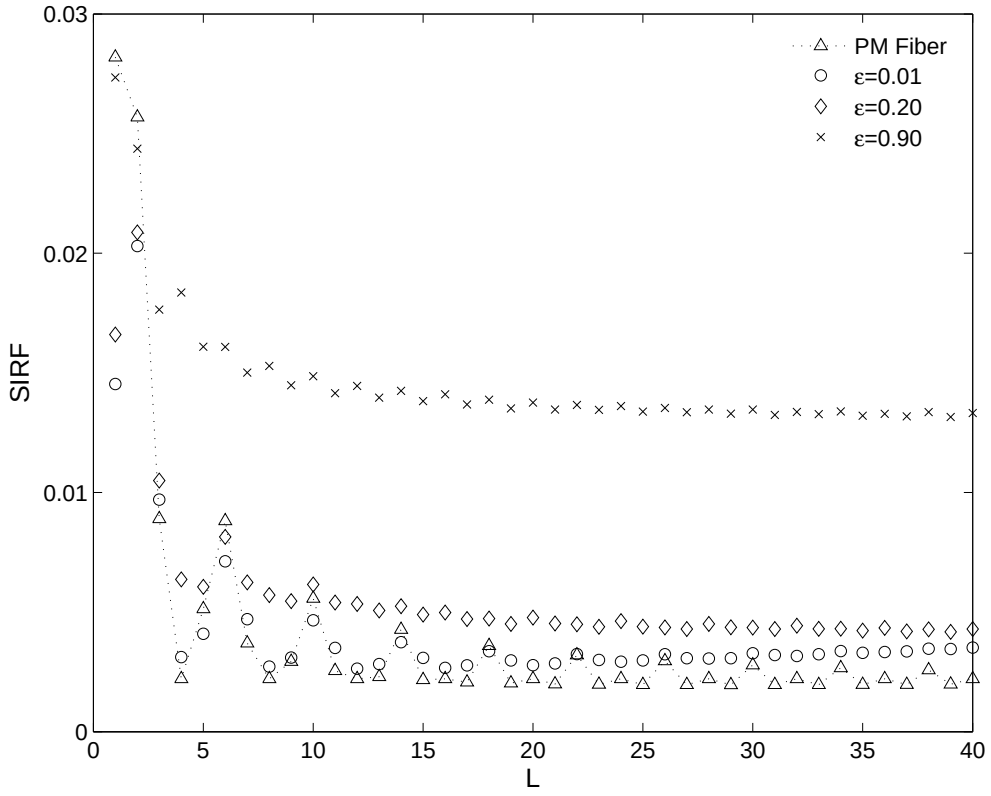

Figure 4.7: The SIRF as a function of fiber length L. Here the spin period $p = 4\,m$ and amplitude $A_0 = 2.75\,rad$, while $\Lambda_{beat} = 20\,m$ and $L_f = 15\,m$. The curves marked $\circ$, $\diamond$, $\times$ and $\triangle$ correspond to $\epsilon = 0.01$, $\epsilon = 0.20$, $\epsilon = 0.90$ and PM fiber, respectively.

A central result of this section is that the MRMM predicts that the PMD reduction for sinusoidal spun fibers varies with the form of the birefringence profiles, such that as the random fluctuation strength ϵ is varied from 0 to 1, the behavior of the SIRF as a function of fiber parameters and spin amplitude interpolates between that of PM fiber and the RMM predictions, c. f. Fig. 4.1 - 4.7

We finally investigate the pdf of the DGD of sinusoidally spun fibers as a function of fiber length. This study parallels our previous analysis of standard fibers in Chapter 3. Since the pdf of the DGD approaches the Maxwell distribution for long fiber lengths, we plot the variance of the deviation of the computed pdf distributions $\rho(n)$ from the Maxwell distribution $\rho_m(n)$ with the same mean DGD, namely,

$$\begin{aligned} \delta_v &= \sum_{n=0}^{M} (\rho_m(n) - \rho(n))(\tau_b^2(n) - \bar{\tau}_b^2) \\ \bar{\tau}_b &= \sum_{n=0}^{M} \rho\, \tau_b(n) \end{aligned} \tag{4.2}$$

in which $M = 40$ histogram bins are employed. The variation of δ_v as a function of $log(L)$ for sinusoidal spun fiber with spin period $p = 4\,m$ and amplitude $A_0 = 2.75$ is calculated in the presence of random birefringence described by $\Lambda_{beat} = 20\,m$, $L_f = 15\,m$, and $\epsilon = 0.9$ and $\epsilon = 0.2$. The results are compared with those of corresponding unspun fibers in Fig. 4.8 for $\epsilon = 0.9$ and Fig. 4.9 for $\epsilon = 0.2$ respectively. Since the pdf:s approach the Maxwellian distribution at different rates, we have employed $0.5 < L < 3000$ in Fig. 4.8 with $\epsilon = 0.9$, and $0.5 < L < 10000$ in Fig. 4.9 with $\epsilon = 0.2$. For comparison, Figs. 4.8 and 4.9 display the different curves plotted instead with the same length scale. In all cases, the lines marked $+$ and $\circ$ correspond to the unspun and spun fiber results, while the dotted and dashed curves are polynomial least-square fits. While the four curves for δ_v possess zero crossings at small L, this does not imply that the pdf is an exact Maxwell distribution since higher moments of the pdf:s may deviate from the Maxwellian values. In fact, graphs of the actual pdf:s display noticeable deviations from the Maxwell distribution for short fiber lengths, but approach the Maxwell distribution asymptotically as $L \to \infty$ as indicated by the solid line in Figs. 4.8 and 4.9. Further, δ_v oscillates with fiber length for spun fiber but not for unspun fiber.

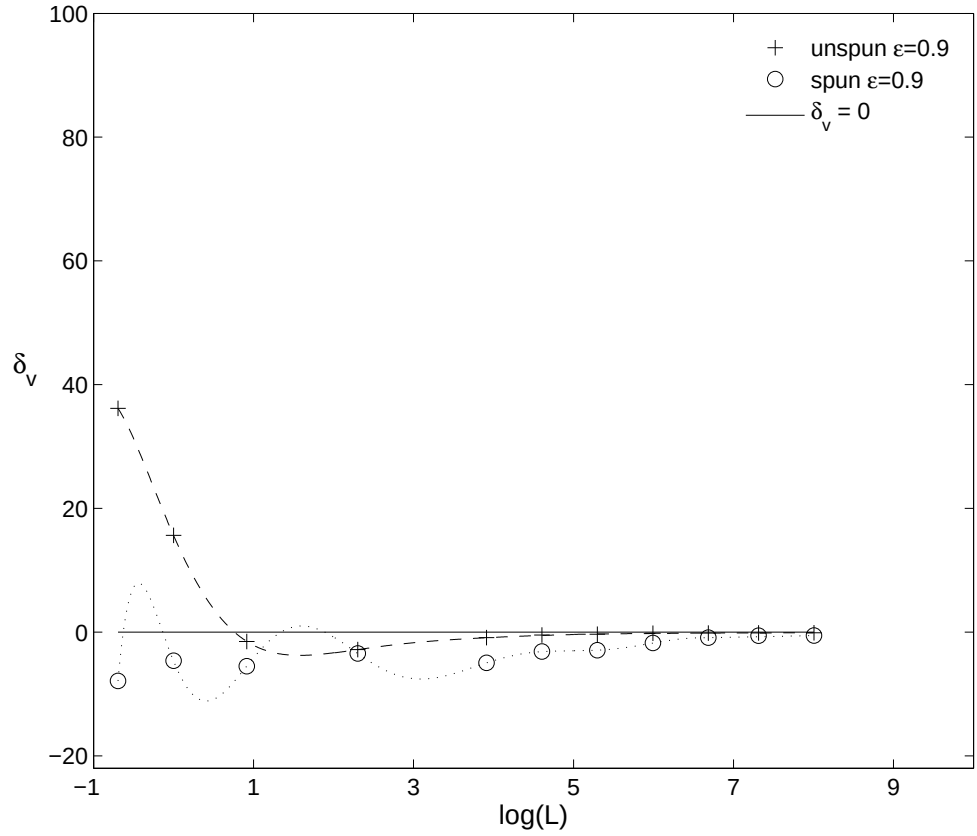

Figure 4.8: The variation of δ_v with $log(L)$ for $\epsilon = 0.90$ and L = 0.5, 1, 2.5, 10, 50, 100, 200, 400, 800, 1500, 3000. The spun fiber results with spin period $p = 4\,m$ and amplitude $A_0 = 2.75\,rad$ are compared with those of unspun fiber with $L_f = 15\,m$ and $\Lambda_{beat} = 20\,m$. $+$ and $\circ$ are the unspun and spun fiber results, and the dotted and dashed curves are polynomial least-square fits to these curves. The solid line is computed with $\delta_v = 0$.

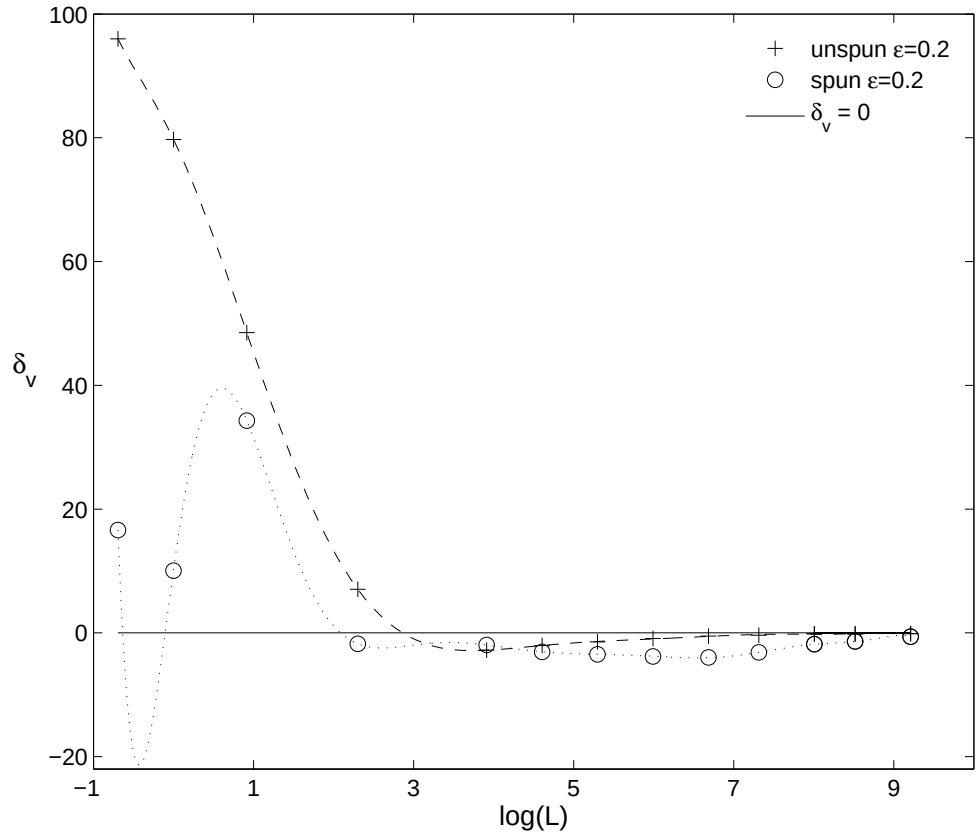

Figure 4.9: As in Fig. 4.8 but for $\epsilon = 0.20$ and L = 0.5, 1, 2.5, 10, 50, 100, 200, 400, 800, 1500, 3000, 5000, 10000.

The distance at which the pdf becomes approximately Maxwellian increases in Figs. 4.8 and 4.9 as ϵ decreases towards zero. If we define L_m as the length at which δ_v decreases to $|\delta_v| = 1$, we observe from our figures that for both ϵ values considered, L_m is proportional to the correlation length L_{corr} for both spun and unspun fibers. Thus L_m increases by a factor of five when ϵ is decreased from 0.90 to 0.20 since $L_{corr} = \nu(\epsilon)L_f$, and the ratio of ν for $\epsilon = 0.20$ and $\epsilon = 0.90$ is $\nu_{0.2}/\nu_{0.9} = 5.13$. Finally, the rate at which the pdf becomes Maxwellian is also far smaller for spun fibers compared to unspun fibers. That the pdf possesses significantly different features as a function of fiber length for spun and unspun fibers is a second central result of this section.

4.2 Polarization Mode Dispersion Compensation

For existing long haul 10 and 40 GHz optical transmission systems, considerable effort has been expended on the theoretical and experimental analysis of electrical and optical PMD compensation in the last decade [78–82]. In this section, we examine PMD compensation formalisms that replace the 2×2 transfer matrix relating the input and output polarization vectors of an arbitrary optical element with products of exponentials of individual matrices. In our first Taylor-series methods, which extend the procedures of Refs. [83] and [1], suitably symmetrized exponential products are employed to enhance computational accuracy at a given order. Up to second order, the physical process corresponding to each individual exponential operator has been experimentally realized [84], and the third-order operator could be implemented in a manner similar to that of Ref. [85] (note, however, that if the bandwidth of the incoming pulse is small, any fiber behaves as a first-order element, for which simplified optical and electrical techniques are available [81]).

Since the Taylor procedure does not successfully compensate the PMD of large-bandwidth signals, other authors have expanded the transfer matrix in a Fourier series [86] or applied an iterative least-squares fit to minimize the calculated deviation of the PMD over a given frequency interval from experimental measurements [87]. In this section, we instead describe the PMD behavior of each fiber realization in

terms of modified exponential products derived from a Chebyshev polynomial approximation to the observed PMD [88]. Similar to the Taylor expansion procedure, we also employ a proper symmetrization of the noncommuting matrix operators to ensure a large Chebyshev compensation bandwidth.

This work was performed in collaboration with other students and my thesis advisor. My contribution consisted of co-developing the theory and independently programming numerical implementations.

4.2.1 Taylor Series Approximation

In this subsection, we introduce procedures that lead to improved accuracy or bandwidth compared to the results of Ref. [1] through the inclusion of additional compensator stages.

Polarization evolution in a linear optical fiber medium in the Jones representation is described by a complex 2×2 frequency-dependent transfer matrix $T(\omega)$ according to $\mathbf{E}_{out} = T(\omega)\mathbf{E}_{in}$, where $\mathbf{E}_{in}$ and $\mathbf{E}_{out}$ denote the incoming and outgoing optical field polarizations, respectively. PMD is then characterized through a three-dimensional Stokes space PMD vector $\boldsymbol{\tau}$ which can be obtained from

$$D(\omega) \equiv -\frac{1}{2}\boldsymbol{\tau} \cdot \boldsymbol{\sigma} = \frac{dT}{d\omega}T^{-1}(\omega), \tag{4.3}$$

in which $\boldsymbol{\sigma}$ represents the Pauli spin vector. Once the analytical expansion of $T(\omega)$ has been found, PMD compensation (PMDC) can be accomplished by implementing the inverse of the approximate $T(\omega)$ after the fiber system [1, 84, 89].

In Ref. [1], $T(\omega)$ is expanded in the vicinity of a reference frequency ω_0 as a product of exponentials of increasing powers of the frequency deviation according to

$$T(\omega_0 + \Delta\omega) = T(\omega_0)e^{\Delta\omega N_1}e^{\frac{1}{2!}(\Delta\omega)^2 N_2}e^{\frac{1}{3!}(\Delta\omega)^3 N_3}e^{\frac{1}{4!}(\Delta\omega)^4 N_4}\cdots . \tag{4.4}$$

From Eq. (4.4), the matrices N_i can be expressed as

$$N_1 = \frac{dT}{d\omega}|_{\omega_0} T_0^{-1} \tag{4.5}$$

$$N_2 = \frac{d^2T}{d\omega^2}|_{\omega_0} T_0^{-1} - N_1^2 \tag{4.6}$$

$$N_3 = \frac{d^3T}{d\omega^3}|_{\omega_0} T_0^{-1} - 3N_1N_2 + N_1^3 \tag{4.7}$$

$$N_4 = \frac{d^4T}{d\omega^4}|_{\omega_0} T_0^{-1} - 4N_1N_3 - 6N_1^2N_2 - 3N_2^2 - N_1^4. \tag{4.8}$$

The exponential expansion according to Eq. (4.4) has the advantage that different orders of PMD can be treated as separate subsystems and subsequently concatenated. However, this expansion is not necessarily optimal, as it ignores the non-commutativity of the matrix product.

Alternative procedures can be obtained through other forms of the solution of the underlying differential equation

$$\frac{dT}{d\omega} = D(\omega)T(\omega). \tag{4.9}$$

For example, to express the solution of this equation as a single exponential of a Taylor series, we can expand

$$D(\omega) = \sum_{n=0}^{\infty} \frac{D_{n+1}}{n!}\Delta\omega^n \tag{4.10}$$

in which D_{n+1} denotes the nth derivative of $D(\omega)$ with respect to frequency.

To express the solution of Eq. (4.9) in the form

$$T(\omega) = T(\omega_0)e^{S_1\Delta\omega + \frac{S_2}{2!}\Delta\omega^2 + \frac{S_3}{3!}\Delta\omega^3 + \cdots}, \tag{4.11}$$

we equate the expressions for $\frac{dT}{d\omega}|_{\omega_0}$, $\frac{d^2T}{d\omega^2}|_{\omega_0}$, $\frac{d^3T}{d\omega^3}|_{\omega_0} \cdots$, evaluated by using Eq. (4.9), with the corresponding expressions obtained from Eq. (4.11). We find that

$$\begin{aligned}
\frac{dT}{d\omega}|_{\omega_0} &= D_1 = S_1 \\
\frac{d^2T}{d\omega^2}|_{\omega_0} &= D_2 + D_1D_1 = S_2 + S_1S_1 \\
\frac{d^3T}{d\omega^3}|_{\omega_0} &= D_3 + 2D_2D_1 + D_1D_2 + D_1D_1D_1 \\
&= S_3 + 1.5S_2S_1 + 1.5S_1S_2 + S_1S_1S_1,
\end{aligned} \tag{4.12}$$

so that

$$S_1 = D_1 \tag{4.13}$$
$$S_2 = D_2 \tag{4.14}$$
$$S_3 = D_3 + \frac{1}{2}[D_2, D_1], \tag{4.15}$$

or

$$S_1 = N_1 \tag{4.16}$$
$$S_2 = N_2 \tag{4.17}$$
$$S_3 = N_3 + \frac{3}{2}[N_1, N_2] \tag{4.18}$$
$$S_4 = N_4 + [N_3, N_1], \tag{4.19}$$

where $[A, B]$ denotes the commutator of A and B.

We observe that while the first two characteristic matrices S_1 and S_2 equal the corresponding matrices of Eyal's method, matrices of higher orders such as S_3 and S_4 differ from those of Eyal's method due to non-commutativity of these matrices, which was neglected by Eyal etc.

To further break Eq. (4.11) into products of individual exponential operators, we employ the standard formula [90, 91],

$$e^{x(A+B)} = e^{\frac{A}{2}x}\, e^{Bx}\, e^{\frac{A}{2}x} + O(x^3), \tag{4.20}$$

which yields

$$T(\omega) = T(\omega_0) e^{\frac{S_1}{2}\Delta\omega} e^{\frac{S_2}{2}\Delta\omega^2} e^{\frac{S_1}{2}\Delta\omega} + O(\Delta\omega^3), \tag{4.21}$$

with obvious higher-order extensions according to Ref. [90]. Hence, unlike, e.g., the compensator proposed in Ref. [84], which does not incorporate the commutator appearing in S_3, residual PMD effects up to second order can be fully eliminated by implementing the expression:

$$T_{res}(\omega) = e^{-\frac{S_1}{2}\Delta\omega} e^{-\frac{S_2}{2}\Delta\omega^2} e^{-\frac{S_1}{2}\Delta\omega} T^{-1}(\omega_0) T(\omega). \tag{4.22}$$

4.2.2 Chebyshev Polynomial Approximation

An alternative technique evaluates the transfer matrix $T(\omega)$ using type I Chebyshev polynomials [88] scaled to the interval $|\omega - \omega_0| < \Delta\omega_c$, where $\Delta\omega_c$ represents the desired bandwidth on the interval of interest. In particular, we express the transfer matrix in the form

$$\begin{aligned} T(\omega) &= e^{F(\omega)} \\ &= e^{F_0+F_1\Delta\omega+F_2\Delta\omega^2+F_3\Delta\omega^3+\cdots}, \end{aligned} \tag{4.23}$$

in which the matrix $F(\omega) \equiv ln[T(\omega)]$ is approximated with (M-1)th-order Chebyshev polynomials (an expansion into the first M Chebyshev polynomials) [92]. Specifically, we first approximate the components of $F(\omega)$, $f^i(\omega)$ for $i = 1, 2, 3, 4$, according to the standard polynomial approximation formula,

$$f(x) \approx \sum_{k=0}^{M-1} c_k \cdot P_k(x) - \frac{1}{2}c_0, \tag{4.24}$$

with $x \in [-1, 1]$. In Eq. (4.24), $P_k(x)$ is the Chebyshev polynomial of order k, and c_k is the corresponding coefficient,

$$c_k = \frac{2}{M} \cdot \sum_{j=1}^{M} f(x_j) \cdot \cos\left[\frac{\pi k(j-0.5)}{M}\right], \tag{4.25}$$

with

$$x_j = \cos\left[\frac{\pi(j-0.5)}{M}\right]. \tag{4.26}$$

Scaling $f(x)$ according to $x = 2\Delta\omega/\Delta\omega_c$ yields

$$f^i(\omega) = f_0^i + f_1^i\Delta\omega + f_2^i\Delta\omega^2 + f_3^i\Delta\omega^3 + \cdots, \tag{4.27}$$

and hence

$$F_n = \begin{bmatrix} f_n^1 & f_n^3 \\ f_n^3 & f_n^4 \end{bmatrix}, \tag{4.28}$$

with $n = 0, 1, 2, 3, \cdots$.

As in the Taylor approximation procedure, Eq. (4.23) can be further approximated as the product of exponents of individual operators through operator symmetrization formulas according to Eq. (4.20). Applying the simplest three-operator expansion yields

$$T_{res}(\omega) = e^{-\frac{F_1}{2}\Delta\omega} e^{-\frac{F_2}{2}\Delta\omega^2} e^{-\frac{F_1}{2}\Delta\omega} T^{-1}(\omega_0) T(\omega). \tag{4.29}$$

The Chebyshev polynomial approximation of the transfer matrix described above follows a different procedure from the co-authored paper [93]. Nevertheless, the numerical simulation yields similar results, c.f. section 4.2.3 and Ref. [93].

4.2.3 Numerical Results

We now examine numerically the compensation error associated with the operator expansions above and effect a comparison with the approach of Ref. [1]. To quantify the error, we observe that, since in the absence of loss the transfer matrix after compensation, $T_{res}(\omega)$, is a 2×2 unitary matrix, its eigenvalues form complex conjugate pairs. The magnitude of their difference therefore describes the deviation of the matrix from an identity matrix representing a perfect compensator. Further, since diagonalization is equivalent to reorienting the measuring apparatus to the principal states of polarization, the eigenvalue difference coincides with $2\sin(\Delta\omega\tau_{res}/2)$, where τ_{res} is the residual DGD. Hence, we define residual as the absolute difference between the two eigenvalues of the residual matrix $T_{res}(\omega)$. The residuals after a standard compensator based on the three procedures have been calculated as a function of a normalized frequency $\Delta\nu = \Delta\omega\,\bar{\tau}/(2\pi)$. In these calculations, we employ $\bar{\tau} = 30\,ps$, and $\Delta\omega \in [-2\pi/\bar{\tau}, -2\pi/\bar{\tau}]$ or $\Delta\nu \in [-1, 1]$. The results are averaged by 10^4 realizations.

To calculate the Jones matrix $T(\omega)$ of an optical fiber, we consider the fiber as N linearly birefringent sections with random orientations. Thus,

$$T(\omega) = \prod_{n=1}^{N} T_n(\omega) \tag{4.30}$$

where $T_n(\omega)$ is the transfer matrix of the n-th fiber section and is calculated according to

$$T_n(\omega) = P(\omega)\, S_n \tag{4.31}$$

with

$$P(\omega) = \begin{bmatrix} e^{-\frac{i\omega\tau_s}{2}} & 0 \\ 0 & e^{\frac{i\omega\tau_s}{2}} \end{bmatrix} \tag{4.32}$$

and

$$S_n = \begin{bmatrix} \cos(\frac{\xi_n}{2})\, e^{i\frac{\varphi_n+\phi_n}{2}} & i\, sin(\frac{\xi_n}{2})\, e^{i\frac{\varphi_n-\phi_n}{2}} \\ i\, \sin(\frac{\xi_n}{2})\, e^{-i\frac{\varphi_n-\phi_n}{2}} & \cos(\frac{\xi_n}{2})\, e^{-i\frac{\varphi_n+\phi_n}{2}} \end{bmatrix}. \tag{4.33}$$

In Eq. (4.32), $\tau_s = \sqrt{3\pi/8}\,\bar{\tau}$ is section DGD and $\bar{\tau}$ is the mean DGD of the fiber. The angles ξ_n, φ_n and ϕ_n in Eq. (4.33) are independent random variables. The probability density function (pdf) of ξ_n, φ_n are uniformly distributed between 0 and 2π, while the pdf of $\cos(\xi_n)$ is uniformly distributed between -1 and 1.

We first display Fig. 4.10 (a) and (b) histograms of the residuals for (a) asymmetric compensation of Ref. [1] according to Eq. (4.4) and (b) Taylor expansion with symmetrized exponential product approximations according to Eq. (4.21), respectively. In these graphs, the results of first- to third-order compensations are superimposed as indicated by the legend. Evidently, symmetrizing the exponential product yields an improvement in the bandwidth at the cost of introducing an additional operator (compensator element).

Next, in Fig. 4.10 (c) we display histograms of the residuals for the symmetrized operator products associated with the first- to third-order Chebyshev procedures of Eq. (4.24). In this calculation, a Chebyshev polynomial approximation is performed over the frequency interval $|\omega - \omega_0| < M\Delta\omega_1$ given by $2\pi\Delta\omega_1 = \Delta\nu_c/\bar{\tau}$ with $\Delta\nu_c = 0.07$ [93]. Note that only odd-order Chebyshev polynomial expansions possess zero residuals at the center frequency, since the Chebyshev approximation then exactly coincides with the transfer matrix at the zero of the subsequent even-ordered Chebyshev polynomials, one of which lies in the origin.

Although the residuals in Fig. 4.10 (c) are far larger than those of Tayler-series methods near the origin, c.f. Fig. 4.10 (a) and (b), the residual is suppressed over a broader frequency domain for the Chebyshev compensator. In fact, the bandwidth

measure, $2\pi\Delta\omega_1 = \Delta\nu_c/\bar{\tau}$, employed in Fig. 4.10 (c) and Fig. 4.11 (b) is valid only if the DGD of the fiber realization is, on average, less than or equal to the average DGD [81]. Although most statistical realizations of the fiber obey this rule, a significant fraction does not, leading to rapidly oscillating transfer matrices $T(\omega)$. The accuracy of the Chebyshev fit is therefore degraded, increasing the corresponding residual values. This yields the local maxima near the center of the graph of Fig. 4.10 (c), which reflect the contributions from all fiber samples.

To further demonstrate the advantage of Chebyshev approximation over Taylor approximation, we display in Fig. 4.11 the histograms of the residuals when Eq. (4.11) and Eq. (4.23) are employed directly without further breaking into products of individual exponential operators for (a) Taylor approximation and (b) Chebyshev approximation, respectively. While, the bandwidth of Taylor compensator increases noticably with the order only up to the third order, the compensation bandwidth associated with Chebyshev approximation increases more significantly with the order and nearly linearly up to the fourth order, c.f. Fig. 4.11.

4.3 Conclusions

In this chapter, we first examined the statistics of the DGD in sinusoidally spun fibers with a general model of fiber birefringence. We find that the PMD reduction effect induced by sinusoidal spinning can be suppressed by a factor of over 10, which agrees very well with the experimental measurements [68, 69]. Further, the simulation results show that the PMD reduction effect is more significant in fibers with large random birefringence. Moreover, our results of the PMD reduction factor interpolate between the predictions of the PM fiber and those of the RMM and therefore display somewhat different features than those of previous authors. The pdf of sinusoidally spun fibers also differs markedly from that of standard fibers at shorter fiber lengths, although it still asymptotically approaches the Maxwell distribution at very long fiber lengths. Such a qualitative understanding of birefringence effects could enable the partial determination of the fiber birefringence from repeated experimental measurements as well as provide insight into the range of parameters required to achieve near-optimal DGD compensation in smaller

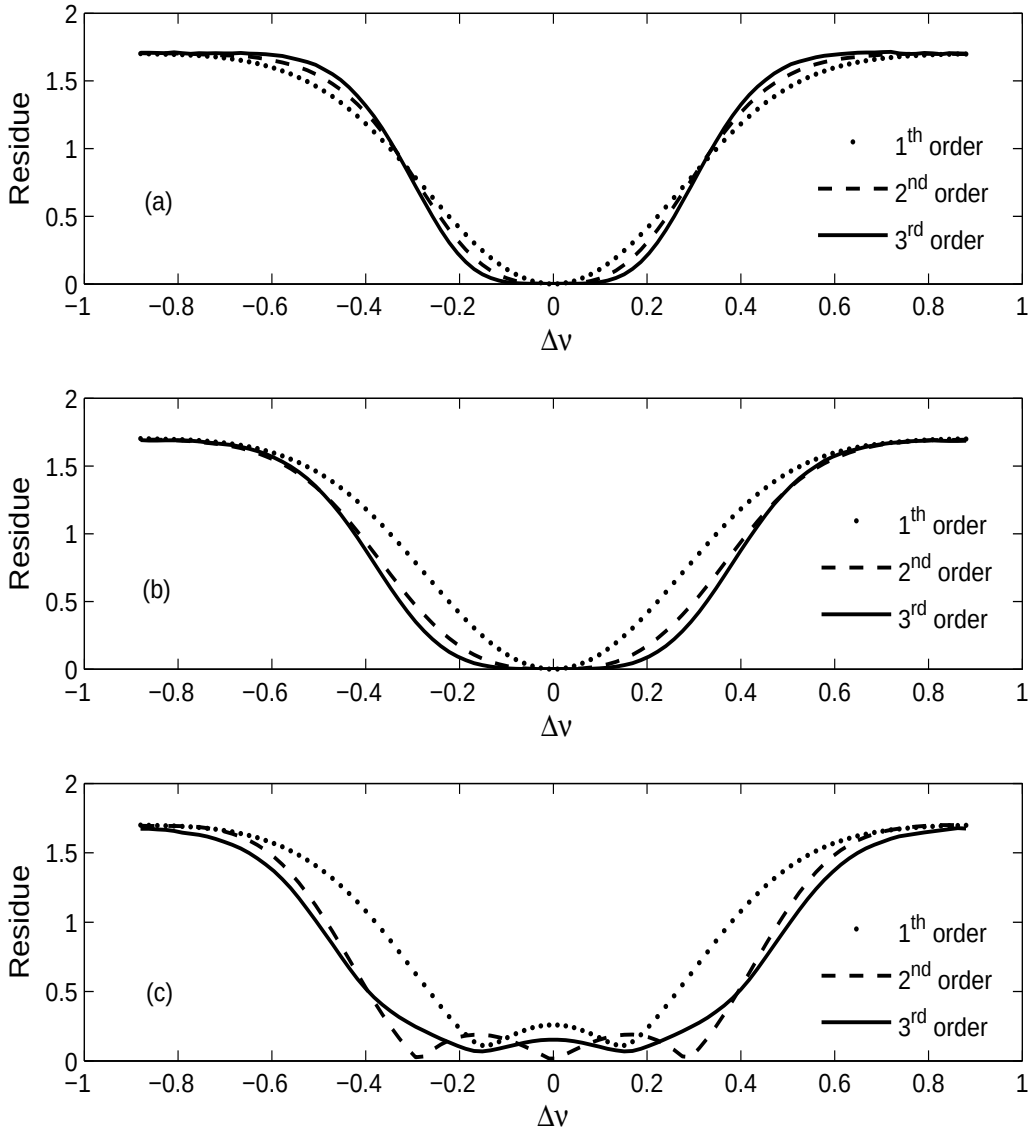

Figure 4.10: Variation of the residual with the normalized parameter $\Delta\nu$ after the first- to third-order (a) asymmetric compensation of Ref. [1], (b) Taylor approximation with appropriate symmetrization of the operator products, and (c) Chebyshev approximation with appropriate symmetrization of the operator products. The results are averaged with 10^4 realizations with $\bar{\tau} = 30\,ps$.

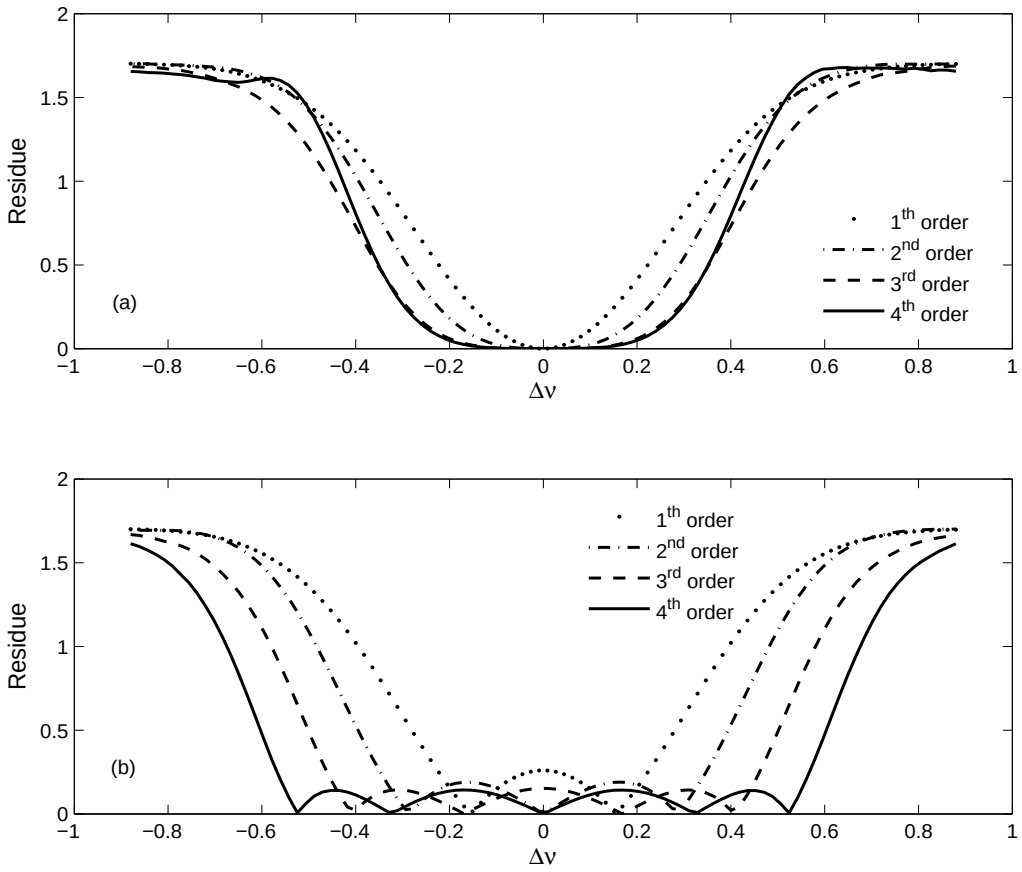

Figure 4.11: Variation of the residual with the normalized parameter $\Delta\nu$ after the first- to third-order for (a) Taylor approximation according to Eq. (4.11) and and (b) Chebyshev approximation according to Eq. (4.23), without further breaking into products of individual exponential operators.

fiber lengths. We then presented two general procedures for enhancing the effective bandwidth of PMD compensators. While the residual PMD of a compensator resulting from a Taylor expansion can be significantly reduced by appropriate symmetrization of the operator products, the Chebyshev approximation can, at least in principle, significantly widen the compensator bandwidth.

Chapter 5

Nonlinear Polarization Mode Dispersion

5.1 Introduction

Although glass fiber is a highly linear material, it has a non-zero nonlinear refractive index due to the Kerr effect [94–96]. With the advent of the erbium-doped optical amplifier, light signals can be transmitted through fibers over transoceanic distance without regeneration. However, both polarization mode dispersion (PMD) and nonlinearities accumulate over the entire distance, resulting in a non-negligible pulse distortion for high bit rate communication systems [97]. Moreover, the interaction between fiber birefringence and nonlinearity may lead to further complications [98–100].

While PMD has been extensively studied in the linear region based on various birefringence models, the properties of PMD in the presence of fiber nonlinearity requires more investigation. In previous work, Menyuk showed that the coupled nonlinear Schrödinger equation (CNLS) applies to birefringent optical fiber [44,101, 102]. Later on, Marcuse derived the Manakov-PMD equation [40]. This equation not only leads to a rapid numerical scheme for determining the signal evolution, but also isolates different physical effects in separate terms of the equation that

have transparent physical meanings. Using this equation as a starting point, signal propagation in nonlinear birefringent optical fibers was investigated in [40].

For numerical simulations of pulse propagation in the presence of both fiber birefringence and nonlinearity, appropriate fiber birefringence models are essential. While different birefringence models predict distinct stochastic properties of linear PMD, c.f. Chapter 3, early studies of PMD and nonlinearity either assumed constant birefringence [101,103,104] or employed a simple birefringence model, i.e., the fixed modulus model (FMM) [105–107]. In this chapter, we study nonlinear pulse propagation properties based on a modified random modulus model (MRMM), i.e. Model B1 in Chapter 2. Since the Manakov-PMD equation is the basic governing equation for pulse propagation in nonlinear birefringent fibers, section 5.2 briefly reviews the derivation of this equation for completeness. We then discuss in the next section the numerical simulations of pulse distortion due to linear and nonlinear PMD. The last section contains the conclusion.

5.2 Derivation of The Manakov-PMD Equation

In this section, we review the derivation of the Manakov-PMD equation according to [40].

Optical signals in fibers can be distorted by several effects. Firstly, the signals suffer the usual polarization mode dispersion for a non-zero b'. Secondly, the signals undergo chromatic dispersion if $\beta'' \neq 0$ (we assume that $\beta_1'' \approx \beta_2'' = \beta''$). Finally, the weak nonlinearity of optical fibers yields a dependence of the refractive index on the light intensity. Taking all these effects into account, the propagation of the light pulses along a random birefringent fiber can be described by the coupled nonlinear Schrödinger equation,

$$\begin{aligned} & i\frac{\partial \mathbf{A}}{\partial z} + b\Sigma\mathbf{A} + ib'\Sigma\frac{\partial \mathbf{A}}{\partial z} - \frac{1}{2}\beta''\frac{\partial^2 \mathbf{A}}{\partial t^2} \\ & + n_2 k_0 \left[|\mathbf{A}|^2\mathbf{A} - \frac{1}{3}(\mathbf{A}^\dagger\sigma_2\mathbf{A})\sigma_2\mathbf{A} \right] = 0. \end{aligned} \tag{5.1}$$

Here, $\mathbf{A} = (A_1, A_2)^t$ is a column vector with elements A_1 and A_2 which are the complex envelopes of the two polarization components. The z-coordinate measures

distance along the fiber axis, while the t-coordinate represents retarded time - the time relative to the moving center of the signal. The last term of Eq. (5.1) corresponds to nonlinear effects caused by the Kerr coefficient n_2, c.f. Eq. (1.2) in Chapter 1. The matrix

$$\Sigma = \sigma_3 \cos(2\alpha) + \sigma_1 \sin(2\alpha) \tag{5.2}$$

is defined in terms of the Pauli matrices

$$\begin{aligned} \mathbf{I} &= \begin{bmatrix} 1 & 0 \\ 0 & 1 \end{bmatrix}, \quad \sigma_1 = \begin{bmatrix} 0 & 1 \\ 1 & 0 \end{bmatrix} \\ \sigma_2 &= \begin{bmatrix} 0 & -i \\ i & 0 \end{bmatrix}, \quad \sigma_3 = \begin{bmatrix} 1 & 0 \\ 0 & -1 \end{bmatrix}. \end{aligned} \tag{5.3}$$

While b is the birefringence strength which varies randomly along the fiber length according to the birefringence model MRMM, the orientation of the principal birefringence axis relative to the laboratory frame, α, is assumed to be only a weak function of frequency. The birefringence orientation was denoted as $\theta = 2\alpha$ in previous chapters.

To obtain the Manakov-PMD equation, two separate steps are required. Firstly, the field $\mathbf{A}$ is transformed from the fixed coordinate system to a coordinate system that rotates with the principal axes of the fiber. The new field is designated by the vector $\mathbf{\Psi} = [U, V]^t$ that is related to $\mathbf{A}$ as follows:

$$\begin{aligned} \mathbf{\Psi} &= R^{-1}\mathbf{A} \\ &= \begin{bmatrix} \cos(\alpha) & \sin(\alpha) \\ -\sin(\alpha) & \cos(\alpha) \end{bmatrix} \begin{bmatrix} A_1 \\ A_2 \end{bmatrix} \end{aligned} \tag{5.4}$$

Secondly, for fast numerical computation, the vector $\mathbf{\Psi}$ is further transformed to a new field vector $\bar{\mathbf{\Psi}}(z,t) = [\bar{U}, \bar{V}]^t$ via a unitary matrix $T(z)$, i.e.,

$$\mathbf{\Psi}(z,t) = \mathbf{T}(z)\bar{\mathbf{\Psi}}(z,t). \tag{5.5}$$

$\mathbf{T}$ is the solution to the ordinary differential equation

$$i\frac{\partial \mathbf{T}}{\partial z} + \tilde{\Sigma}\mathbf{T} = 0 \tag{5.6}$$

with the initial condition

$$\mathbf{T}(z=0) \equiv \begin{bmatrix} 1 & 0 \\ 0 & 1 \end{bmatrix}. \tag{5.7}$$

$\tilde{\Sigma}$ in Eq. (5.6) can be expressed as

$$\tilde{\Sigma} = \begin{bmatrix} b & -i\alpha_z \\ i\alpha_z & -b \end{bmatrix} \tag{5.8}$$

where $\alpha_z = d\alpha/dz$, and the matrix $\mathbf{T}$ is a special unitary matrix so that it has the form

$$\mathbf{T}(z) \equiv \begin{bmatrix} u_1 & -u_2* \\ u_2 & u_1* \end{bmatrix}, \tag{5.9}$$

with the additional constraint $|u_1|^2 + |u_2|^2 = 1$.

According to Eq. (5.4) and Eq. (5.5), the vectors $\mathbf{A}$ and $\bar{\mathbf{\Psi}}$ are related to one and another by a simple unitary transformation. Since the electrical output current from a realistic detection system is given by $|\mathbf{A}|^2 = |\bar{\mathbf{\Psi}}|^2$, either vector can be employed to describe the electric field. In fact, after these transformations, the coupled nonlinear Schrödinger equation, Eq. (5.1), yields $\partial\bar{\mathbf{\Psi}}(z,t)/\partial z = 0$ in the linear continuous wave (CW) limit. In other words, $\bar{\mathbf{\Psi}}$ is frozen on the *Poincaré* sphere in this limit, and for present communication systems with nonlinear optical pulses, its evolution is still quite slowly varying on the length scale of hundreds of kilometers that is associated with the scale lengths of PMD, chromatic dispersion, and nonlinearity. The slow variation of $\bar{\mathbf{\Psi}}$ enables integration of the resulting equation with a larger step size, greatly increasing the computation speed.

Substituting theses transformations into Eq. (5.1) yields the Manakov-PMD equation

$$\begin{aligned} & i\frac{\partial\bar{\mathbf{\Psi}}}{\partial z} - \frac{1}{2}\beta''\frac{\partial^2\bar{\mathbf{\Psi}}}{\partial t^2} + \frac{8}{9}n_2k_0|\bar{\mathbf{\Psi}}|^2\bar{\mathbf{\Psi}} \\ = \; & -ib'\bar{\sigma}\frac{\partial\bar{\mathbf{\Psi}}}{\partial t} - \frac{1}{3}n_2k_0(\hat{\mathbf{N}} - \langle\hat{\mathbf{N}}\rangle). \end{aligned} \tag{5.10}$$

The second term on the left-hand side of Eq. (5.10) includes the effect of chromatic dispersion, and the third term on the left-hand side of Eq. (5.10) incorporates the effect of Kerr nonlinearity averaged over the *Poincaré* sphere with the 8/9 factor.

It has been shown that the first term on the right-hand side of Eq. (5.10) gives rise to linear PMD effects. Finally, the second term on the right-hand side of Eq. (5.10) yields nonlinear PMD. Physically, it is due to incomplete mixing on the *Poincaré* sphere, and was found to be negligible in the parameter regime in which current communication fibers normally operate. When the right-hand side vanishes, Eq. (5.10) reduces to the Manakov equation.

While $\bar{\sigma} = \mathbf{T}^{\dagger}\sigma_3\mathbf{T}$, one can show that $\hat{\mathbf{N}} = [\hat{N}_1, \hat{N}_2]^t$ and $\langle\hat{\mathbf{N}}\rangle = [\langle\hat{N}_1\rangle, \langle\hat{N}_2\rangle]^t$, where

$$\begin{aligned}
\hat{N}_1 &= z_1^2(2|\bar{V}|^2 - |\bar{U}|^2)\bar{U} - z_1(z_2 - iz_3)(2|\bar{U}|^2 - |\bar{V}|^2)\bar{V} \\
&- z_1(z_2 + iz_3)\bar{U}^2\bar{V}^* - (z_2 - iz_3)^2\bar{V}^2\bar{U}^* \\
\hat{N}_2 &= z_1^2(2|\bar{U}|^2 - |\bar{V}|^2)\bar{V} - z_1(z_2 + iz_3)(2|\bar{V}|^2 - |\bar{U}|^2)\bar{U} \\
&- z_1(z_2 - iz_3)\bar{V}^2\bar{U}^* - (z_2 + iz_3)^2\bar{U}^2\bar{V}^*,
\end{aligned} \tag{5.11}$$

and

$$\begin{aligned}
\langle\hat{N}_1\rangle &= \frac{1}{3}(2|\bar{V}|^2 - |\bar{U}|^2)\bar{U}, \\
\langle\hat{N}_2\rangle &= \frac{1}{3}(2|\bar{U}|^2 - |\bar{V}|^2)\bar{V},
\end{aligned} \tag{5.12}$$

with z_1, z_2 and z_3 the Stokes parameters of the CW wave, defined as

$$\begin{aligned}
z_1 &= i(u_1u_2^* - u_1^*u_2) \\
z_2 + iz_3 &= i(u_1^2 + u_2^2).
\end{aligned} \tag{5.13}$$

5.3 Numerical Results

In this section, we employ a more general model, namely the MRMM or Model B1 in Chapter 2, to examine the distortion of a pulse that propagates through a nonlinear birefringent fiber. Specifically, we first generate a longitudinally-varying birefringence vector according to the MRMM. Then the Manakov-PMD equation is numerically integrated along this birefringent fiber, following the approach in [40].

In our calculation, we employ the following parameters: the wavelength $\lambda = 1.55\,\mu m$, the effective mode area $A_{eff} = 55\,\mu m^2$, the Kerr coefficient $n_2 = 2.6 \times$

$10^{-20}\,m^2/W$ and a total fiber length $z = 2000\,km$. Fiber loss and chromatic dispersion are not considered here for simplicity, since it can be canceled with a dispersion map [108]. As the input pulse pattern we use a 10 bit pseudorandom pulses in NRZ (nonreturn to zero) format with pulse width $25\,ps$ corresponding to a signal rate of $40\,Gb/s$. As in [40], we also use the low-pass Bessel filter to slightly round the pulse edges in order to avoid the high harmonics of its fourier transform. These pulses are shown in Fig. 5.1 in units of mW with a peak power of 10 mw.

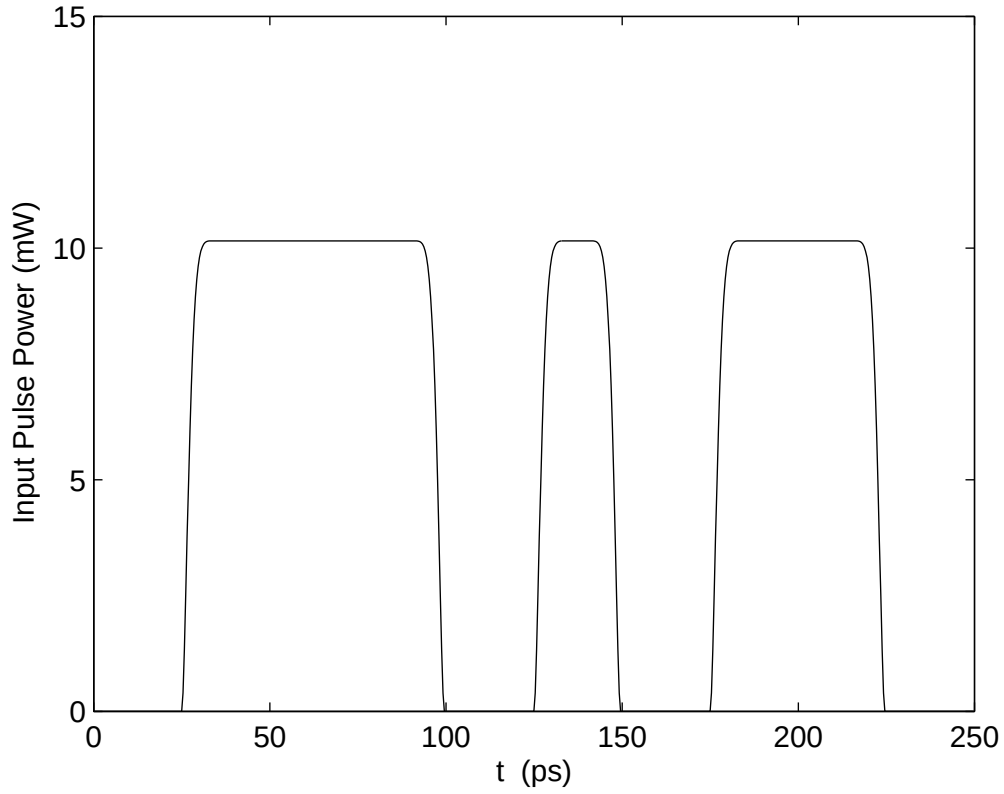

Figure 5.1: Power of the input optical pulses consisting of 10 pseudorandom bits.

According to the MRMM, the linear PMD is determined by fiber birefringence as characterized by the fiber beat length Λ_{beat}, the inverse coupling strength L_f and the amplitude of random birefringence fluctuation ϵ, c.f. Chapter 2 & 3. To illustrate the dependence of birefringence parameters on the nonlinear PMD we simulate the

output waveform after the input pulse train of Fig. 5.1 has propagated through a birefringent fiber with different combinations of these parameters. In Fig. 5.2, we first display the output pulses for a low PMD fiber with birefringence characterized by $\Lambda_{beat} = 25\,m$, $L_f = 12\,m$ and $\epsilon = 0.9$. The solid curve (a) is calculated with only the linear PMD term or with both the linear PMD term and the Manakov term in Eq. (5.10), while the dotted curve (b) includes also the nonlinear PMD term. Although adding the Manakov term in our example leaves the distortion nearly unaffected, the pulses are slightly reshaped due to the nonlinear PMD. We can increase the linear PMD in our model in two ways. In the first of these, while keeping $\epsilon = 0.9$, we decrease the beat length for a larger mean birefringence strength and increase the inverse coupling strength to reduce the coupling effect. For the second approach, we find that the effect of linear PMD can be increased by decreasing the value of ϵ. While Figure 5.3 displays output pulse distortion for $\Lambda_{beat} = 10\,m$, $L_f = 20\,m$ and $\epsilon = 0.9$, Fig. 5.4 shows corresponding results for $\Lambda_{beat} = 25\,m$, $L_f = 12\,m$ and $\epsilon = 0.1$. While these two approaches indeed effectively increase the linear PMD as indicated in Chapter 3, the distortion induced by the nonlinear PMD also become evident, c.f. Fig. 5.3 and Fig. 5.4. As a common feature for three combinations of Λ_{beat}, L_f and ϵ, the Manakov term does not noticeably contribute to the pulse distortion, c.f. Fig. 5.2, Fig. 5.3 and Fig. 5.4. Further calculation indicates that the Manakov term will only cause distortion when a much higher pulse power is used.

5.4 Conclusions

We have applied a general model of fiber birefringence to examine the distortion of a pulse resulting from both birefringence and nonlinearity. In contrast to the results reported in [40], we have found that the nonlinear PMD can be suppressed by a large degree of random birefringence. Further, our numerical simulation indicates that some choices of birefringence parameters not only increase the linear PMD, but also enhance the importance of the nonlinear PMD.

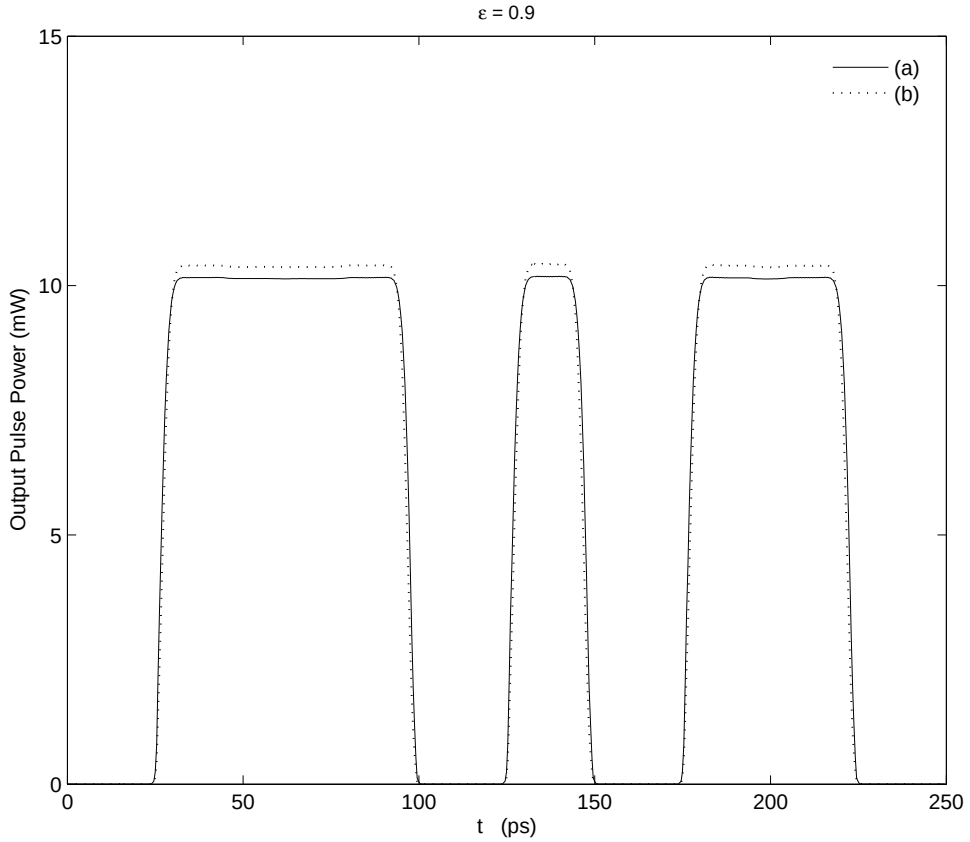

Figure 5.2: Power of the output optical pulses for fiber length $z = 2000\,km$ with a fiber birefringence characterized by $\Lambda_{beat} = 25\,m$, $L_f = 12\,m$ and $\epsilon = 0.9$. The solid curve (a) is calculated with only linear PMD term or both linear PMD term and the Manakov term in Eq. (5.10), while the dotted curve (b) includes also the nonlinear PMD term.

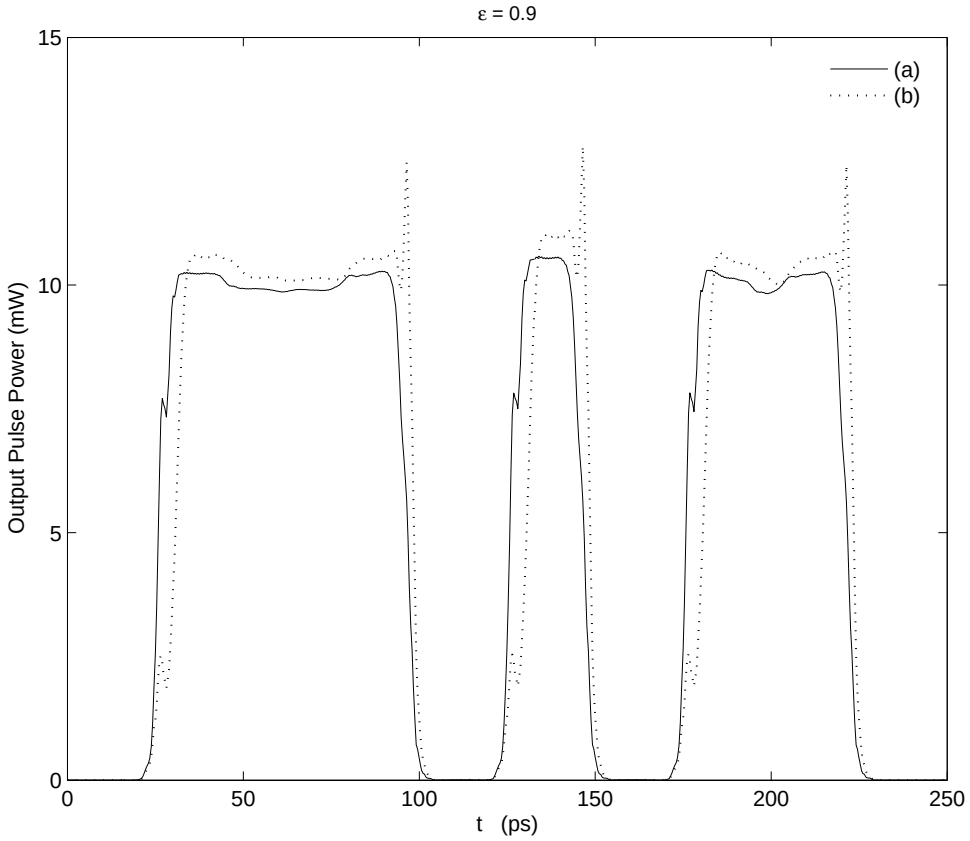

Figure 5.3: As in Fig. 5.2 but for $\Lambda_{beat} = 10\,m$ and $L_f = 20\,m$.

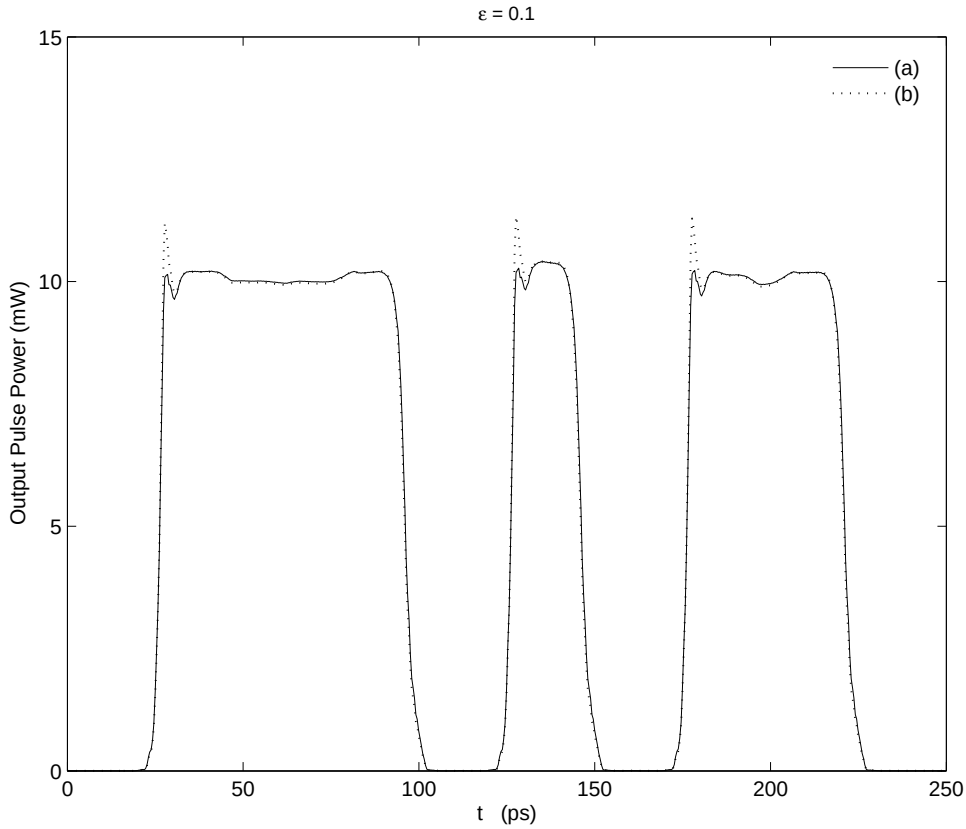

Figure 5.4: As in Fig. 5.2 but for $\epsilon = 0.1$.

Chapter 6

Conclusions

In conclusion, we have proposed four new statistical models for the description of the evolution of optical fiber birefringence with fiber length. While current models are actually the limiting cases of our formalism, our models can be adapted to a broad range of birefringent fibers. In addition, we have also introduced mathematical algorithms that simplify the numerical implementation of these models. We have then employed the birefringence models to examine PMD stochastic properties in all fiber length regions through both theoretical analysis and numerical simulations. The PMD statistics are found to vary with the birefringence model used, and these differences are compared and analyzed. Similar studies were also conducted for spun fiber, which revealed several differences compared to standard fibers. While fiber spinning has proved to be an effective technology for manufacturing low-PMD fiber and for compensating the PMD of already installed fiber systems, several general procedures have been developed for the design of broad-band PMD compensators. In last part of this thesis, we applied one of our general models to the studies of the interaction between the PMD and nonlinearity. We have found a non-negligible pulse distortion due to the nonlinear PMD that has not previously been reported. Overall, our four general fiber birefringence models extend PMD and PMD related studies in optical communications field. For example, the applications of our models on both standard single mode fiber and spun fibers have uncovered many new features of the PMD statistics. Therefore, our models may benefit the design of

low PMD fiber for both standard and spun fibers.

As well, we have demonstrated that our models of fiber birefringence are consistent with all the experimental studies of which we are aware. As expected, the flexibility of our models may lead to predictions that can be experimentally verified once improved measurement techniques for birefringence variations are developed. For example, as the resolution of the measurement of spatial distribution of birefringence strength improves, experimental results for short fibers can be compared to our numerical results. Further, while the PMD distributions obtained from different birefringence models display the same qualitative characteristics in the long fiber length region, these models differ in their predictions for the statistical behavior of the PMD at short fiber lengths. Although experimental techniques allow a determination of PMD in fibers of arbitrary length [109–112], experimental studies of the PMD statistics are currently focused in the long length region, as the PMD only significantly affects the pulse response after propagation through long fiber lengths. We believe that in future, more careful studies of local birefringence properties will become available from which the predictions of different birefringence models can be tested.

For future work, our general birefringence models and their applications could be extended in the following directions. First, while this thesis studies only first order PMD, an examination of higher-order PMD and joint PMD probability density distributions [113], which are conceivably more sensitive to the birefringence properties, would also be of interest. Second, our general birefringence models assume linear birefringence, which is applicable to most modern optical communication fibers. However, several experimental measurements of non-negligible circular birefringence in some fibers have been recently reported [52, 58, 59]. For more general applications, our birefringence models can be extended to include circular birefringence. Further, theoretical and experimental studies have demonstrated that solitons are not only stable to the perturbation of dispersion and energy variation but also robust to PMD [104, 114–119]. These could be extended by our models, although the results are of course very unlikely to change appreciably. Moreover, the mathematical algorithms employed in our birefringence models may also be modified for modeling mode coupling induced by nonlinear processes such as stim-

ulated Raman scattering (SRS) and four-wave mixing (FWM) [120]. Because of the higher sensitivity of these processes to small deviations from the phase-matching condition, our models could be of importance in this context.

Appendix A

Acronyms Used in Thesis

BER Bit Error Rate

CD Chromatic Dispersion

CW Continuous Wave

CCTV Closed Circuit Television

CNLS Coupled Nonlinear *Schrödinger* Equation

DGD Differential Group Delay

DSF Dispersion-Shifted Fiber

FWM Four-Wave Mixing

FMM Fixed Modulus Model

LAN Local Area Network

MAN Metropolitan Area Network

MRMM Modified Random Modulus Model

NRZ Non-Return-to-Zero

OFDR Optical Frequency Domain Reflectometer

PM Polarization-Maintaining

PMD Polarization Mode Dispersion

PSP Principle State of Polarization

PDCD Polarization Dependent Chromatic Dispersion

POTDR Polarization Optical Time Domain Reflectometer

PDF Probability Distribution Function

RZ Return-to-Zero

RMM Random Modulus MOdel

SI Step-Index

SOPMD Second-Order PMD

SIRF Spin-Induced Reduction Factor

SRS Stimulated Raman Scattering

TV Television

WAN Wide Area Network

WDM Wavelength-Division Multiplexing

Bibliography

[1] A. Eyal, W.K. Marshall, M. Tur, and A. Yariv. Representation of second-order polarisation mode dispersion. *Electron. Lett.*, 35(19):1658–1659, 1999.

[2] G. P. Agrawal. *Fiber-Optic Communication Systems.* John Wiley & Sons, Inc., Rochester, NY, 3rd edition, 2002, ch. 1.

[3] H. Sunnerud, M. Karlsson, and P. A. Andrekson. A comparison between NRZ and RZ data formats with respect to PMD-induced system degradation. *IEEE Photon. Technol. Lett.*, 13(5):448–450, 2001.

[4] A. Hasegawa. Theory of information transfer in optical fibers: A tutorial review. *Optical Fiber Technology*, 10:150–170, 2004.

[5] G. P. Agrawal. *Fiber-Optic Communication Systems.* John Wiley & Sons, Inc., Rochester, NY, 3rd edition, 2002, ch. 2.

[6] J. Cameron, L. Chen, and X. Bao. Impact of chromatic dispersion on the system limitation due to polarization mode dispersion. *IEEE Photon. Technol. Lett.*, 12(1):47–49, 2000.

[7] F. Bruyère. Impact of first- and second-order PMD in optical digital transmission systems. *Optical Fiber Technology*, 2:269–280, 1996.

[8] V. Chernyak, M. Chertkov, I. Gabitov, I. Kolokolov, and Vladimir Lebedev. PMD-induced fluctuations of bit-error rate in optical fiber systems. *J. Lightwave Technol.*, 22(4):1155–1168, 2004.

[9] Y-G Han and S. B. Lee. Tunable dispersion compensator based on uniform fiber bragg grating and its application to tunable pulse repetition-rate multiplication. *Opt. Express*, 13(23):9224–9229, 2005.

[10] H. Kogelnik, L. E. Nelson, and R.M. Jopson. Tutorial: Polarization-mode dispersion impairment in lightwave transmission systems. *Optical Fiber Communications*, 1:194, 2002.

[11] J. P. Gordon and H. Kogelnik. PMD fundamentals: Polarization mode dispersion in optical fibers. *Proceedings of the National Academy of Sciences*, 97(9):4541–4550, 2000.

[12] N. Gisin and J.P. Pellaux. Polarization mode dispersion: time versus frequency domains. *Opt. Commun.*, 89:316–323, 1992.

[13] M. Shtaif and M. Borditsky. The effect of the frequency dependence of PMD on the performance of optical communications systems. *IEEE Photon. Technol. Lett.*, 15(10):1369–1371, 2003.

[14] I. P. Kaminow and T. L. Koch. *Optical Fiber Telecommunications*. Academic Press, San Diego, CA, iii edition, 1997, ch. 6.

[15] Y. Namihira, Y. Horiuchi, K. Mochizuki, and H. Wakabarashi. Polarizaion mode dispersion measurements in an installed optical fiber submarine cable. *IEEE Photon. Technol. Lett.*, 1(10):329–331, 1989.

[16] D. Beltrame, F. Matera, M. Settembre, A. Galtarossa, A. Pizzinat, F. Favre, D. Le Guen, and M. Henry. Impact of polarization mode dispersion on the statistic of Q factor in optical transmission systems. *Electron. Lett.*, 36(16):1400–1402, 2000.

[17] R. Pajntar, M. Vidmar, H. Suche, A. Paoletti, and A. Schiffini. PMD penalty monitor for automatic PMD compensation of 40-Gb/s RZ data. *IEEE Photon. Technol. Lett.*, 16(4):1203–1205, 2004.

[18] E. Collett. *Polarized Light*. Marcel Dekker, Inc., Rochester, NY, iii edition, 1993, ch. 10.

[19] W. K. Marshall A. Eyal, Y. Li and A. Yariv. Statistical determination of the length dependence of high-order polarization mode dispersion. *Opt. Lett.*, 25(12):875–877, 2000.

[20] C. D. Poole and R. E. Wagner. Phenomenological approach to polarization dispersion in long single-mode fibers. *Electron. Lett.*, 22:1029–1030, 1986.

[21] D. Penninckx and V. Morenas. Jones matrix of polarization mode dispersion. *Opt. Lett.*, 24(13):875–877, 1999.

[22] F. Heismann. Accurate jones matrix expansion for all orders of polarization mode dispersion. *Opt. Lett.*, 28(21):2013–2015, 2003.

[23] H. Kogelnik, L. E. Nelson, J. P. Gordon, and R. M. Jopson. Jones matrix for second-order polarization mode dispersion. *Opt. Lett.*, 25(1):19–21, 2000.

[24] F. Curti, B. Daino, G. Marchis, and F. Matera. Statistical treatment of the evolution of the principal states of polarization in single-mode fibers. *J. Lightwave Technol.*, 8(8):1162–1166, 1990.

[25] C. D. Poole, N. S. Bergano, R. E. Wagner, and H. J. Schulte. Polarization dispersion and principle states in a 147-km undersea lightwave cable. *J. Lightwave Technol.*, 6(7):1185–1190, 1988.

[26] D. Kuperman, A. Eyal, O. Mor, S. Traister, and M. Tur. Measurement of the input states of poloarization that maximize and minimize the eye opening in the presence of PMD and PDL. *IEEE Photon. Technol. Lett.*, 15(10):1425–1427, 203.

[27] W. Shieh. Principal states of polarization for an optical pulse. *IEEE Photon. Technol. Lett.*, 11(6):677–679, 1999.

[28] H. Kogelnik, L. E. Nelson, and J. P. Gordon. Emulation and inversion of polarization-mode dispersion. *J. Lightwave Technol.*, 21(2):482–495, 2003.

[29] Y. Suetsugu, T. Kato, and M. Nishimura. Full characterization of polarization-mode dispersion with random-mode coupling in single-mode optical fibers. *IEEE Photon. Technol. Lett.*, 7(8):887–889, 1995.

[30] G. J. Foschini and C. D. Poole. Statistical theory of polarization dispersion in single mode fibers. *J. Lightwave Technol.*, 9(11):1439–1456, 1991.

[31] R. M. Jopson, L. E. Nelson, and H. Kogelnik. Measurement of second-order polarization-mode dispersion vectors in optical fibers. *IEEE Photon. Technol. Lett.*, 11(9):1153–1155, 1999.

[32] Y. Li, A. Eyal, P.-O. Hedekvist, and A. Yariv. Measurement of high-order polarization mode dispersion. *IEEE Photon. Technol. Lett.*, 12(7):861–863, 2000.

[33] T. Gravemann, J. Kissing, and E. Voges. Signal degradation by second-order polarization-mode dispersion and noise. *IEEE Photon. Technol. Lett.*, 16(3):795–797, 2004.

[34] H. B*ü*low. System outage probability due to first- and second-order PMD. *IEEE Photon. Technol. Lett.*, 10(5):696–698, 1998.

[35] A. Djupsj*ö*acka. On differential group-delay statistics for polarization-mode dispersion emulators. *J. Lightwave Technol.*, 19(2):285–290, 2001.

[36] M. Karlsson. Probability density functions of the differential group delay in optical fiber communication systems. *J. Lightwave Technol.*, 19(3):324–331, 2001.

[37] M. Karlsson, J. Brentel, and P. A. Andrekson. Long-term measurement of PMD and polarization drift in installed fibers. *J. Lightwave Technol.*, 18(7):941, 2000.

[38] N. Gisin, R. Passy, P. Blasco, and M. Devente etc. Definition of polarization mode dispersion and first results of the COST 241 round-robin measurements. *Pure Appl. Opt.*, 4:511–522, 1995.

[39] C. D. Poole, J. H. Winters, and J. A. Nagel. Dynamical equation for polarization dispersion. *Opt. Lett.*, 16(6):372–374, 1991.

[40] D. Marcuse, C. R. Menyuk, and P. K. A. Wai. Application of the Manakov-PMD equation to studies of signal propagation in optical fibers with randomly varying birefringence. *J. Lightwave Technol.*, 15(9):1735–1745, 1997.

[41] P.K. Wai and C. R. Menyuk. Polarization mode dispersion, decorrelation, and diffusion in optical fibers with randomly varying birefringence. *J. Lightwave Technol.*, 14(2):148, 1996.

[42] C. D. Poole. Statistical treatment of polarization dispersion in single-mode fiber. *Opt. Lett.*, 13(8):687–689, 1988.

[43] Ivan P. Kaminow. Polarization in optical fibers. *J. Quantum Electron.*, 17(1):15–22, 1981.

[44] C. R. Menyuk. Nonlinear pulse propagation in birefringent optical fibers. *J. Quantum Electron.*, QE-23(2):174–176, 1987.

[45] A. Simon and R. Ulrich. Evolution of polarization of a single-mode fiber. *Appl. Phys. Lett.*, 31(8):517–520, 1977.

[46] V. Ramaswamy, W. G. French, and R. D. Standley. Polarization characteristics of noncircular core single-mode fibers. *Appl. Opt.*, 17(18):3014–3017, 1978.

[47] Y. Fujii and K. Sano. Polarization coupling in twisted elliptical optical fiber. *Appl. Opt.*, 19(15):2602, 1980.

[48] V. Ramaswamy, R. D. Standley, D. Szeand, and W. G. French. Polarization effects in short length, single mode fibers. *B.S.T.J.*, 57(3):635–651, 1978.

[49] V. Ramaswamy and W. G. French. Influence of noncircular core on the polarization performance of single mode fibers. *Electron. Lett.*, 14(5):143–144, 1978.

[50] M. Wegmuller, M. Legré, P. Oberson, L. Guinnard, C. Vinegoni, and N. Gisin. Analysis of the polarization evolution in a ribbon cable using high-resolution coherent OFDR. *IEEE Photon. Technol. Lett.*, 13(2):145–147, 2001.

[51] B. Huttner, J. Reecht, N. Gisin, R. Passy, and J. P. von der Weid. Local birefringence measurements in single-mode fibers with coherent optical frequency-domain reflectometry. *IEEE Photon. Technol. Lett.*, 10(10):1458–1460, 1998.

[52] M. Wegmuller, M. Legré, and N. Gisin. Distributed beatlength measurement in single-mode fibers with optical frequency-domain reflectometry. *J. Lightwave Technol.*, 20(5):828–835, 2002.

[53] A. Galtarossa, L. Palmieri, A. Pizzinat, M. Schiano, and T. Tambosso. Measurement of local beat length and differential group delay in installed single-mode fibers. *J. Lightwave Technol.*, 18(10):1389–1394, 2000.

[54] A. Galtarossa, L. Palmieri, M. Schiano, and T. Tambosso. Statistical characterization of fiber random birefringence. *Opt. Lett.*, 25(18):1322–1324, 2000.

[55] A. Galtarossa, L. Palmieri, M. Schiano, and T. Tambosso. Measurements of beat length and perturbation length in long single-mode fibers. *Opt. Lett.*, 25(6):384–386, 2000.

[56] A. Galtarossa, L. Palmieri, M. Schiano, and T. Tambosso. Measurement of birefringence correlation length in long, single-mode fibers. *Opt. Lett.*, 26(13):962–964, 2001.

[57] M. Wulipart, P. Mégret, M. Blondel, A. Rogers, and Y. Defosse. Measurement of the spatial distribution of birefringence in optical fibers. *IEEE Photon. Technol. Lett.*, 13:836–838, 2001.

[58] A. Galtarossa and L. Palmieri. Measure of twist-induced circular birefringence in long single-mode fibers: theory and experiments. *J. Lightwave Technol.*, 20(7):1149–1159, 2002.

[59] A. Galtarossa and L. Palmieri. Spatially resolved PMD measurements. *J. Lightwave Technol.*, 22(4):1103–1115, 2004.

[60] L. Arnold. *Stochastic Differential Equations, Theory and Applications*. Wiley, New York, NY, 1974.

[61] J. Yang and W. L. Kath andC.R. Menyuk. Polarization mode dispersion probability distribution for arbitrary distances. *Opt. Lett.*, 26(19):1472–1474, 2001.

[62] A. Galtarossa, P. Griggio, L. Palmieri, and A. Pizzinat. Polarization mode dispersion properties of constantly spun randomly birefringent fibers. *Opt. Lett.*, 28(18):1639–1641, 2003.

[63] A. Pizzinat, B. S. Marks, L. Palmieri, C. R. Menyuk, and A. Galtarossa. Influence of the model for random birefringence on the differential group delay of periodically spun fibers. *IEEE Photon. Technol. Lett.*, 15(6):819–821, 2003.

[64] A. Galtarossa, L. Palmieri, A. Pizzinat, B. S. Marks, and C. R. Menyuk. An analytical formula for the mean differential group delay of randomly birefringent spun fibers. 20(7):1635–1643, 2003.

[65] A. Galtarossa, L. Palmieri, and Anna Pizzinat. Optimized spinning design for low PMD fibers: An analytical approach. *J. Lightwave Technol.*, 19(10):1502–1512, 2001.

[66] D. A. Nolan, X. Chen, and M. J. Li. Fibers with low polarization-mode dispersion. *J. Lightwave Technol.*, 22(4):1066–1077, 2004.

[67] P. Poggiolini, A. Nespola, S. Abrate, V. Ferrero, and C. Lezzi. Long-term PMD characterization of a metropolitan g.652 fiber plant. *JLT*, 24(11):4022, 2006.

[68] D. Sarchi and G. Roba. PMD mitigation through constant spinning and twist control: experimental results. *OFC'2003 Tech. Dig., 2003*, pages 367–368.

[69] Y. Wang, C. Xu, and V. Izraelian. Characterization of spun fibers with millimeter spin periods. *Optical Express*, 13(10):3841, 2005.

[70] A. Galtarossa, P. Griggio, A. Pizzinat, and L. Palmieri. Calculation of the mean differential group delay of periodically spun, randomly birefringent fibers. *Opt. Lett.*, 27(9):692–694, 2002.

[71] R. E. Schuh, X. Shan, and A. Siddiqui. Polarization mode dispersion in spun fibers with different linear birefringence and spinning parameters. *J. Lightwave Technol.*, 16(9):1583–1588, 1998.

[72] M. Li X. Chen and D. A. Nolan. Polarization mode dispersion of spun fibers: an analytical solution. *Opt. Lett.*, 27(5):294–296, 2002.

[73] M. J. Li and D. A. Nolan. Fiber spin-profile designs for producing fibers with low polarization mode dispersion. *Opt. Lett.*, 23(21):1659–1661, 1998.

[74] M. Li X. Chen and D. A. Nolan. Scaling properties of polarization mode dispersion of spun fibers in the presence of random mode coupling. *Opt. Lett.*, 27(18):1595–1597, 2002.

[75] A. Galtarossa, P. Griggio, L. Palmieri, and A. Pizzinat. First- and second-order PMD statistical properties of constantly spun randomly birefringent fibers. *J. Lightwave Technol.*, 22(4):1127–1136, 2004.

[76] A. Pizzinat, L. Palmieri, B. S. Marks, C. R. Menyuk, and A. Galtarossa. Analytical treatment of randomly birefringent periodically spun fibers. *J. Lightwave Technol.*, 21(12):3355, 2003.

[77] A. Pizzinat, B. S. Marks, C. R. Menyuk, and A. Galtarossa. Polarization mode dispersion of spun fibers with randomly varying birefringence. *Opt. Lett.*, 28(6):390–392, 2003.

[78] M. Shtaif, A. Mecozzi, M. Tur, and J. A. Nagel. A compensator for the effects of high-order polarization mode dispersion in optical fibers. *IEEE Photon. Technol. Lett.*, 12(4):434–436, 2000.

[79] I. T. Lima, R. Khosravani, P. Ebrahimi, E. Ibragimov, C. R. Menyuk, and A. E. Willner. Comparison of polarization mode dispersion emulators. *J. Lightwave Technol.*, 19(12):1872–1881, 2001.

[80] L. Yan, M. C. Hauer, Y. Shi, X. S. Yao, P. Ebrahimi, Y. Wang, A. E. Willner, , and W. L. Kath. Polarization-mode-dispersion emulator using variable

differential-group-delay (DGD) elements and its use for experimental importance sampling. *J. Lightwave Technol.*, 22(4):1051–1058, 2004.

[81] H. Sunnerud, M. Karlsson, C. Xie, and P. A. Andrekson. Polarization-mode dispersion in high-speed fiber-optic transmission systems. *J. Lightwave Technol.*, 20(12):2204–2219, 2002.

[82] I. T. Lima, A. O. Lima, G. Biondini, C. R. Menyuk, and W. L. Kath. A comparative study of single-section polarization-mode dispersion compensators. *J. Lightwave Technol.*, 22(4):1023–1032, 2004.

[83] A. Yariv. *Optical Fiber Communication*. Oxford U. Press, 5th edition, 1997.

[84] T. Kudou, M. Iguchi, M. Masuda, and T. Ozeki. Theoretical basis of polarization mode dispersion equalization up to the second order. *J. Lightwave Technol.*, 18(4):614–617, 2000.

[85] E. Hellstrom, H. Sunnerud, M. Westlund, and M. Karlsson. Third-order dispersion compensation using a phase modulator. *J. Lightwave Technol.*, 21:1188–1197, 2003.

[86] L. Moller. Filter synthesis for broad-band PMD compensation in WDM systems. *IEEE Photon. Technol. Lett.*, 12(9):1258–1260, 2000.

[87] A. Eyal and A. Yariv. Design of broad-band PMD compensation filters. *IEEE Photon. Technol. Lett.*, 14(8):1088–1090, 2002.

[88] W. H. Press, B. P. Flannery, and S. A. Teukolsky. *Numerical Recipes in* C. Cambridge U. Press, Rochester, NY, 2nd edition, 1992.

[89] S. Lanne and E. Corbel. Practical considerations for optical polarization-mode dispersion compensators. *J. Lightwave Technol.*, 22(4):1033–1040, 2004.

[90] M. Glasner, D. Yevick, and B. Hermannson. Generalized propagation formulas of arbitrarily high order. *J. Chem. Phys.*, 95(11):8266–1667, 1991.

[91] A. D. Bandrauk and H. Shen. Improved exponential split operator method for solving the time-dependent *schrödinger* equation. *Proc. Japan Acad.*, 176(5):428–432, 1991.

[92] T. J. Rivlin. *The Chebyshev Polynomials*. Wiley, New York, NY, 1974.

[93] D. Yevick, M. Chanachowicz, M. Reimer, M. O'Sullivan, W. Huang, and T. Lu. Chebyshev and taylor approximations of polarization mode dispersion for improved compensation bandwidth. *J. Opt. Soc. Amer. A*, 22(8):1662–1667, 2005.

[94] G. P. Agrawal. *Nonlinear Fiber Optics*. Academic Press, Rochester, NY, 3rd edition, 2001, ch. 1.

[95] G. Luther and M. S. Alber. Nonlinear wave, nonlinear optics and your communications future. *Nonlinear Science Today*, pages 1–19, 1997.

[96] R. H. Stolen, J. Botineau, and A. Ashkin. Intensity discrimination of optical pulses with birefringent fibers. *Opt. Lett.*, 7(10):512–515, 1982.

[97] D. Alzetta and M. Matsumoto. Transmission degradation due to polarization-mode dispersion in linear and nonlinear systems. *Optical Fiber Communications*, pages 50–51, 2002.

[98] C.R. Menyuk. Interaction of nonlinearity and polarization mode dispersion. *J. Opt. Fiber. Commun. Rep.*, 1:305–311, 2004.

[99] P.K.A. Wai, C.R. Menyuk, and J. W. Zhang. Nonlinear polarization-mode dispersion in optical fibers with randomly varying birefringence. *J. Opt. Soc. Amer. B*, 14(11):2967–2979, 1997.

[100] D. Marcuse, C.R. Menyuk, and R. Holzlohner. Time shift of pulses due to dispersion slope and nonlinearity. *IEEE Photon. Technol. Lett.*, 11(12):1611–1613, 1999.

[101] C.R. Menyuk. Stability of solitons in birefringent optical fibers. II. arbitrary amplitudes. *J. Opt. Soc. Amer. B*, 5(2):392–402, 1988.

[102] C.R. Menyuk. Pulse progation in an elliptically birefringent kerr medium. *J. Quantum Electron.*, 25(12):2674–2682, 1989.

[103] C.R. Menyuk. Stability of solitons in birefringent optical fibers. I: Equal propagation amplitudes. *Opt. Lett.*, 12(8):614–616, 1987.

[104] M. Matsumoto, Y. Akagi, and A. Hasegawa. Propagation of solitons in fibers with randomly varying birefringence: Effects of soliton transmission control. *J. Lightwave Technol.*, 15(4):584–589, 1997.

[105] F. Matera and M. Settembre. Compensation of polarization mode dispersion by means of the kerr effect for nonreturn-to-zero signals. *Opt. Lett.*, 20(1):28–30, 1995.

[106] D. Marcuse and C. R. Menyuk. Simulation of single-channel optical sysmtems at 100 Gb/s. *J. Lightwave Technol.*, 17(4):564–569, 1999.

[107] P.K.A. Wai, C.R. Menyuk, and H.H. Chen. Stability of solitons in randomly varying birefringent fibers. *Opt. Lett.*, 16(16):1231–1233, 1991.

[108] C. Xie, M. Karlsson, P.A. Andrekson, and H. Sunnerud. Robustness of dispersion-managed solitons to the polarization-mode dispersion in optical fibers. *IEEE Photon. Technol. Lett.*, 13(2):121–123, 2001.

[109] C. T. Allen, P. K. Kondamuri, D. L. Richards, and D. C. Hague. Measured temporal and spectral PMD characteristics and their implications for network-level mitigation approaches. *J. Lightwave Technol.*, 21(1):79–86, 2003.

[110] C. D. Poole. Measurement of polarization-mode dispersion in single-mode fibers with random mode coupling. *Opt. Lett.*, 14(10):523–525, 1989.

[111] E. Simova, I. Powell, and C. P. Grover. Measurement of femtosecond polarization mode dispersion (PMD) using biased p-shifted lowcoherence interferometry. *Opt. Express*, 7(6):228–236, 2000.

[112] B. L. Heffner. Attosecond-resolution measurement of polarization mode dispersion in short sections of optical fiber. *Opt. Lett.*, 18(24):2102–2104, 1993.

[113] D. Yevick. Multicanonical evaluation of joint probability density functions in communication system modeling. *IEEE Photon. Technol. Lett.*, 15(11):1540–1542, 2003.

[114] L.F. Mollenauer, K. Smith, and J.P. Gordon. Resistance of solitons to the effects of polarization dispersion in optical fibers. *Opt. Lett.*, 14(21):1219–1221, 1989.

[115] T. L. Lakoba and D. J. Kaup. Perturbation theroy for the manakov soliton and its applications to pulse propagation in randomly birefringent fibers. *Phys. Rev. E*, 56(5):6147–6165, 1997.

[116] Y. Chen and H.A. Haus. Solitons and polarization mode dispersion. *Opt. Lett.*, 25(5):290–292, 2000.

[117] C. Xie, M. Karlsson, and P.A. Andrekson. Soliton robustness to the polarization-mode dispersion in optical fibers. *IEEE Photon. Technol. Lett.*, 12(7):801–803, 2000.

[118] B. Bakhshi, J. Hansryd, P.A. Andrekson, J. Brentel, E. Kolltveit, B.-E. Olsson, and M. Karlsson. Experimental observation of soliton robustness to polarization dispersion pulse broadening. *Electron. Lett.*, 35(7):65–66, 1999.

[119] H. Sunnerud, J. Li, P.A. Andrekson, and C. Xie. Experimental quantification of soliton robustness to polarization-mode dispersion in dispersion-managed systems. *IEEE Photon. Technol. Lett.*, 13:118–120, 2001.

[120] G. P. Agrawal. *Nonlinear Fiber Optics*. Academic Press, Rochester, NY, 3rd edition, 2001, ch. 8 & ch. 10.